Journal of Applied Mathematics and Physics, 2025, 13(3), 729-796
https://www.scirp.org/journal/jamp
ISSN Online: 2327-4379
ISSN Print: 2327-4352

Generalized Robust Systems-Based Theoretical Kinematic Inverse/Regular Wedge Cam Theory for Three-Point Diametral Self-Centering Motion

Shawn P. Guillory, Alan A. Barhorst, Jim Lee, Raju Gottumukkala, Jonathan R. Raush, Terrence L. Chambers

Department of Mechanical Engineering, The University of Louisiana at Lafayette, Lafayette, USA
Email: shawn.guillory1@louisiana.edu, alan.barhorst@louisiana.edu, jim.lee@louisiana.edu, jonathan.raush@louisiana.edu, raju.gottumukkala@louisiana.edu, terrence.chambers@louisiana.edu

How to cite this paper: Guillory, S.P., Barhorst, A.A., Lee, J., Gottumukkala, R., Raush, J.R. and Chambers, T.L. (2025) Generalized Robust Systems-Based Theoretical Kinematic Inverse/Regular Wedge Cam Theory for Three-Point Diametral Self-Centering Motion. *Journal of Applied Mathematics and Physics*, **13**, 729-796.
https://doi.org/10.4236/jamp.2025.133040

Received: February 4, 2025
Accepted: March 16, 2025
Published: March 19, 2025

Abstract

Generalized robust systems-based theoretical kinematic inverse/regular wedge cam procedures which produce self-centering motion applicable to three-point clamping device design about cylindrical workpieces that vary within a prescribed size range are presented. Within such presentment, various parametric (trigonometric, combined loop closure with vector projection/resolution, transformation) and rectangular form (Taylor series approximation, trigonometric substitution & transformation (TS&T), nonlinear ODE) equation methods along with related statics and dynamics are explored. In connection, a simulated unified resultant amplitude method (URAM) is applied for generalization purposes. Moreover, the theoretical framework is validated within the context of a computer-generated model of a mechanism design which demonstrates self-centering over the prescribed design range with negligible to zero error. Furthermore, the static and dynamic analyses are verified through computer-aided engineering simulation in conjunction with equilibrium equations and a consideration of various calculus principles. Consequently, the self-centering theoretical formulation coupled with static and dynamic analyses provide for an accurate and generalized quantitative model couched within a holistic systems engineering framework which can be useful for providing state-of-the-art engineering and design optimization of various parameters for developing new and/or improved self-centering gripping devices of the inverse/regular wedge cam type.

Keywords

Self-Centering Wedge Cam, Robotic End Effector, Gripper Device, Design

Optimization, Unified Resultant Amplitude Method, Nonlinear ODE

1. Introduction

In the development of self-centering devices which clamp around cylindrical workpieces, there are several different existing kinematic design configurations which produce the type of desired functionality in relation to the intended application set forth by the designer. The various practical configurations of such devices usually include anywhere from two to four points of contact. As a related example, self-centering steady rest products/utility patents used for gripping cylindrical workpieces involved in CNC lathe machining processes revolve around three-point contact clamping devices [1]-[19]. Another similar clamping device design includes a patented oil & gas wrench involving similar, but different, three-point contact self-centering motion serving as a method for gripping and positioning thin-walled cylinders [20]. Other comparable clamping device designs include a two-point pipe clamping chuck design in addition to a two-arm holding self-centering pipeline clamping device among others [21] [22].

In connection, and regarding diverse applicability of related gripping mechanisms, Afandiyev and Nuriyev discuss the occurrence of clamping devices being widely used in various industries with constantly increasing needs, especially in relation to processing accuracy and the forces acting on the clamped part. The reliability of such devices in terms of their use on thin-walled cylinders, in particular drill pipes, is highlighted due to plastic deformations being highly prevalent in clamping zones as a result of current clamping devices creating uneven loading arrangements with associated contact pressure distributions/compressive stresses exceeding the pipe material yield strength. In an effort to remedy these issues involving the state of the pipe and holding capacity of the clamping device, a concept of a pipe clamping chuck design with basic design detail is provided [21].

Additionally, Haixia, Liquan, Shiqing, and Xianchao discuss multifunctional pipeline repair machinery being used in the deep-sea arena along with the difficulty of gripping pipelines while ensuring their concentricity between cutter heads and the pipeline during operation. In view of this, a new design involving a two-arm holding self-centering pipeline clamping device is proposed which involves two groups of parallelogram double-rocker and cranking block mechanisms. The recommended design is extensive in presentment with schematic representations along with 3D modeling as well as detailed calculations coupled to CAE simulation and being accompanied by the real clamping device prototype with satisfactory testing results [22].

Furthermore, Mhamane, Bavadekar, Dhokale, Hogade, Patil, and Survase among others discuss the use of a self-centering steady rest for eliminating problems involving vibration and deflection on workpieces while machining. They also describe its facilitation regarding an increase in productivity by reducing cycle time along with being able to obtain higher accuracy and good surface finish. Consequently, a regular wedge cam design within the context of a self-centering steady rest is discussed for improving these characteristics with design aspects being presented based on a graphical incremental angle approach within the computer-aided design environment [23]-[25]. Moreover, and expanding on self-centering steady rests and their inherent cam design due to the proposed research being centered around similar three-point clamping device design, existing related theory explores analytical approaches to the development of the regular wedge cam path involving parametric equation formulation through trigonometric and velocity techniques as well as approximating the cam contour using regression analysis and first-order iterative solver approximation procedures [26]-[35].

In further review of various cam designs within related Mechanism and Machine Theory for exploring other potential analytical techniques which may be useful for advancing gripping mechanisms of this type, existing literature is rather extensive but largely devoted to plate cam design along with a discussion of the uncommon occurrence of wedge cam design in addition to covering a wide variety of other specialized cam mechanisms [36]-[38]. Several of the various related kinematic cam formulations involve parameterization regarding the theory of envelopes in addition to using cylindrical cam surface indexing for plate cam designs having mathematical content revolving around disk, cylindrical, camoid, globoidal, and conical cam profiles [39] [40]. Other well-known plate cam profile creation techniques include the Polydyne approach and polynomial curve fitting for efficient, desired, and minimized vibrational cam profiles [41]. Additionally, spline curve methods are used for plate cams lacking in harmonic content with having concerns regarding accuracy and computational expensiveness when higher order curves are necessary for producing higher order derivative accuracy in relation to cam profile dynamics [42] [43]. Moreover, the Fourier series may be used as a local mathematical approximation for modeling plate cam follower displacements along with minimizing residual cam vibrations among other cam dynamic characteristics [43].

Including examples of related self-centering mechanism and machine theory, general theoretical bar mechanisms, namely self-aligning systems, are constructed by manipulating the mechanism's mobility via joint replacements [44]. In comparison to self-aligning systems, the seven-bar mechanism supplies self-centering motion at the output for disc-brake systems which constructs a coupled solution for producing clamping action in conjunction with equalized force distribution [45].

As previously discussed, there is an increasing need for reliability involving clamping accuracy, force transmission, vibration minimization, material deformation, productivity, and more. Improving these characteristics is not a trivial exercise due to manufacturing, quality, and engineering considerations whereby the design and analysis variables are rather numerous and complex therefore making it difficult for combining and directing toward optimizing characteristics through typical manual type adjustments in a computer-aided design environment or by analytical presentments that are lacking in robustness. Consequently, this can be better achieved through having a rigorous systems-based theoretical engineering model for incorporating robust design/robust design optimization techniques toward achieving world-class engineering and design intent.

Nevertheless, and despite such expansiveness on cam and associated product design with related mechanism and machine theory, existing literature does not provide a holistic analytical approach to developing three-point clamping devices of its specific or similar kind and by which is required as part of providing a more rigorous, useful and properly structured quantitative model for incorporating advanced design and robust design optimization techniques as part of contemporary engineering efforts for meeting the high-quality demands of today. Additionally, existing related theory is not wholly generalized and only explores parametric equation development of the regular wedge cam type specific to self-centering steady rests with the workpiece radius as the independent variable and by which is unbounded and may lead to mathematical errors within the theory and accompanying designs [26]-[32].

However, the research entailed herein presents a more generalized and robust theoretical quantitative model/framework with taking a holistic systems engineering approach to designing accurate three-point self-centering mechanisms about a variable workpiece diameter of both the inverse and regular wedge cam types. This, more generalized and unified theoretical construction, is useful for extending the usage of such toward the design and development of three-point self-centering clamping devices of this type and by which may include designing devices similar to existing practical application within the manufacturing industry regarding self-centering steady rests in addition to the oil & gas industry involving pipe handling and/or pipeline repair machinery as well as finding its way into other industries such as aerospace, construction equipment, precision medical, and many other potential industry applications whereby the efficiency and utility of such vigorously engineered and optimized product designs resulting from this applied mathematical modeling regarding mechanism and machine theory may be beneficial. Furthermore, and important to note, various aspects and approaches provided within the theory, such as the application of the unified resultant amplitude method (URAM) among others, may also inspire research efforts and application of such to other areas of engineering, physics, and mathematics.

The presented formulation also includes important design considerations such as clearances and contact angles for broadening practical design aspects as well as for being required as part of applying advanced robust design optimization techniques to critical characteristics related to force balancing and vibration minimization among others. Additionally, coordinate points are used for specifying critical design locations and related lengths which are also more useful for design optimization in terms of developing the limits of the design optimization space as well as for use in generalization of the theoretical framework. Furthermore, the independent variable is the angle of cam rotation rather than the workpiece radius which is required for generalizing the backward kinematic cam rotation equation due to the bounded nature of the rotation angle.

Moreover, and considering generalization and robustness, all related kinematics of the self-centering arrangement that factor into the development of the parametric equations are explored through various approaches including trigonometric, a generalized combined double loop-closure with vector projection/resolution method, and finally through a consideration of transformation equations required for rectangular form conversion. Parametric equations are then extended into direct rectangular form conversion using both approximation (Taylor series and nonlinear ODE) and exact (trigonometric substitution & transformation (TS&T) and nonlinear ODE) methods which may be useful for robotics & controls theory application among other theoretically applied uses in design and optimization. In conjunction, a simulated unified resultant amplitude method is uniquely applied toward dynamics and the generalization of the theoretical framework. Additional aspects incorporated for providing a holistic systems engineering methodology including robust design optimization application requirements involve normalization of the cam path, providing generalized statics with taking a systems approach required for determining various contact and reaction forces along with related machine design and application engineering considerations, as well as including related dynamics with direct application of the cam rotation equation development utilizing the simulated unified resultant amplitude method.

2. Nomenclature

2.1. Specified/Driving Analysis Variables

θ: Independent Cam Rotation Variable;

R_{wmin}: Minimum Actual Workpiece Radius;

R_{wmax}: Maximum Actual Workpiece Radius;

r: Gripper Roller Radius;

C_{lrx}: Horizontal Clearance;

φ_o: Initial Contact Angle;

x_1: Horizontal Coordinate from Origin O_1 to Pivot Point O_2;

y_1: Vertical Coordinate from Origin O_1 to Pivot Point O_2;

x_2: Horizontal Coordinate from Origin O_1 to Roller Follower Starting Point D;

y_2: Vertical Coordinate from Origin O_1 to Roller Follower Starting Point D;

x_{m1}: Horizontal Coordinate from Origin O_1 to Normal (Friction Related) Force on the Upper End of the Translational Gripper;

y_{m1}: Vertical Coordinate from Origin O_1 to Normal (Friction Related) Force on the Upper End of the Translational Gripper;

x_{m2}: Horizontal Coordinate from Origin O_1 to Normal (Friction Related) Force on the Lower End of the Translational Gripper/Actuator;

y_{m2} : Vertical Coordinate from Origin O_1 to Normal (Friction Related) Force on the Lower End of the Translational Gripper/Actuator;

μ_s : Static Friction Coefficient;

F_a : Activation Force;

F_{wpx} : Total External Horizontal Reaction Force on the Workpiece;

F_{wpy} : Total External Vertical Reaction Force on the Workpiece;

M_{extx} : Total External Moment About x -axis;

M_{exty} : Total External Moment About y -axis;

M_{extz} : Total External Moment About z -axis;

P_c : Constant Power Source

2.2. Calculated/Driven Fixed Analysis Variables

R_{twmax} : Maximum Theoretical Workpiece Radius;

L_1 : Rotational Gripper Length from Pivot Point O_2 (or O_3) to Point B (or C);

L_2 : Length from Pivot Point O_2 (or O_3) to Cam Roller Follower Starting Point D (or E);

L_3 : Theoretical Length from Origin O_1 to Pivot Point O_2 (or O_3);

η : Starting Angle from Negative (or Positive) x -axis to Length L_1 [Relative to a Coordinate System at Pivot Point O_2 (or O_3)];

δ : Counterclockwise (or Clockwise) Angle from Length L_1 to Length L_2 [Relative to a Coordinate System at Pivot Point O_2 (or O_3)];

β : Angle from Negative (or Positive) x -axis to Length L_3 [Relative to a Coordinate System at Pivot Point O_2 (or O_3)];

2.3. Calculated/Driven Variable Equations/Analysis Functions

μ : Angle of Rotation from the Negative (or Positive) x -axis to the Line from Pivot Point O_2 (or O_3) to Point D_2 (or E_2) [Relative to a Coordinate System at Pivot Point O_2 (or O_3)];

ϵ : Supplementary Angle of Rotation Corresponding to the Angle of Rotation μ [Relative to a Coordinate System at Pivot Point O_2 (or O_3)];

R_{tw} : Theoretical Workpiece Radius (Congruent to the Actual Workpiece when $R_{wmin} \le R_{tw} \le R_{wmax}$ is Satisfied);

x_3 : Horizontal Coordinate from Origin O_1 to Rotational Gripper Roller Center Point B (or C);

y_3 : Vertical Coordinate from Origin O_1 to Rotational Gripper Roller Center Point B (or C);

x_4 : Horizontal Coordinate from Origin O_1 to Translational Gripper Roller Center Point A;

y_4 : Vertical Coordinate from Origin O_1 to Translational Gripper Roller Center Point A;

x_5 : Horizontal Coordinate from Origin O_1 to Roller Follower Starting Point D;

y_5: Vertical Coordinate from Origin O_1 to Roller Follower Point D_1 (or E_1);

x_6: Horizontal Coordinate from Origin O_1 to Point D_2 (or E_2);

y_6: Vertical Coordinate from Origin O_1 to Point D_2 (or E_2);

h_c: Length from Point D_2 (or E_2) to Roller Follower Point D_1 (or E_1);

ω: Angle of Rotation from Positive (or Negative) x-axis to Length h_c [Relative to a Coordinate System at Cam Roller Follower Point D_1 (or E_1)];

λ: Angle of Rotation from Positive (or Negative) x'-axis to Length h_c [Relative to a Coordinate System at Cam Roller Follower Point D_1 (or E_1)];

x_c: Horizontal Component of the Wedge Cam Path;

y_c: Vertical Component of the Wedge Cam Path;

ζ: Angle of Rotation from the Negative (or Positive) y-axis to Length from Pivot Point O_2 (or O_3) to Point D_2 (or E_2) (Relative to a Coordinate System at Pivot Point O_2 (or O_3)];

γ: Angle of Rotation from the Negative (or Positive) x-axis to Length from Pivot Point O_2 (or O_3) to Point D_2 (or E_2) (Relative to a Coordinate System at Pivot Point O_2 (or O_3)];

φ: Contact Angle;

$R_{head\ tail}$: Link Lengths for Loop-Closure Equations;

θ_{head}: Angles of Rotation for Loop-Closure Equations;

c: Polynomial Coefficients, Dependent Summation Wave Variable, Instantaneous Constant ODE Parameter;

Θ: Trigonometric Numerator Parameter;

Γ: Trigonometric Denominator Parameter;

a: Cosine Wave Amplitude;

b: Sine Wave Amplitude;

m: N-Ary Product Index, Multiple of π;

q: Quadrant Location of Wave Summation;

$\hat{R}$: Resultant Amplitude Combination-Wave Fluctuation;

$\hat{\varnothing}$: Phase Angle Combination-Wave Fluctuation;

R: Resultant Amplitude;

$\varnothing$: Phase Angle;

θ_{max}: Maximum Cam Rotation;

s_{num}: ODE Solution Number;

$\hat{s}_1$: First ODE Plus/Minus Sign Pattern;

$\hat{s}_2$: Second ODE Plus/Minus Sign Pattern;

k: Variable ODE Initial Condition;

ς: Normalization Parameter;

α: Rotational Gripper Angle O_1O_2B (or O_1O_3C);

ψ: Angle Corresponding to Triangle O_1BO_2 (or O_1CO_3);

m_c: Wedge Cam Contour Slope;

ρ: Tangential Force Angle;

Ω: Normal Force Angle;

ϕ: Pressure Angle;

d_m : Horizontal Moment Arm Length of Normal Cam Path Force Transmissibility;
F_A : Translational Gripper Contact Force;
F_B : Right-Side Rotational Gripper Contact Force;
F_C : Left-Side Rotational Gripper Contact Force;
$F_{D1,2}$: Right Side Normal Force at Roller Follower Point D_1 (or D_2);
$F_{E1,2}$: Left Side Normal Force at Roller Follower Point E_1 (or E_2);
F_{N1} : Normal (Friction Related) Force on the Upper End of Translational Gripper;
F_{N2} : Normal (Friction Related) Force on the Lower End of Translational Gripper;
F_{O2x} : Horizontal Component of the Reaction Force at Pivot Point O_2;
F_{O2y} : Vertical Component of the Reaction Force at Pivot Point O_2;
F_{O3x} : Horizontal Component of the Reaction Force at Pivot Point O_3;
F_{O3y} : Vertical Component of the Reaction Force at Pivot Point O_3;
t : Time Parameter;
s_{TG} : Linear Displacement Function;
v_{TG} : Rectilinear Translational Gripper Velocity;
ω_{RG} : Angular Rotational Gripper Velocity;
α_{RG} : Angular Rotational Gripper Acceleration;
$\dot{\alpha}_{jRG}$: Angular Rotational Gripper Jerk;
v_{RG} : Tangential Curvilinear Rotational Gripper Velocity;
a_{RG} : Tangential Curvilinear Rotational Gripper Acceleration;
j_{RG} : Tangential Curvilinear Rotational Gripper Jerk;
v_{cx} : Horizontal Component of the Curvilinear Wedge Cam Contour Velocity;
a_{cx} : Horizontal Component of the Curvilinear Wedge Cam Contour Acceleration;
j_{cx} : Horizontal Component of the Curvilinear Wedge Cam Contour Jerk;
v_{cy} : Vertical Component of the Curvilinear Wedge Cam Contour Velocity;
a_{cy} : Vertical Component of the Curvilinear Wedge Cam Contour Acceleration;
j_{cy} : Vertical Component of the Curvilinear Wedge Cam Contour Jerk;
v_c : Resultant Curvilinear Wedge Cam Contour Velocity;
a_c : Resultant Curvilinear Wedge Cam Contour Acceleration;
j_c : Resultant Curvilinear Wedge Cam Contour Jerk;

3. Methodology

3.1. Kinematic Development of Parametric Inverse/Regular Wedge Cam Path

3.1.1. Specified/Driving and Calculated/Driven Fixed Analysis Variables

In connection with the prescribed nomenclature and Figure 1 below, the foundational kinematics regarding the cam profile will be mathematically derived for producing self-centering motion applicable to three-point contact about varying diameters of the workpiece within a specified size range.

Due to symmetry, the layout can be viewed as shown with the theoretical formulation comprising quadrants 1 and 4 about a global stationary coordinate system located at point O_1. In relation, there is an inverse (or regular) wedge cam/roller follower located at point D through which, when vertical movement

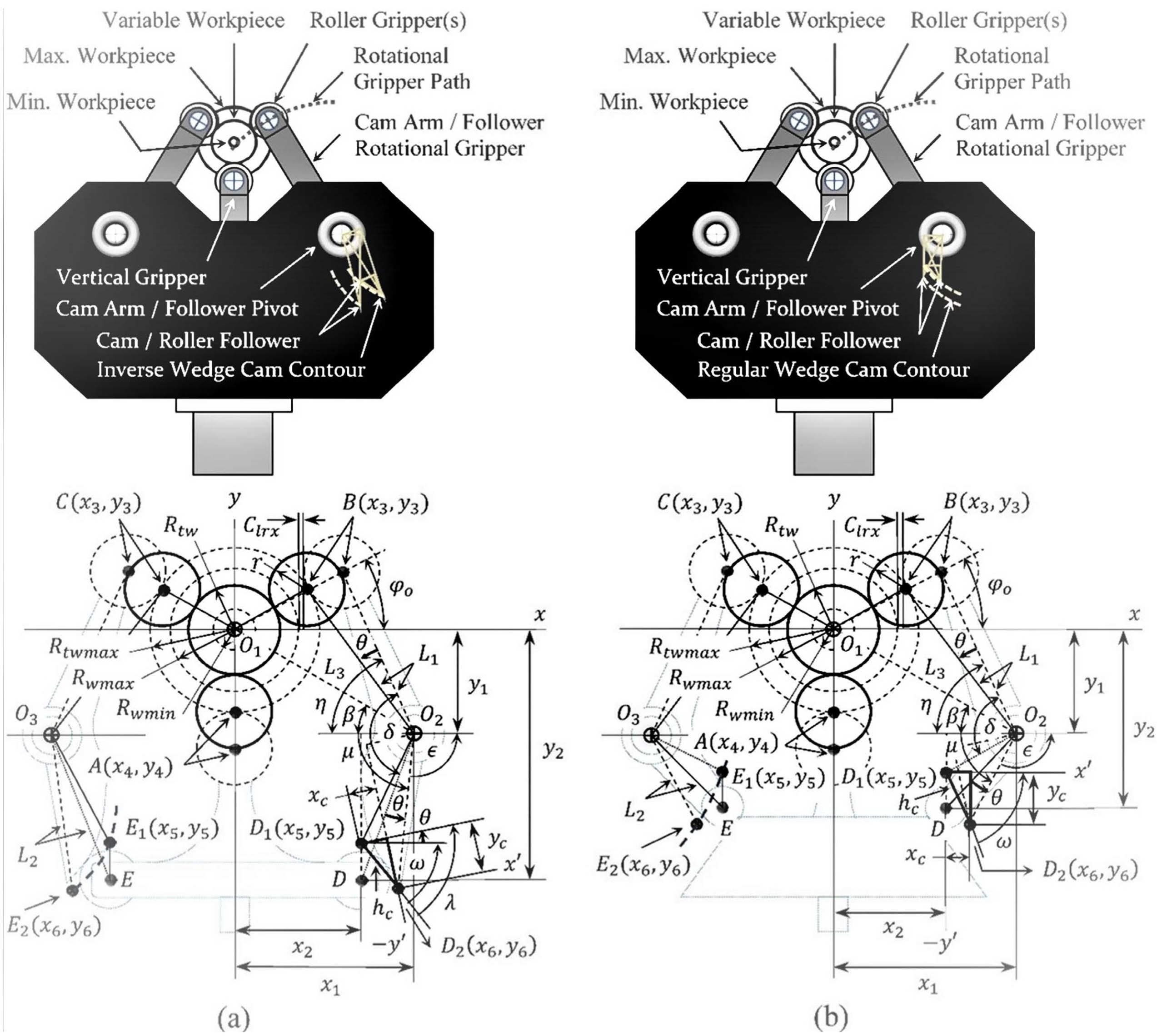

Figure 1. The kinematic self-centering motion layout (a) ınverse wedge cam, (b) regular wedge cam.

of the translational gripper/roller follower to point D_1 occurs in conjunction with rotation of the rotational gripper about point O_2, all three roller gripper diameters (located at points A, B, and C) will contact the theoretical workpiece diameter (located at point O_1) in a simultaneous tangent fashion thus achieving self-centering motion of this type.

The generalized self-centering cam derivation arising from the corresponding moving x' - y' coordinate system (starting at point D and incrementing through point D_2 (or D_1)—for the inverse (or regular) wedge cams respectively—over the cam rotation range required for tangential gripping of all three roller diameters) considers parameterization of the cam contour equations used for producing a path in the local x' - y' Cartesian coordinate system located at points D_2 (or D_1). For clarification, points D_2 (and D_1) are shown in **Figure 1(a)** (and **Figure 1(b)**), respectively, at an intermediate position of the total cam rotation range.

Regarding the kinematic motion and associated theoretical development, as shown in Section B of the nomenclature, several specified/driving analysis variables are prescribed. In connection, the independent variable is specified as the angle of cam rotation θ ranging from 0˚ to a maximum value that corresponds to the minimum workpiece diameter. However, and for convenience, maximum and minimum actual workpiece radii, R_{wmax} and R_{wmin}, are utilized rather than diameters when formulating the theoretical framework. Additionally, and important to note, the gripper roller radius parameter r may be interchanged with noncircular shapes by being consistent with vectors starting from points A, B, and C and ending at their outer edges of contact with the corresponding mating surface of the workpiece diameter.

Moreover, to broaden the practical aspects related to designing a satisfactory self-centering arrangement, a clearance allowance C_{lrx} is included. This horizontal component starts from the outermost tangential edge of the maximum actual workpiece diameter (along its horizontal axis) and ends at the outermost tangential edge of gripper rollers B (and C) (along their horizontal axes) in their initial configuration. In connection, and as an aid toward the development of an optimal design, an initial contact angle φ_o is utilized to establish the starting positions of gripper rollers B (and C) in alignment with the prescribed clearance and maximum actual workpiece radius.

Furthermore, for better visualization of the design specification and associated limits of the design space within an optimization environment, the starting positions of points O_2 and D are assigned as coordinate points (x_1, y_1) and (x_2, y_2) relative to the workpiece origin O_1. Lastly, and regarding a static and dynamic analyses integral to an extension of the kinematics theory for providing a generalized and holistic systems engineering approach to the design of such devices, the static friction coefficient μ_s, activation force F_a, given workpiece reaction forces and external moment components F_{wpx}, F_{wpy}, M_{extx}, M_{exty}, and M_{extz}, as well as the constant power source P_c are provided as specified design parameters.

In conjunction, and as preliminary specification toward the theoretical development of the wedge cam contour equations, the calculated/driven fixed analysis variables (in accordance with Section C of the nomenclature) are shown through the following equations.

With the horizontal clearance specification between the rotational gripper rollers as well as the maximum actual workpiece radius, the maximum theoretical workpiece radius R_{twmax} can be determined by Equation (1) below.

$$R_{twmax} = \frac{R_{wmax} + C_{lrx} + r}{\cos \varphi_o} - r \tag{1}$$

Note that the maximum theoretical workpiece radius provides an upper bound for the allowed range of the adjustable theoretical workpiece radius in which the gripper rollers theoretically contact and/or move through.

Additionally, various kinematic lengths are determined through the following equations.

$$L_1 = \sqrt{\left(x_1 - \left(R_{twmax} + r\right)\cos\varphi_o\right)^2 + \left(y_1 + \left(R_{twmax} + r\right)\sin\varphi_o\right)^2} \quad (2)$$

$$L_2 = \sqrt{\left(x_2 - x_1\right)^2 + \left(y_2 - y_1\right)^2} \quad (3)$$

$$L_3 = \sqrt{x_1^2 + y_1^2} \quad (4)$$

In connection, their associated angles are determined as follows:

$$\eta = \frac{\pi}{2} - \tan^{-1}\frac{x_1 - \left(R_{twmax} + r\right)\cos\varphi_o}{y_1 + \left(R_{twmax} + r\right)\sin\varphi_o} \quad (5)$$

$$\delta = \eta + \frac{\pi}{2} + \tan^{-1}\frac{x_2 - x_1}{y_2 - y_1} \quad (6)$$

$$\beta = \tan^{-1}\frac{y_1}{x_1} \quad (7)$$

3.1.2. Method 1: Trigonometry Applied to the Coordinate Points Design Layout

With having established the specified and calculated parameters within the previous discussion, nomenclature, and associated equations, the development of calculated/driven variable equations/analysis functions will be shown within the following presentment. To note, Section D of the nomenclature has been provided for use in conjunction with the following generalized theoretical formulations.

In reference to Figure 1, forward kinematic equations that describe the moving coordinate points A, B, D_1, and D_2 will be derived as a function of the cam rotation θ for use when developing the associated parametric wedge cam equations. Moreover, the corresponding formulation will be outlined through an analytical approach involving basic trigonometric concepts.

In deriving the forward kinematics, the following angles as a function of the cam rotation θ are presented.

$$\mu(\theta) = \delta - (\eta - \theta) \quad (8)$$

$$\epsilon(\theta) = \pi - \mu(\theta) \quad (9)$$

Furthermore, coordinates $x_3(\theta)$ and $y_3(\theta)$ for point B along with the associated theoretical workpiece radius $R_{tw}(\theta)$ are provided through Equations (10)-(12).

$$x_3(\theta) = x_1 - L_1\cos(\eta - \theta) \quad (10)$$

$$y_3(\theta) = L_1\sin(\eta - \theta) - y_1 \quad (11)$$

$$R_{tw}(\theta) = \sqrt{x_3^2(\theta) + y_3^2(\theta)} - r \quad (12)$$

Additionally, coordinates x_4 and $y_4(\theta)$ of the vertically translating roller located at point A are given below.

$$x_4 = 0 \quad (13)$$

$$y_4(\theta) = R_{tw}(\theta) + r \tag{14}$$

Moreover, coordinates $x_5(\theta)$ and $y_5(\theta)$ of the vertically translating cam roller follower located at point D_1 are given as follows.

$$x_5 = x_2 \tag{15}$$

$$y_5(\theta) = y_2 - \left(R_{twmax} - R_{tw}(\theta)\right) \tag{16}$$

Lastly, coordinates $x_6(\theta)$ and $y_6(\theta)$ for point D_2 are given by Equations (17) and (18).

$$x_6(\theta) = x_1 + L_2 \cos\epsilon(\theta) \tag{17}$$

$$y_6(\theta) = y_1 + L_2 \sin\epsilon(\theta) \tag{18}$$

With having the above theoretical foundation specification, parametric equations of the wedge cam contours can now be formulated as a function of their cam rotation. Several preliminary equations for defining the cam contour equations are as follows.

$$h_c(\theta) = \sqrt{\left(x_6(\theta) - x_5\right)^2 + \left(y_6(\theta) - y_5(\theta)\right)^2} \tag{19}$$

$$\omega(\theta) = \tan^{-1}\frac{y_6(\theta) - y_5(\theta)}{x_6(\theta) - x_5} \tag{20}$$

$$\lambda(\theta) = \theta + \omega(\theta) \tag{21}$$

Consequently, the components of the inverse and regular cam paths on the moving x' - y' coordinate system are provided by $x_c(\theta)$ and $y_c(\theta)$ through Equations (22) to (25) below. To note, subscripts i and r are used to distinguish between inverse and regular cam types.

$$x_{c_i}(\theta) = h_c(\theta)\cos\lambda(\theta) \tag{22}$$

$$y_{c_i}(\theta) = h_c(\theta)\sin\lambda(\theta) \tag{23}$$

$$x_{c_r}(\theta) = h_c(\theta)\cos\omega(\theta) \tag{24}$$

$$y_{c_r}(\theta) = h_c(\theta)\sin\omega(\theta) \tag{25}$$

While the above parametric equations are adequate for creating a useful design, they rely on incrementing the rotating gripper (angle of cam rotation) for developing the cam contour. However, and regarding a robotics & controls theory application among other potential theoretical uses in design and optimization, it may be useful to extend the parametric cam equations into rectangular form within the local Cartesian reference frame located at points D_2 (or D_1) for both cam types respectively.

In relation, and with taking the theoretical formulation of the backward kinematic cam rotation equation into consideration, the composition of the parametric cam equations in expanded form (with substitution of all related forward kinematic equations) contain trigonometric functions of unlike angles thereby presenting difficulties for isolating the cam rotation. Therefore, a combined loop-closure with vector projection/resolution method will be explored as an attempt to resolve this mathematical issue as well as to provide an alternative generalized approach for developing the parametric cam path equations which may prove useful and convenient within a robust design optimization context.

3.1.3. Method 2: Combined Loop-Closure with Vector Projection/Resolution Using Coordinate Points Design Layout

Regarding the combined loop-closure with vector projection/resolution formulation, two loop closures are superimposed onto each moving component of the self-centering mechanism in terms of both the translational and rotational grippers as shown in Figure 2 below.

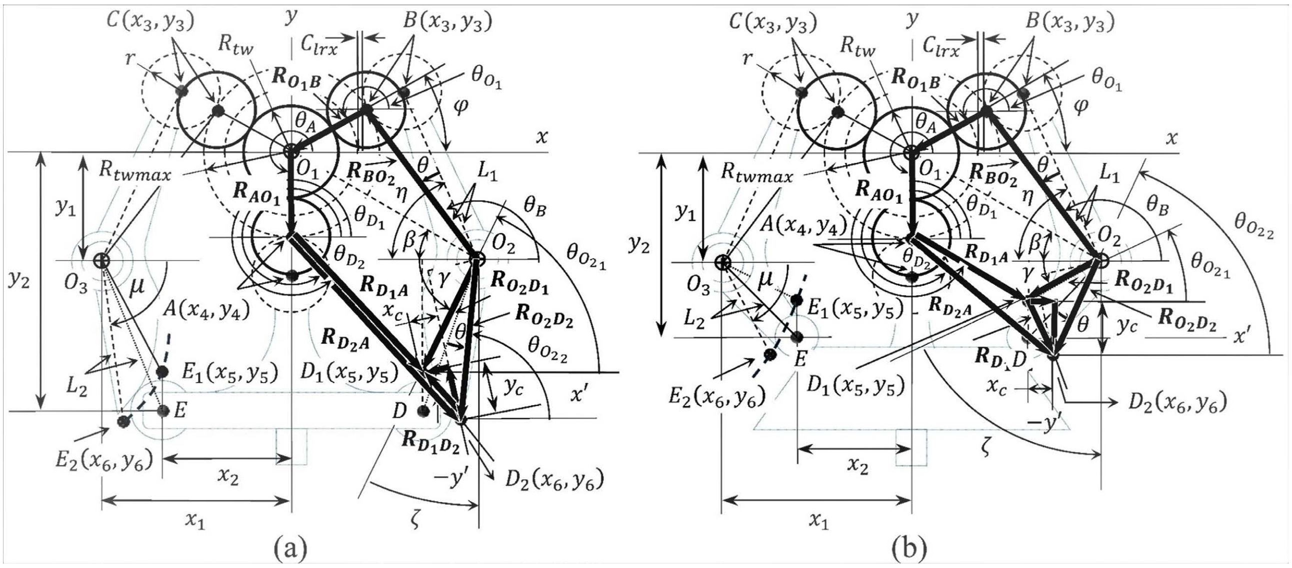

Figure 2. Combined loop-closure with vector projection/resolution layout (a) ınverse wedge cam, (b) regular wedge cam.

In connection, theoretical five-bar mechanisms are chosen for both loops in order to directly capture the contact angle and associated line of action of contact forces useful for design optimization tasks. Moreover, each of the five-bar mechanisms describe the vertical movement of point D_1 on the translational gripper and the rotation of point D_2 on the rotational gripper respectively. Due to this configuration in association with both loops sharing similar vectors in addition to a common point of contact for producing simultaneous translation and rotation thereby contributing to the moving coordinate system of the cam contour, the parametric cam contour equations can be developed through projection (or resolution) of related vector components onto this moving coordinate system at points D_2 (or D_1) along with taking their relative differences.

Following, a complex algebraic approach will be employed for deriving the vectors of the loop closures in terms of their coordinate points. To note, both loop closures start and end at point O_2 and are oriented in a counterclockwise fashion.

The vectors for the first loop are as follows.

$$\boldsymbol{R}_{BO_2}(\theta) = -\left(x_1 - x_3(\theta)\right) + \mathrm{i}\left(y_1 + y_3(\theta)\right) \tag{26}$$

$$\boldsymbol{R}_{O_1B}(\theta) = -x_3(\theta) - \mathrm{i}\,y_3(\theta) \tag{27}$$

$$\boldsymbol{R}_{AO_1}(\theta) = x_4 - \mathrm{i}\,y_4(\theta) \tag{28}$$

$$\boldsymbol{R}_{D_1A}(\theta) = (x_5 - x_4) - \mathrm{i}\left(y_5(\theta) - y_4(\theta)\right) \tag{29}$$

$$\boldsymbol{R}_{O_2D_1}(\theta) = (x_1 - x_5) + \mathrm{i}\left(y_5(\theta) - y_1\right) \tag{30}$$

The additional second loop vectors are defined below.

$$\boldsymbol{R}_{D_2A}(\theta) = \left(x_6(\theta) - x_4\right) - \mathrm{i}\left(y_6(\theta) - y_4(\theta)\right) \tag{31}$$

$$\boldsymbol{R}_{O_2D_2}(\theta) = \left(x_1 - x_6(\theta)\right) + \mathrm{i}\left(y_6(\theta) - y_1\right) \tag{32}$$

Consequently, the loop-closure equations for both loop closures are:

$$\boldsymbol{R}_{BO_2}(\theta) + \boldsymbol{R}_{O_1B}(\theta) + \boldsymbol{R}_{AO_1}(\theta) + \boldsymbol{R}_{D_1A}(\theta) + \boldsymbol{R}_{O_2D_1}(\theta) = 0 \tag{33}$$

$$\boldsymbol{R}_{BO_2}(\theta) + \boldsymbol{R}_{O_1B}(\theta) + \boldsymbol{R}_{AO_1}(\theta) + \boldsymbol{R}_{D_2A}(\theta) + \boldsymbol{R}_{O_2D_2}(\theta) = 0 \tag{34}$$

In alignment with a complex polar algebraic approach and from the above vector equations along with the following angles, the magnitudes and directions of the vectors can be determined through the use of absolute value and argument functions for complex numbers. However, note that several of the angles obtained from the argument function are equated to the contact angle among others for use when incorporating constraints within specialized design arrangements and the application of various techniques regarding optimization/multi-objective optimization.

$$\varphi(\theta) = \tan^{-1}\frac{y_3(\theta)}{x_3(\theta)} \tag{35}$$

$$\zeta(\theta) = \tan^{-1}\frac{x_5 - x_1}{y_5(\theta) - y_1} \tag{36}$$

$$\gamma(\theta) = \frac{\pi}{2} + \zeta(\theta) \tag{37}$$

Furthermore, and pertaining to the complex polar algebraic approach, the magnitudes and directions of the vectors are provided as shown through the following equations.

$$\vec{R}_{BO_2}(\theta)\angle\theta_B(\theta) = \sqrt{\left(x_1 - x_3(\theta)\right)^2 + \left(y_1 + y_3(\theta)\right)^2}\angle\pi - (\eta - \theta) \tag{38}$$

$$\vec{R}_{O_1B}(\theta)\angle\theta_{O_1}(\theta) = \sqrt{x_3^2(\theta) + y_3^2(\theta)}\angle\pi + \varphi(\theta) \tag{39}$$

$$\vec{R}_{AO_1}(\theta)\angle\theta_A = \sqrt{x_4^2(\theta)^2 + y_4^2(\theta)}\angle 3\frac{\pi}{2} \tag{40}$$

$$\vec{R}_{D_1A}(\theta)\angle\theta_{D_1}(\theta) = \sqrt{\left(x_5 - x_4\right)^2 + \left(y_5(\theta) - y_4(\theta)\right)^2}$$
$$\angle 2\pi - \tan^{-1}\frac{y_5(\theta) - y_4(\theta)}{x_5 - x_4} \tag{41}$$

$$\vec{R}_{O_2D_1}(\theta)\angle\theta_{O_{2_1}}(\theta)=\sqrt{(x_1-x_5)^2+(y_5(\theta)-y_1)^2}\angle\gamma(\theta) \tag{42}$$

$$\vec{R}_{D_2A}(\theta)\angle\theta_{D_2}(\theta)=\sqrt{(x_6(\theta)-x_4)^2+(y_6(\theta)-y_4(\theta))^2}$$
$$\angle 2\pi-\tan^{-1}\frac{y_6(\theta)-y_4(\theta)}{x_6(\theta)-x_4} \tag{43}$$

$$\vec{R}_{O_2D_2}(\theta)\angle\theta_{O_{2_2}}(\theta)=\sqrt{(x_1-x_6(\theta))^2+(y_6(\theta)-y_1)^2}\angle\mu(\theta) \tag{44}$$

To illustrate the incorporation of generalization into the loop-closure equations, the magnitudes and directions provided by the above equations are used in the following manner for converting the original vector formulation into standard complex algebraic form.

$$\boldsymbol{R}_{\boldsymbol{BO_2}}(\theta)=\vec{R}_{BO_2}(\theta)\cos\theta_B(\theta)+\mathrm{i}\vec{R}_{BO_2}(\theta)\sin\theta_B(\theta) \tag{45}$$

$$\boldsymbol{R}_{\boldsymbol{O_1B}}(\theta)=\vec{R}_{O_1B}(\theta)\cos\theta_{O_1}(\theta)+\mathrm{i}\vec{R}_{O_1B}(\theta)\sin\theta_{O_1}(\theta) \tag{46}$$

$$\boldsymbol{R}_{\boldsymbol{AO_1}}(\theta)=\vec{R}_{AO_1}(\theta)\cos\theta_A+\mathrm{i}\vec{R}_{AO_1}(\theta)\sin\theta_A \tag{47}$$

$$\boldsymbol{R}_{\boldsymbol{D_1A}}(\theta)=\vec{R}_{D_1A}(\theta)\cos\theta_{D_1}(\theta)+\mathrm{i}\vec{R}_{D_1A}(\theta)\sin\theta_{D_1}(\theta) \tag{48}$$

$$\boldsymbol{R}_{\boldsymbol{O_2D_1}}(\theta)=\vec{R}_{O_2D_1}(\theta)\cos\theta_{O_{2_1}}(\theta)+\mathrm{i}\vec{R}_{O_2D_1}(\theta)\sin\theta_{O_{2_1}}(\theta) \tag{49}$$

$$\boldsymbol{R}_{\boldsymbol{D_2A}}(\theta)=\vec{R}_{D_2A}(\theta)\cos\theta_{D2}(\theta)+\mathrm{i}\vec{R}_{D_2A}(\theta)\sin\theta_{D_2}(\theta) \tag{50}$$

$$\boldsymbol{R}_{\boldsymbol{O_2D_2}}(\theta)=\vec{R}_{O_2D_2}(\theta)\cos\theta_{O_{2_2}}(\theta)+\mathrm{i}\vec{R}_{O_2D_2}(\theta)\sin\theta_{O_{2_2}}(\theta) \tag{51}$$

With having derived the vector equations for both loop-closures, the magnitudes of vectors $\boldsymbol{R}_{\boldsymbol{O2\,D1}}(\theta)$ and $\boldsymbol{R}_{\boldsymbol{O2\,D2}}(\theta)$ are projected (or resolved) onto the x' - y' coordinate system at points D_2 (or D_1) for inverse (or regular) wedge cams respectively. The projected (or resolved) vectors are then combined through their difference(s) as shown within $\boldsymbol{R}_{\boldsymbol{D1\,D2}}(\theta)$ provided below.

$$\begin{aligned}\boldsymbol{R}_{\boldsymbol{D_1D_{2_i}}}(\theta)=&\left(\vec{R}_{O_2D_2}(\theta)\cos\left(\theta_{O_{2_2}}(\theta)-\theta\right)-\vec{R}_{O_2D_1}(\theta)\cos\left(\theta_{O_{2_1}}(\theta)-\theta\right)\right)\\&+\mathrm{i}\left(\vec{R}_{O_2D_2}(\theta)\sin\left(\theta_{O_{2_2}}(\theta)-\theta\right)-\vec{R}_{O_2D_1}(\theta)\sin\left(\theta_{O_{2_1}}(\theta)-\theta\right)\right)\end{aligned} \tag{52}$$

$$\boldsymbol{R}_{\boldsymbol{D_1D_{2_r}}}(\theta)=\left(x_6(\theta)-x_5\right)-\mathrm{i}\left(y_6(\theta)-y_5(\theta)\right) \tag{53}$$

Consequently, the components of $\boldsymbol{R}_{\boldsymbol{D1\,D2}}(\theta)$ are extracted for defining the parametric wedge cam equations for both design types.

$$x_{c_i}(\theta)=\vec{R}_{O_2D_2}(\theta)\cos\left(\theta_{O_{2_2}}(\theta)-\theta\right)-\vec{R}_{O_2D_1}(\theta)\cos\left(\theta_{O_{2_1}}(\theta)-\theta\right) \tag{54}$$

$$y_{c_i}(\theta)=\vec{R}_{O_2D_2}(\theta)\sin\left(\theta_{O_{2_2}}(\theta)-\theta\right)-\vec{R}_{O_2D_1}(\theta)\sin\left(\theta_{O_{2_1}}(\theta)-\theta\right) \tag{55}$$

$$x_{c_r}(\theta)=x_6(\theta)-x_5 \tag{56}$$

$$y_{c_r}(\theta)=-\left(y_6(\theta)-y_5(\theta)\right) \tag{57}$$

Concluding from the vector formulation of the cam path(s), the loop-closure equation for the inverse/regular wedge cam type is defined below by Equation

(59). Regarding this loop-closure equation, the vector $\boldsymbol{R}_{D1\,D2}(\theta)$ —Equation (52) for the inverse wedge cam—is resolved parallel to a stationary coordinate system located at point D and coincident with the cam follower point D_1 as shown through Equation (58). However, and for the regular wedge cam type, this vector is defined as Equation (53) and is inherently resolved parallel to the previously mentioned coordinate system and coincident with the cam follower point D_2 by definition of the regular wedge cam path. Therefore, an additional equation for the 'resolved' vector $\boldsymbol{R}_{D1\,D2}(\theta)$ is unnecessary for the regular wedge cam type.

$$\boldsymbol{R}_{D_1 D_{2_i}}(\theta) = \left(x_{c_i}(\theta)\cos\theta - y_{c_i}(\theta)\sin\theta\right) + \mathrm{i}\left(y_{c_i}(\theta)\cos\theta + x_{c_i}(\theta)\sin\theta\right) \quad (58)$$

$$\boldsymbol{R}_{D_1 D_2}(\theta) + \boldsymbol{R}_{O_2 D_1}(\theta) - \boldsymbol{R}_{O_2 D_2}(\theta) = 0 \quad (59)$$

Similarly to the basic trigonometric method, the parametric cam Equations (54) to (57) adequately define the inverse/regular cam contours. Contrary to the trigonometric method, the proper sense of the cam path components naturally arises from the vector equations. More importantly, it may be desired to use the combined loop-closure with vector projection/resolution method during robust design optimization tasks due to the convenience of such regarding utilization of the loop-closure summation from a constraint perspective as well as having the contact angle embedded within the vector formulation in relation to contact force transmissibility. However, the parametric cam Equations (54) and (55) in expanded form still does not provide a mathematical structure that enables an easy isolation of the cam rotation. Therefore, transformation equations (strictly based upon the cam rotation for this specific problem) will be used to reformulate the cam path and associated coordinate points for eliminating this complexity as well as to provide a natural extension toward generalization of the theoretical framework.

3.1.4. Method 3: Transformation Equations Applied to Coordinate Points Design Layout

Within the following, an analytical approach involving transformation equations will be applied to the kinematic coordinate points layout as shown in **Figure 3** below.

In the development of the cam path formulation utilizing this specific method, there are no preliminary variable angle equations necessary as that shown for the basic trigonometric and loop-closure methods. Therefore, the equations for the coordinate points derived from transformation equations are immediately presented.

Regarding this derivation, coordinates $x_3(\theta)$ and $y_3(\theta)$ for point B are provided through Equations (60) and (61).

$$\begin{aligned} x_3(\theta) = x_1 &- \left(x_1 - \left(R_{twmax} + r\right)\cos\varphi_o\right)\cos\theta \\ &- \left(y_1 + \left(R_{twmax} + r\right)\sin\varphi_o\right)\sin\theta \end{aligned} \quad (60)$$

$$\begin{aligned} y_3(\theta) = -y_1 &- \left(x_1 - \left(R_{twmax} + r\right)\cos\varphi_o\right)\sin\theta \\ &+ \left(y_1 + \left(R_{twmax} + r\right)\sin\varphi_o\right)\cos\theta \end{aligned} \quad (61)$$

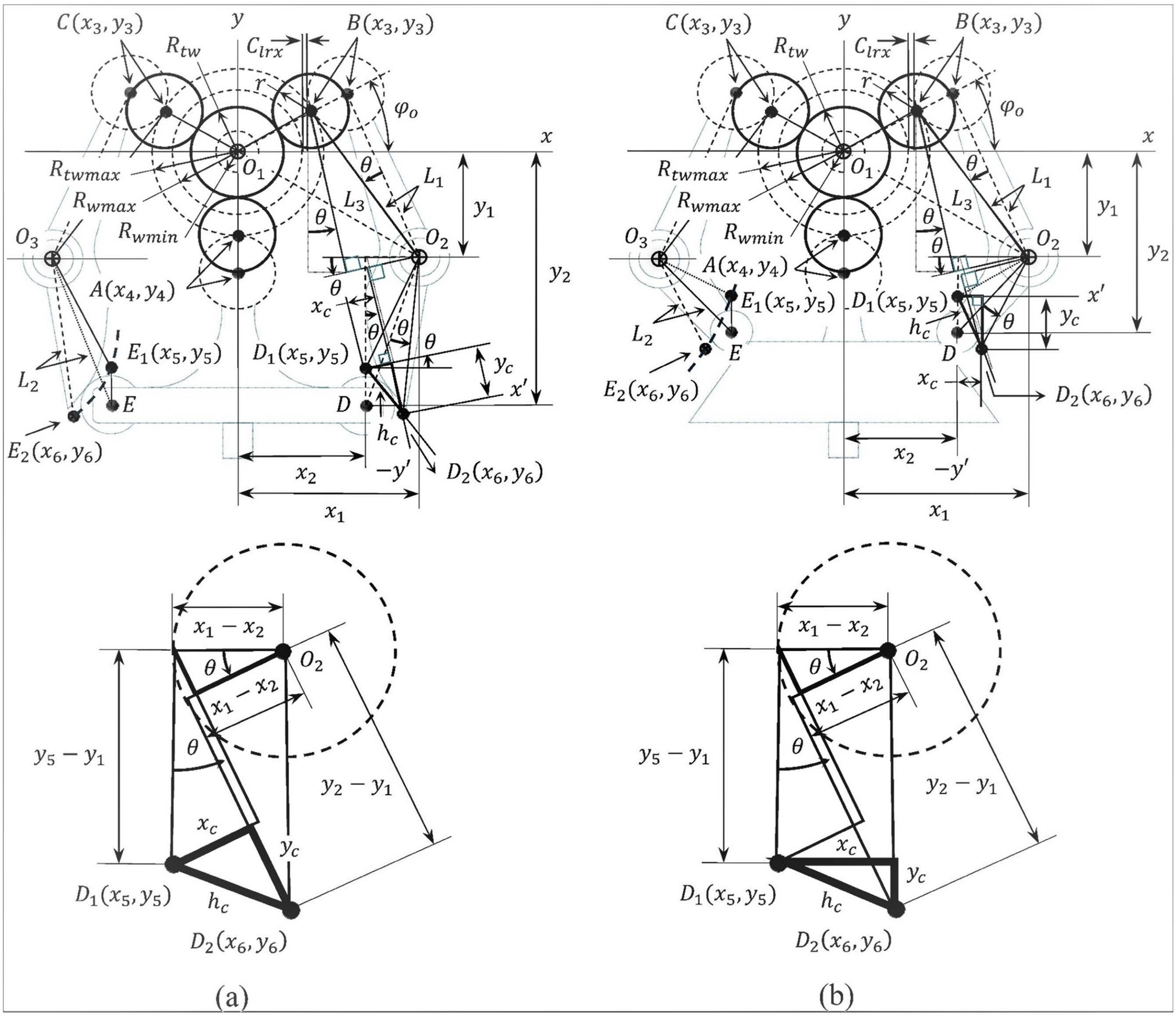

Figure 3. The transformation equations layout (a) inverse wedge cam, (b) regular wedge cam.

In conjunction, the theoretical workpiece radius $R_{tw}(\theta)$ from Equation (12) is presented below in expanded form regarding future isolation of the cam rotation.

$$
\begin{aligned}
&R_{tw}(\theta) = \sqrt{x_3^2(\theta) + y_3^2(\theta)} - r \Rightarrow \\
&- r + \surd\Big(L_3^2 - 2x_1\cos\theta\big(x_1 - (r + R_{twmax})\cos\varphi_o\big) + \big(x_1 - (r + R_{twmax})\cos\varphi_o\big)^2 \\
&+ 2y_1\big(x_1 - (r + R_{twmax})\cos\varphi_o\big)\sin\theta - 2y_1\cos\theta\big(y_1 + (r + R_{twmax})\sin\varphi_o\big) \\
&- 2x_1\sin\theta\big(y_1 + (r + R_{twmax})\sin\varphi_o\big) + \big(y_1 + (r + R_{twmax})\sin\varphi_o\big)^2\Big)
\end{aligned}
\tag{62}
$$

Additionally, coordinate $y_4(\theta)$ of the vertically translating roller located at point A is given below in expanded form. Note that the horizontal coordinate for this component is given by Equation (13) ($x_4 = 0$).

$$
\begin{aligned}
& y_4(\theta) = R_{tw}(\theta) + r \Rightarrow \\
& \surd\Big(L_3^2 - 2x_1 \cos\theta\big(x_1 - (r + R_{twmax})\cos\varphi_o\big) + \big(x_1 - (r + R_{twmax})\cos\varphi_o\big)^2 \\
& + 2y_1\big(x_1 - (r + R_{twmax})\cos\varphi_o\big)\sin\theta - 2y_1\cos\theta\big(y_1 + (r + R_{twmax})\sin\varphi_o\big) \\
& - 2x_1 \sin\theta\big(y_1 + (r + R_{twmax})\sin\varphi_o\big) + \big(y_1 + (r + R_{twmax})\sin\varphi_o\big)^2\Big)
\end{aligned} \tag{63}
$$

Furthermore, coordinate $y_5(\theta)$ of the vertically translating cam roller follower located at point D_1 is given below in expanded form. Note that the horizontal coordinate for this point is given by Equation (15) ($x_5 = x_2$).

$$
\begin{aligned}
& y_5(\theta) = y_2 - \big(R_{twmax} - R_{tw}(\theta)\big) \Rightarrow \\
& y_2 - \Big(R_{twmax} - \Big(-r + \surd\Big(L_3^2 - 2x_1\cos\theta\big(x_1 - (r + R_{twmax})\cos\varphi_o\big) \\
& + \big(x_1 - (r + R_{twmax})\cos\varphi_o\big)^2 + 2y_1\big(x_1 - (r + R_{twmax})\cos\varphi_o\big)\sin\theta \\
& - 2y_1\cos\theta\big(y_1 + (r + R_{twmax})\sin\varphi_o\big) \\
& - 2x_1\sin\theta\big(y_1 + (r + R_{twmax})\sin\varphi_o\big) + \big(y_1 + (r + R_{twmax})\sin\varphi_o\big)^2\Big)\Big)\Big)
\end{aligned} \tag{64}
$$

Lastly, coordinates $x_6(\theta)$ and $y_6(\theta)$ for point D_2 are given by Equations (65) and (66).

$$
x_6(\theta) = x_1 + (x_2 - x_1)\cos\theta + (y_2 - y_1)\sin\theta \tag{65}
$$

$$
y_6(\theta) = y_1 - (x_2 - x_1)\sin\theta + (y_2 - y_1)\cos\theta \tag{66}
$$

With having the above derivation for the coordinate points, the parametric inverse/regular wedge cam equations are as follows.

$$
\begin{aligned}
& x_{c_i}(\theta) = (x_2 - x_1) - (x_2 - x_1)\cos\theta + \big(y_5(\theta) - y_1\big)\sin\theta \Rightarrow \\
& (x_2 - x_1) - (x_2 - x_1)\cos\theta + \Big(y_2 - \Big(R_{twmax} - \Big(-r + \surd\Big(L_3^2 \\
& - 2x_1\cos\theta\big(x_1 - (R_{twmax} + r)\cos\varphi_o\big) + \big(x_1 - (R_{twmax} + r)\cos\varphi_o\big)^2 \\
& + 2y_1\big(x_1 - (R_{twmax} + r)\cos\varphi_o\big)\sin\theta - 2y_1\cos\theta\big(y_1 + (R_{twmax} + r)\sin\varphi_o\big) \\
& - 2x_1\sin\theta\big(y_1 + (R_{twmax} + r)\sin\varphi_o\big) + \big(y_1 + (R_{twmax} + r)\sin\varphi_o\big)^2\Big)\Big)\Big) - y_1\Big)\sin\theta
\end{aligned} \tag{67}
$$

$$
\begin{aligned}
& y_{c_i}(\theta) = (y_2 - y_1) - (x_2 - x_1)\sin\theta - \big(y_5(\theta) - y_1\big)\cos\theta \Rightarrow \\
& (y_2 - y_1) - (x_2 - x_1)\sin\theta - \Big((x_2 - x_1) - (x_2 - x_1)\cos\theta \\
& + \Big(y_2 - \Big(R_{twmax} - \Big(-r + \surd\Big(L_3^2 - 2x_1\cos\theta\big(x_1 - (R_{twmax} + r)\cos\varphi_o\big) \\
& + \big(x_1 - (R_{twmax} + r)\cos\varphi_o\big)^2 + 2y_1\big(x_1 - (R_{twmax} + r)\cos\varphi_o\big)\sin\theta \\
& - 2y_1\cos\theta\big(y_1 + (R_{twmax} + r)\sin\varphi_o\big) - 2x_1\sin\theta\big(y_1 + (R_{twmax} + r)\sin\varphi_o\big) \\
& + \big(y_1 + (R_{twmax} + r)\sin\varphi_o\big)^2\Big)\Big)\Big) - y_1\Big)\sin\theta - y_1\Big)\cos\theta
\end{aligned} \tag{68}
$$

$$
x_{c_r}(\theta) = x_6(\theta) - x_2 \Rightarrow x_1 - x_2 + (x_2 - x_1)\cos\theta + (y_2 - y_1)\sin\theta \tag{69}
$$

$$\begin{aligned} y_{c_r}(\theta) &= y_6(\theta) - y_5(\theta) \Rightarrow (y_1 - y_2) - (x_2 - x_1)\sin\theta + (y_2 - y_1)\cos\theta \\ &+ (R_{twmax} + r) - \surd\Big(L_3^2 - 2x_1\cos\theta\big(x_1 - (R_{twmax} + r)\cos\varphi_o\big) \\ &+ \big(x_1 - (R_{twmax} + r)\cos\varphi_o\big)^2 + 2y_1\big(x_1 - (R_{twmax} + r)\cos\varphi_o\big)\sin\theta \\ &- 2y_1\cos\theta\big(y_1 + (R_{twmax} + r)\sin\varphi_o\big) - 2x_1\sin\theta\big(y_1 + (R_{twmax} + r)\sin\varphi_o\big) \\ &+ \big(y_1 + (R_{twmax} + r)\sin\varphi_o\big)^2\Big) \end{aligned} \tag{70}$$

Due to the way in which transformation equations are applied to this specific problem, the mathematical structure of the parametric cam Equations (67) to (70) are satisfactory for the development of backward kinematic cam rotation equations.

3.1.5. Related Other: Spatial Derivatives of the Parametric Cam Equations

Prior to advancing into the backward kinematic cam rotation equation formulation, the spatial derivatives of the cam Equations (67) to (70) are computed for future use when exploring nonlinear ordinary differential equations, static equilibrium equations, and cam dynamics. To note, the spatial derivatives of Equations (67), (68), and (70) over the cam rotation result in very complicated equations. Due to such, there are common terms found within the derivative equations that are extracted and correlated to $y_4(\theta)$ as well as to several summation wave equations congruent with expressions that are encountered within the simulated unified resultant amplitude method (URAM) prescribed in [46].

In connection, sinusoidal amplitude parameters associated with the summation wave equations for both cam types used for condensing the derivatives are:

$$a_{1_i}(\theta) = y_4(\theta) + y_2 - y_1 - R_{twmax} - r \tag{71}$$

$$b_{1_i} = x_2 - x_1 \tag{72}$$

$$a_{2_i} = 2y_1\big(x_1 - (R_{twmax} + r)\cos\varphi_o\big) \tag{73}$$

$$b_{2_i} = 2x_1\big(x_1 - (R_{twmax} + r)\cos\varphi_o\big) \tag{74}$$

$$a_{3_i} = -2x_1\big(y_1 + (R_{twmax} + r)\sin\varphi_o\big) \tag{75}$$

$$b_{3_i} = 2y_1\big(y_1 + (R_{twmax} + r)\sin\varphi_o\big) \tag{76}$$

$$a_{1_r} = 2y_1\big(x_1 - (R_{twmax} + r)\cos\varphi_o\big) \tag{77}$$

$$b_{1_r} = 2x_1\big(x_1 - (R_{twmax} + r)\cos\varphi_o\big) \tag{78}$$

$$a_{2_r} = -2x_1\big(y_1 + (R_{twmax} + r)\sin\varphi_o\big) \tag{79}$$

$$b_{2_r} = 2y_1\big(y_1 + R_{twmax} + r\big)\sin\varphi_o) \tag{80}$$

Therefore, the corresponding summation wave equations are:

$$c_{w_{1_i}}(\theta) = a_{1_i}(\theta)\cos\theta + b_{1_i}\sin\theta \tag{81}$$

$$c_{w_{2_i}} = a_{2_i}\cos\theta + b_{2_i}\sin\theta \tag{82}$$

$$c_{w_{3_i}} = a_{3_i}\cos\theta + b_{3_i}\sin\theta \tag{83}$$

$$c_{w_{4_i}} = b_{2_i} \cos\theta - a_{2_i} \sin\theta \quad (84)$$

$$c_{w_{5_i}} = b_{3_i} \cos\theta - a_{3_i} \sin\theta \quad (85)$$

$$c_{w_{6_i}}(\theta) = -b_{1_i} \cos\theta + a_{1_i}(\theta)\sin\theta \quad (86)$$

$$c_{w_{1_r}}(\theta) = a_{1_r} \cos\theta + b_{1_r} \sin\theta \quad (87)$$

$$c_{w_{2_r}} = a_{2_r} \cos\theta + b_{2_r} \sin\theta \quad (88)$$

$$c_{w_{3_r}} = b_{1_r} \cos\theta - a_{1_r} \sin\theta \quad (89)$$

$$c_{w_{4_r}} = b_{2_r} \cos\theta - a_{2_r} \sin\theta \quad (90)$$

With having the summation wave equations, the condensed spatial horizontal cam path component derivatives for both cam types are:

$$\frac{\mathrm{d}x_{c_i}(\theta)}{\mathrm{d}\theta} = c_{w_{1_i}}(\theta) + \frac{\left(c_{w_{2i}} + c_{w_{3_i}}\right)\sin\theta}{2y_4(\theta)} \quad (91)$$

$$\frac{\mathrm{d}^2 x_{c_i}(\theta)}{\mathrm{d}\theta^2} = -c_{w_{6_i}}(\theta) + \frac{\left(c_{w_{2_i}} + c_{w_{3_i}}\right)\cos\theta}{y_4(\theta)} + \left(\frac{c_{w_{4_i}} + c_{w_{5_i}}}{2y_4(\theta)} - \frac{\left(c_{w_{2_i}} + c_{w_{3_i}}\right)^2}{4y_4(\theta)^3}\right)\sin\theta \quad (92)$$

$$\begin{aligned} \frac{\mathrm{d}^3 x_{c_i}(\theta)}{\mathrm{d}\theta^3} = &-c_{w_{1_i}}(\theta) + \left(-\frac{3\left(c_{w_{2_i}} + c_{w_{3_i}}\right)^2}{4y_4(\theta)^3} + \frac{3\left(c_{w_{4_i}} + c_{w_{5_i}}\right)}{2y_4(\theta)}\right)\cos\theta \\ &+ \left(\frac{3\left(c_{w_{2_i}} + c_{w_{3i}}\right)^3}{8y_4(\theta)^5} - \frac{3\left(c_{w_{2_i}} + c_{w_{3_i}}\right)\left(c_{w_{4_i}} + c_{w_{5_i}}\right)}{4y_4(\theta)^3}\right. \\ &\left. - \frac{c_{w_{2_i}} + c_{w_{3_i}}}{2y_4(\theta)} - \frac{3\left(c_{w_{2_i}} + c_{w_{3_i}}\right)}{2y_4(\theta)}\right)\sin\theta \end{aligned} \quad (93)$$

$$\frac{\mathrm{d}x_{c_r}(\theta)}{\mathrm{d}\theta} = (y_2 - y_1)\cos\theta - (x_2 - x_1)\sin\theta \quad (94)$$

$$\frac{\mathrm{d}^2 x_{c_r}(\theta)}{\mathrm{d}\theta^2} = -(x_2 - x_1)\cos\theta - (y_2 - y_1)\sin\theta \quad (95)$$

$$\frac{\mathrm{d}^3 x_{c_r}(\theta)}{\mathrm{d}\theta^3} = -(y_2 - y_1)\cos\theta + (x_2 - x_1)\sin\theta \quad (96)$$

Additionally, the condensed spatial vertical cam path component derivatives are:

$$\frac{\mathrm{d}y_{c_i}(\theta)}{\mathrm{d}\theta} = c_{w_{6_i}}(\theta) - \frac{\left(c_{w_{2i}} + c_{w_{3_i}}\right)\cos\theta}{2y_4(\theta)} \quad (97)$$

$$\frac{\mathrm{d}^2 y_{c_i}(\theta)}{\mathrm{d}\theta^2} = c_{w_{1_i}}(\theta) + \frac{\left(c_{w_{2_i}} + c_{w_{3_i}}\right)\sin\theta}{y_4(\theta)} + \left(\frac{\left(c_{w_{2_i}} + c_{w_{3_i}}\right)^2}{4y_4(\theta)^3} + \frac{-c_{w_{4i}} - c_{w_{5_i}}}{2y_4(\theta)}\right)\cos\theta \quad (98)$$

$$\frac{\mathrm{d}^3 y_{c_i}(\theta)}{\mathrm{d}\theta^3} = -c_{w_{6_i}}(\theta) + \left(-\frac{3\left(c_{w_{2_i}} + c_{w_{3_i}}\right)^3}{8 y_4(\theta)^5} + \frac{3\left(c_{w_{2i}} + c_{w_{3_i}}\right)\left(c_{w_{4i}} + c_{w_{5_i}}\right)}{4 y_4(\theta)^3} + \frac{2\left(c_{w_{2_i}} + c_{w_{3_i}}\right)}{y_4(\theta)} \right)\cos\theta + \left(-\frac{3\left(c_{w_{2_i}} + c_{w_{3_i}}\right)^2}{4 y_4(\theta)^3} + \frac{3\left(c_{w_{4_i}} + c_{w_{5_i}}\right)}{2 y_4(\theta)} \right)\sin\theta \tag{99}$$

$$\frac{\mathrm{d} y_{c_r}(\theta)}{\mathrm{d}\theta} = -(x_2 - x_1)\cos\theta - (y_2 - y_1)\sin\theta - \frac{c_{w_{1_r}}(\theta) + c_{w_{2r}}}{2 y_4(\theta)} \tag{100}$$

$$\frac{\mathrm{d}^2 y_{c_r}(\theta)}{\mathrm{d}\theta^2} = (x_2 - x_1)\sin\theta - (y_2 - y_1)\cos\theta + \frac{\left(c_{w_{1_r}}(\theta) + c_{w_{2_r}}\right)^2}{4 y_4(\theta)^3} - \frac{c_{w_{3_r}} + c_{w_{4_r}}}{2 y_4(\theta)} \tag{101}$$

$$\frac{\mathrm{d}^3 y_{c_r}(\theta)}{\mathrm{d}\theta^3} = (x_2 - x_1)\cos\theta + (y_2 - y_1)\sin\theta - \frac{3\left(c_{w_{1_r}}(\theta) + c_{w_{2_r}}\right)^3}{8 y_4(\theta)^5} + \frac{3\left(c_{w_{1_r}}(\theta) + c_{w_{2_r}}\right)\left(c_{w_{3r}} + c_{w_{4_r}}\right)}{4 y_4(\theta)^3} + \frac{c_{w_{1_r}}(\theta) + c_{w_{2_r}}}{2 y_4(\theta)} \tag{102}$$

Combined with the transformation parametric cam equations and associated spatial derivatives, backward kinematic cam rotation equations in terms of the horizontal cam path component will commence through incorporation of both approximation and exact methods.

3.2. Backward Kinematic Cam Rotation Equations

3.2.1. Developing a Solvable Equation

Backward kinematic cam rotation equations are used for converting the parametric cam contour equations into rectangular form through substitution of $\theta(x_c)$ into the equation $y_c(\theta)$. For inverting $x_c(\theta)$ into $\theta(x_c)$, Equation (67) is rearranged in a manner that eliminates the radical, and Equation (69) is rearranged in a similar form for comparative convenience. The rearranged equations are provided below.

$$\begin{aligned} \mathrm{eqn}_i\left(\theta, x_{c_i}\right) &= \left(y_4(\theta)\sin\theta\right)^2 - \left(x_1 - x_2 + x_{c_i} + (-x_1 + x_2)\cos\theta \right. \\ &\quad \left. + \left(R_{twmax} + r + y_1 - y_2\right)\sin\theta\right)^2 \\ &\equiv 0 \end{aligned} \tag{103}$$

$$\mathrm{eqn}_r\left(\theta, x_{c_r}\right) = x_1 - x_2 - x_{c_r} + (x_2 - x_1)\cos\theta + (y_2 - y_1)\sin\theta \equiv 0 \tag{104}$$

To note, Equations (103) and (104) are presented in two variables, θ and x_c, where θ must be isolated. This results in a contour plot of the equation with a family of curves representing $\mathrm{eqn}(\theta, x_c)$ and with the curve of interest being specified where $\mathrm{eqn}(\theta, x_c) = 0$ for determining the roots.

For isolating the cam rotation θ, the eleventh order Taylor series expansion and the trigonometric substitution & transformation method will be applied to

$\text{eqn}(\theta, x_c)$ for deriving the corresponding approximate and exact backward kinematic equations.

3.2.2. Method 1: The Taylor Series Expansion

The Taylor series approach is applied to the framework of the theoretical arrangement for developing an approximation of the cam rotation equation. With the origin of expansion starting at $\theta_o = 0$, the eleventh order series expansion of $\text{eqn}(\theta, x_c)$ relative to θ yields an eleventh order polynomial approximation. The resulting approximation for the inverse wedge cam is given by Equation (117) with its Taylor series coefficients being defined by Equations (105) through (116) and with the resulting approximation for the regular wedge cam being defined by Equation (118).

$$\begin{aligned} c_{11}(x_{c_i}) = \frac{1}{19958400}\Big(&-\big((1023(x_1 - x_2) - x_{c_i})(R_{twmax} + r + y_1 - y_2)\big) \\ &- 44286(R_{twmax} + r)(y_1 \cos\varphi_o + x_1 \sin\varphi_o)\Big) \end{aligned} \tag{105}$$

$$\begin{aligned} c_{10}(x_{c_i}) = \frac{1}{1814400}\Big(&-13995x_1^2 + x_2(255x_2 + x_{c_i}) - x_1(510x_2 + x_{c_i}) \\ &+ 2(-256(R_{twmax} + r) - 7253y_1)y_1 + 512(R_{twmax} + r + y_1)y_2 \\ &- 256y_2^2 + 14250(R_{twmax} + r)(x_1 \cos\varphi_o - y_1 \sin\varphi_o)\Big) \end{aligned} \tag{106}$$

$$\begin{aligned} c_9(x_{c_i}) = \frac{1}{181440}\Big(&(255(x_1 - x_2) - x_{c_i})(R_{twmax} + r + y_1 - y_2) \\ &+ 4920(R_{twmax} + r)(y_1 \cos\varphi_o + x_1 \sin\varphi_o)\Big) \end{aligned} \tag{107}$$

$$\begin{aligned} c_8(x_{c_i}) = \frac{1}{20160}\Big(&1449x_1^2 - x_2(63x_2 + x_{c_i}) + x_1(126x_2 + x_{c_i}) \\ &+ 8\big(y_1(16(R_{twmax} + r) + 197y_1) - 16(R_{twmax} + r + y_1)y_2 + 8y_2^2\big) \\ &+ 1512(R_{twmax} + r)(-x_1 \cos\varphi_o + y_1 \sin\varphi_o)\Big) \end{aligned} \tag{108}$$

$$\begin{aligned} c_7(x_{c_i}) = \frac{1}{2520}\Big(&-\big((63(x_1 - x_2) - x_{c_i})(R_{twmax} + r + y_1 - y_2)\big) \\ &- 546(r + R_{twmax})(y_1 \cos\varphi_o + x_1 \sin\varphi_o)\Big) \end{aligned} \tag{109}$$

$$\begin{aligned} c_6(x_{c_i}) = \frac{1}{360}\Big(&-135x_1^2 + x_2(15x_2 + x_{c_i}) - x_1(30x_2 + x_{ci}) \\ &- 2y_1(16(R_{twmax} + r) + 83y_1) + 32(R_{twmax} + r + y_1)y_2 \\ &- 16y_2^2 + 150(R_{twmax} + r)(x_1 \cos\varphi_o - y_1 \sin\varphi_o)\Big) \end{aligned} \tag{110}$$

$$\begin{aligned} c_5(x_{ci}) = \frac{1}{60}\Big(&(15(x_1 - x_2) - x_{c_i})(R_{twmax} + r + y_1 - y_2) \\ &+ 60(R_{twmax} + r)(y_1 \cos\varphi_o + x_1 \sin\varphi_o)\Big) \end{aligned} \tag{111}$$

$$\begin{aligned} c_4(x_{c_i}) = \frac{1}{12}\Big(&9x_1^2 - x_2(3x_2 + x_{c_i}) + x_1(6x_2 + x_{c_i}) \\ &+ 8y_1(R_{twmax} + r + 2y_1) - 8(R_{twmax} + r + y_1)y_2 \\ &+ 4y_2^2 + 12(R_{twmax} + r)(-x_1 \cos\varphi_o + y_1 \sin\varphi_o)\Big) \end{aligned} \tag{112}$$

$$c_3\left(x_{c_i}\right)=\frac{1}{3}\Big(-\Big(\big(3\left(x_1-x_2\right)-x_{c_i}\big)\left(R_{twmax}+r+y_1-y_2\right)\Big) \\ -6\left(R_{twmax}+r\right)\left(y_1\cos\varphi_o+x_1\sin\varphi_o\right)\Big) \tag{113}$$

$$c_2\left(x_{c_i}\right)=\left(x_2-x_1\right)x_{c_i}+\left(y_2-y_1\right)\left(2\left(R_{twmax}+r\right)+y_1-y_2\right) \tag{114}$$

$$c_1\left(x_{c_i}\right)=-2x_{c_i}\left(R_{twmax}+r+y_1-y_2\right) \tag{115}$$

$$c_0\left(x_{c_i}\right)=-x_{c_i}^2 \tag{116}$$

$$\begin{aligned} f_i\left(\theta,x_{c_i}\right)=&\,c_{11}\left(x_{c_i}\right)\theta^{11}+c_{10}\left(x_{c_i}\right)\theta^{10}+c_9\left(x_{c_i}\right)\theta^9+c_8\left(x_{c_i}\right)\theta^8 \\ &+c_7\left(x_{c_i}\right)\theta^7+c_6\left(x_{ci}\right)\theta^6+c_5\left(x_{c_i}\right)\theta^5+c_4\left(x_{c_i}\right)\theta^4 \\ &+c_3\left(x_{c_i}\right)\theta^3+c_2\left(x_{c_i}\right)\theta^2+c_1\left(x_{c_i}\right)\theta+c_0\left(x_{c_i}\right) \\ \equiv&\,0 \end{aligned} \tag{117}$$

$$\begin{aligned} f_r\left(\theta,x_{cr}\right)=&\,\frac{y_1-y_2}{11!}\theta^{11}+\frac{x_1-x_2}{10!}\theta^{10}+\frac{y_2-y_1}{9!}\theta^9+\frac{x_2-x_1}{8!}\theta^8 \\ &+\frac{y_1-y_2}{7!}\theta^7+\frac{x_1-x_2}{6!}\theta^6+\frac{y_2-y_1}{5!}\theta^5+\frac{x_2-x_1}{4!}\theta^4 \\ &+\frac{y_1-y_2}{3!}\theta^3+\frac{x_1-x_2}{2!}\theta^2+\left(y_2-y_1\right)\theta-x_{c_r} \\ \equiv&\,0 \end{aligned} \tag{118}$$

While an eleventh order approximation may appear rather large when considering a regression analysis of the actual cam path, it is necessary for generalizing and accurately approximating the angle of cam rotation over a bounded range of $0^\circ\le\theta\le 90^\circ$. In the application of the Taylor series approach, note that the specified series requires angles to be in radians.

In connection, the backward kinematic cam rotation equation can be solved by taking the roots of the polynomial $f\left(\theta,x_c\right)$. There are eleven different real/complex roots that satisfy the corresponding eleventh order polynomial. In view of polynomial algebra, the roots can be determined numerically through synthetic division, Newton's method, and software programming to name a few. To note, only a single root out of the many different roots (on a pointwise basis) pertains to the cam rotation equation associated with the self-centering arrangement and given design parameters. However, the designer must be aware if, and when, the root solution number changes from one to another depending on the portion of the cam path being considered.

Moreover, matters of deriving closed-form equations for fifth and greater order polynomial roots are entirely too complex for theoretically determining the cam rotation equation. Therefore, due to the theoretical complexity involved, experimental evaluation via numerical methods for solving the roots of the polynomial are required. In connection, most root solutions pertaining to this particular self-centering theory can only be represented programmatically through symbolic form rather than through closed-form solutions.

Consequently, with the use of matching methods and/or a graphical approach, the appropriate root solution(s) can be selected. For example, the variable x_c can be numerically quantified through an evaluation of its parametric cam equation by using a specified value for the cam rotation and substituting this value into Equations (105) through (116) for determining the polynomial coefficients of Equation (117) for the inverse wedge cam (and substituting the same value into Equation (118) for the regular wedge cam). Thereafter, the numerical root solution can be solved through the quantified polynomial and compared against the chosen value of the cam rotation to find the closest match.

From a graphical perspective, a horizontal line can be drawn on the contour plot of $f(\theta, x_c)$ at the calculated value for x_c (at a chosen angle within the design range) whereby the roots of this function correspond to points along this line where the angle of cam rotation intersects both the line and the contour of the function $f(\theta, x_c) = 0$. Determination of the appropriate root through the contour plot provides a direct approach since the desired root is present within the applicable range of $0 \le \theta \le \theta_{max}$ along the actual x_c vs. θ curve.

Nevertheless, and for eliminating inaccuracies involved within the Taylor series approach, an exact mathematical formulation of the backward kinematic cam rotation equation will be derived through an approach involving trigonometric substitution & transformation.

3.2.3. Method 2: Trigonometric Substitution & Transformation (TS&T)

Trigonometric substitution, specific to the parametric cam contour equations developed from the transformation equations method, involves a replacement of the cosine and sine functions found within Equations (103) and (104) for their universal trigonometric identities where both are in terms of the half-angle tangent function. As a consequence of such, transformation arises when using Equations (119) and (120) for the theta Θ (trigonometric numerator) and gamma Γ (trigonometric denominator) parameters thereby illustrating the similarity between the universal identities defined by Equations (121) and (123).

$$\Theta = \tan \theta/2 \tag{119}$$

$$\Gamma = 1 + \Theta^2 \tag{120}$$

$$\sin \theta \equiv \frac{2\tan \theta/2}{1+\tan^2 \theta/2} \Rightarrow \frac{2\Theta}{\Gamma} \tag{121}$$

$$\cos \theta \equiv \frac{1-\tan^2 \theta/2}{1+\tan^2 \theta/2} \Rightarrow \frac{1-\Theta^2}{\Gamma} \tag{122}$$

This exact mathematical method being presented transforms Equations (103) and (104) into polynomial form as shown by Equation (130) with its coefficients defined by Equations (123) through (129) for the inverse wedge cam (and by Equation (131) for the regular wedge cam). The associated polynomial roots of Equation (130) provide several solution(s), and Equation (131) provides two solution(s) for the theta parameter Θ. Additionally, isolation of the cam rotation arises when utilizing the combination of Equations (130) and (132) with Equation

(119) in terms of the polynomial root Θ as shown through Equation (133).

$$c_6\left(x_{c_i}\right) = -\left(2\left(x_1 - x_2\right) + x_{c_i}\right)^2 \tag{123}$$

$$c_5\left(x_{c_i}\right) = -4\left(2\left(x_1 - x_2\right) + x_{c_i}\right)\left(R_{twmax} + r + y_1 - y_2\right) \tag{124}$$

$$\begin{aligned} c_4\left(x_{c_i}\right) = {} & 12x_1^2 - 4x_2^2 + 8x_1\left(x_2 - x_{c_i}\right) + 8x_2 x_{c_i} - 3x_{c_i}^2 \\ & + 4y_1\left(-2\left(R_{twmax} + r\right) + 3y_1\right) + 8\left(R_{twmax} + r + y_1\right)y_2 \\ & - 4y_2^2 + 16\left(R_{twmax} + r\right)\left(-x_1 \cos\varphi_o + y_1 \sin\varphi_o\right) \end{aligned} \tag{125}$$

$$\begin{aligned} c_3\left(x_{c_i}\right) = {} & -8\Big(\left(x_1 - x_2 + x_{c_i}\right)\left(R_{twmax} + r + y_1 - y_2\right) \\ & + 2\left(R_{twmax} + r\right)\left(y_1 \cos\varphi_o + x_1 \sin\varphi_o\right)\Big) \end{aligned} \tag{126}$$

$$c_2\left(x_{c_i}\right) = \left(-4x_1 + 4x_2 - 3x_{c_i}\right)x_{c_i} - 4\left(y_1 - y_2\right)\left(2\left(R_{twmax} + r\right) + y_1 - y_2\right) \tag{127}$$

$$c_1\left(x_{c_i}\right) = -4x_{c_i}\left(R_{twmax} + r + y_1 - y_2\right) \tag{128}$$

$$c_0\left(x_{c_i}\right) = -x_{c_i}^2 \tag{129}$$

$$\begin{aligned} f_i\left(\Theta, x_{c_i}\right) = {} & c_6\left(x_{c_i}\right)\Theta^6 + c_5\left(x_{c_i}\right)\Theta^5 + c_4\left(x_{c_i}\right)\Theta^4 + c_3\left(x_{c_i}\right)\Theta^3 \\ & + c_2\left(x_{c_i}\right)\Theta^2 + c_1\left(x_{c_i}\right)\Theta + c_0\left(x_{c_i}\right) \\ \equiv {} & 0 \end{aligned} \tag{130}$$

$$f_r\left(\Theta, x_{c_r}\right) = \left(2\left(x_1 - x_2\right) - x_{c_r}\right)\Theta^2 + 2\left(y_2 - y_1\right)\Theta - x_{c_r} \equiv 0 \tag{131}$$

$$\Theta\left(x_{c_r}\right) = \frac{y_1 - y_2}{2\left(x_1 - x_2\right) - x_{c_r}} \pm \frac{\sqrt{2\left(\left(x_1 - x_2\right)x_{c_r} - y_1 y_2\right) - x_{c_r}^2 + y_1^2 + y_2^2}}{2\left(x_1 - x_2\right) - x_{c_r}} \tag{132}$$

$$\theta\left(x_c\right) = 2\tan^{-1}\Theta\left(x_c\right) \tag{133}$$

Similarly to the Taylor series expansion, the procedures for determining the roots of Equations (130) and (131) follow the same approach (using matching methods and/or a graphical analysis). However, and to note, solving Equations (117) and (118) from the series expansion directly provides the cam rotation solution(s), while solving for the cam rotation using Equations (130) and (131) requires the additional use of Equation (133).

The potential benefit of using this method over the Taylor series is that it provides an exact, rather than approximate, cam rotation solution. This may be necessary from a research & development perspective when designing devices utilizing this theory as deviations from the theoretically exact cam rotation and corresponding clamping action may lead to undesirable contact force differences between the three grippers which present various functionality implications regarding real-world product designs. Furthermore, and worth considering, manufacturing will induce deviations from the theoretical cam contour due to machining capabilities and associated tolerances. Therefore, having a theoretically exact derivation for the cam rotation prior to manufacturing may be imperative to the desired output function of the accompanying physical product design with its corresponding manufacturing deviations from the theoretical exact design.

3.2.4. Related Other: Applied Unified Resultant Amplitude Method (URAM)

The various methods presented in the previous sections involving backward kinematic cam rotation equations are useful for creating the cam contour solution over an infinite domain. However, and for the design case, a finite range of the cam rotation must be specified in connection with the minimum and maximum workpiece diameters. Therefore, and considering generalization due to potential issues that may arise with sign changes occurring with trigonometric functions, a simulated unified resultant amplitude method for opposite wave summation has been developed [46] and will be utilized for obtaining the maximum cam rotation.

In connection, the maximum cam path coordinates can be determined in accordance with the maximum cam rotation by setting the minimum of Equation (14) for $y_4(\theta)$ to an equation comprising known specified analysis variables as shown through Equation (134). Consequently, a system of equations is developed and rearranged in the form of a summation wave, as shown through Equation (135), due to its connection with URAM theory.

$$R_{wmin} + r = y_4(\theta_{max}) \tag{134}$$

$$-2L_1x_1\cos(\eta-\theta_{max}) - 2L_1y_1\sin(\eta-\theta_{max}) = -L_1^2 - L_3^2 + (R_{wmin}+r)^2 \tag{135}$$

When applying URAM theory, various resultant wave parameters, including the cosine and sine amplitudes as well as the known wave summation number, are extracted from Equation (135) in the following manner.

$$a = -2L_1x_1 \tag{136}$$

$$b = -2L_1y_1 \tag{137}$$

$$c = -L_1^2 - L_3^2 + (R_{wmin}+r)^2 \tag{138}$$

Therefore, the wave summation equation for the maximum cam rotation is:

$$a\cos(\eta-\theta_{max}) + b\sin(\eta-\theta_{max}) = c \tag{139}$$

Based on the sense of a and b in relation to the triangle formations shown in [46], the quadrant number for the theoretical wave summation specific to this generalized arrangement will always be:

$$q = 3 \tag{140}$$

Accordingly, the combination-wave fluctuations arising from an analysis of polar waves are:

$$\hat{R} = \prod_{m=1}^{q} e^{i(m-1)\pi} = (-1)^{\mathrm{Floor}\left(\frac{q}{2}\right)} \Rightarrow -1 \tag{141}$$

$$\hat{\varnothing} = -e^{i(q-1)\pi} = -\cos\pi(q-1) - i\sin\pi(q-1) \Rightarrow -1 \tag{142}$$

Additionally, the associated resultant amplitude and phase angle parameters are:

$$R = \sqrt{a^2 + b^2} \Rightarrow 2L_1L_3 \tag{143}$$

$$\varnothing = \tan^{-1}\left|\frac{b}{a}\right| \Rightarrow \beta \tag{144}$$

Furthermore, the unified wave that corresponds to Equation (139) is:

$$\begin{gathered}\left[\hat{R}R\cos\left(\left(\eta - \theta_{max}\right) + \hat{\varnothing}\varnothing\right) = c\right] \Rightarrow \\ 2L_1L_3\cos\left(\beta - \eta + \theta_{max}\right) = -L_1^2 - L_3^2 + \left(r + R_{wmin}\right)^2\end{gathered} \tag{145}$$

Assuming the positive-domain condition along with a bounded limit of $0^\circ \le \theta \le 90^\circ$ due to practical application (requiring that $m = 0$), the maximum cam rotation equation is:

$$\begin{aligned}\theta_{max} &= \eta - \left(\cos^{-1}\frac{c}{\hat{R}R} - \hat{\varnothing}\varnothing - m\pi\right) \\ &\Rightarrow \eta - \beta - \cos^{-1}\frac{L_1^2 + L_3^2 - \left(r + R_{wmin}\right)^2}{2L_1L_3}\end{aligned} \tag{146}$$

In summary, backward kinematic cam rotation equations including the maximum cam rotation have been derived. Subsequently, a conversion of the parametric inverse/regular wedge cam equations into rectangular form will follow.

3.3. Converting the Parametric Wedge Cam Path into Rectangular Form

3.3.1. Method 1: Approximate Cam Contour Equations in Rectangular Form

Although the backward kinematic cam rotation equations involved the use of transformation equations, the parametric cam contour equations from any one of the three different methods can be converted into rectangular form. With the use of $\theta(x_c)$ derived by approximation, the parametric equation $y_c(\theta)$ can be converted into $y_c(x_c)$ within the local x' - y' Cartesian reference frame starting at point D and rotating to point D_2 for the inverse wedge cam (or translating to point D_1 for the regular wedge cam) through to the full cam rotation range as shown within the previous figures. However, and important to note, inaccuracies from the Taylor series are induced into the rectangular form of the cam contour equation. While this will most likely be undesirable, the use of higher order terms (as previously provided) may improve the accuracy of the cam profile to within an acceptable amount of error.

3.3.2. Method 2: Exact Cam Contour Equations in Rectangular Form

For eliminating inaccuracies involved within the Taylor series, the trigonometric substitution & transformation method for the equation of $\theta(x_c)$ can be used in conjunction with any one of the three parametric equation methods to obtain the rectangular form conversion of the cam contour equation. Additionally, the maximum cam rotation equation can be used to terminate the domain of both approximate and exact rectangular forms of the parametric cam contour equations.

3.3.3. Method 3: The Nonlinear Second Order Nonhomogeneous Instantaneous Constant Radius of Curvature Ordinary Differential Equation

To restate, the Taylor series as well as the trigonometric substitution & transformation method are used for converting the various parametric cam contour equations into approximate and exact rectangular forms respectively. Nevertheless, instead of converting the parametric cam contour equations into rectangular form by using the parametric cam contour equations in conjunction with the angle isolation approach, the radius of curvature ODE provided in Appendix A can be used to define the cam contour in rectangular form as a replacement for the parametric equations (although it still requires the angle solution). In connection with the ODE solution, the radius of curvature $r_{rc}\left(x_c\right)$ along with the associated variable initial conditions $k_1\left(x_c\right)$ and $k_2\left(x_c\right)$ of the cam contour are as follows.

$$r_{rc}\left(x_c\right)=\frac{\left(1+\left(\dfrac{y_c'\left(\theta\left(x_c\right)\right)}{x_c'\left(\theta\left(x_c\right)\right)}\right)^2\right)^{3/2}}{\left|\dfrac{y_c''\left(\theta\left(x_c\right)\right)}{\left(x_c'\left(\theta\left(x_c\right)\right)\right)^2}+\dfrac{y_c'\left(\theta\left(x_c\right)\right)}{x_c''\left(\theta\left(x_c\right)\right)}\right|} \tag{147}$$

$$k_1\left(x_c\right)=y_c\left(x_c\left(\theta\right)\right)\Rightarrow y_c\left(\theta\left(x_c\right)\right) \tag{148}$$

$$k_2\left(x_c\right)=y_c'\left(x_c\right)\Rightarrow \frac{y_c'\left(\theta\left(x_c\right)\right)}{x_c'\left(\theta\left(x_c\right)\right)} \tag{149}$$

Regarding this generalized ODE solution, any one of the solutions can be chosen for producing the same cam contour equation. However, only one of the solutions provides the appropriate sense for the first and second spatial derivatives of the cam path over the horizontal cam path component. Additionally, the positive sign choice for $c_1\left(x_c\right)$ is required for satisfying the direction of the associated derivatives. Therefore, the final differential equation solution involving the radius of curvature for the cam contours of both cam types is given by Equation (152).

$$c_1\left(x_c\right)=\frac{x_c}{r_{rc}\left(x_c\right)}+\frac{k_2^2\left(x_c\right)r_{rc}^2\left(x_c\right)}{\sqrt{k_2^2\left(x_c\right)\left(1+k_2^2\left(x_c\right)\right)r_{rc}^4\left(x_c\right)}} \tag{150}$$

$$c_2\left(x_c\right)=k_1\left(x_c\right)-\sqrt{r_{rc}^2\left(x_c\right)-x_c^2+2r_{rc}\left(x_c\right)c_1\left(x_c\right)x_c-r_{rc}^2\left(x_c\right)c_1^2\left(x_c\right)} \tag{151}$$

$$y\left(x_c\right)=\sqrt{r_{rc}^2\left(x_c\right)-x_c^2+2r_{rc}\left(x_c\right)c_1\left(x_c\right)x_c-r_{rc}^2\left(x_c\right)c_1^2\left(x_c\right)}+c_2\left(x_c\right) \tag{152}$$

Although Equation (152) for the cam contour solution(s) appears to be rather simple and consolidated, it is more complex than the parametric cam contour solution when expanded with associated derivatives and combined with the backward kinematic cam rotation equations. Nevertheless, one may find use for this radius of curvature ODE approach as a matter of choice. Additionally, it can be used as a means of validating the manner in which variable initial conditions are prescribed within the ODE theory through expecting the results to be identical to both the original approximation and exact methods respectively. Moreover, the differential equation itself can be validated through a consideration of the ODE solution in conjunction with its first and second derivatives. The combination described must be used rather than the ODE solution and its first derivative alone due to the nature in which the instantaneous constant variables $c_1(x_c)$ and $c_2(x_c)$ are determined.

3.3.4. Related Other: Normalization of the Wedge Cam Contour Equations

With the parametric and rectangular forms of the cam profile being established, normalization of the cam path equations will follow. In general, normalizing an equation means to create a unit vector. Specific to the self-centering wedge cam path, creating a unit vector for the cam profile will be based on the premise of changing the independent variable x_c (a one-dimensional vector) by dividing it with the maximum value of x_c for creating a ratio ς that maximizes at unity. Therefore, and regarding the resulting Equation (153), the original independent variable x_c is equivalent to $x_{cmax}\varsigma$.

$$\varsigma(\theta) = \frac{x_c(\theta)}{x_c(\theta_{max})} \tag{153}$$

Furthermore, parametric normalization can be achieved through a parametric plot of $y_c(\theta)$ versus $\varsigma(\theta)$. Additionally, rectangular forms of the cam contour can be normalized by substituting $x_{cmax}\varsigma$ for x_c thereby changing the independent variable to the normalization parameter spanning ratio values from zero to unity.

From a design context, having the normalized cam contour may be helpful for comparing one curve versus another within the analysis process. In connection, a potential application may involve design optimization for minimizing accelerations for various practical engineering reasons.

To note, and up to this point, a thorough presentation of the theoretical development for parametric cam contour equations, their associated spatial derivatives, backward kinematic cam rotation equations, as well as various rectangular form conversion methods have been provided. In the following, a generalized static equilibrium analysis of the mechanism will be formulated along with dynamics for providing a more holistic systems engineering framework regarding the self-centering wedge cam theory presented herein.

3.4. Static Equilibrium Equations

3.4.1. Driven Kinematic and Given Force Parameters

In order for equilibrium of the self-centering mechanism to be achieved, free-body diagrams of the workpiece, both rotational grippers, and the translational gripper are provided as shown in Figure 4 below. The static analyses presented, involving the determination of clamping, normal, and reaction forces, are useful from a machine design, application engineering, and robust design optimization context.

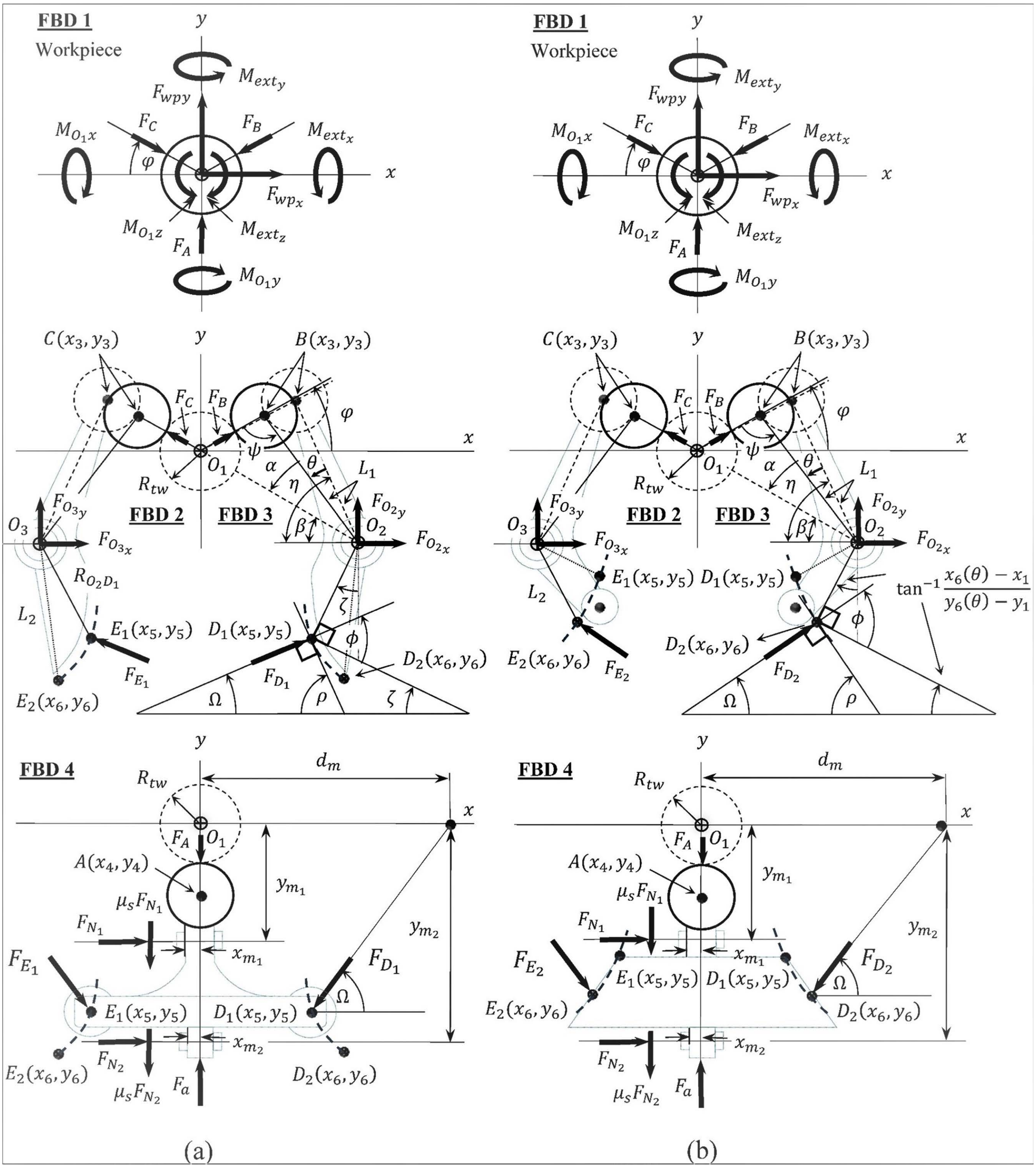

Figure 4. Free-body diagrams for force transmission (a) ınverse wedge cam, (b) regular wedge cam.

For generalization purposes, external reaction forces and external moments are included on the free-body diagram of the workpiece. These reaction forces take into account the weight of the workpiece, any external loadings along with their associated angles of approach, and the angle of tilt of the mechanism with respect to the global horizontal axis. Details regarding the equations for these reactions are left aside for the application engineer due to the numerous scenarios that might be encountered in practical reality.

As an aid to the application engineer, the problem will generally be indeterminate to the second degree and, therefore, the use of compatibility equations for the workpiece in the x - z and y - z planes can be considered through superposition to solve for the associated reaction forces and moments. Alternatively, the use of standard force and moment tables or general FEA techniques may be utilized when solving for the generalized reaction forces and moments denoted within the theory. Note that the manner in which moment reactions are transferred to the mechanism are left up to the application engineer. Additionally, the forces F_{wpx} and F_{wpy} in this theory are taken as the opposite sign of what is obtained by the application engineer.

Prior to static equilibrium analysis, the kinematic aspects shown in **Figure 4** are derived in the following way.

The required angles are:

$$\alpha(\theta) = \eta - \beta - \theta \tag{154}$$

$$\psi(\theta) = \pi - \left(\varphi(\theta) + \beta + \alpha(\theta)\right) \tag{155}$$

Additionally, the cam contour slope for both cam types is:

$$m_c(x_c) = \frac{\mathrm{d}y_c(x_c)}{\mathrm{d}x_c} \Rightarrow \frac{\mathrm{d}y_c(\theta(x_c))}{\mathrm{d}\theta(x_c)} \div \frac{\mathrm{d}x_c(\theta(x_c))}{\mathrm{d}\theta(x_c)} \tag{156}$$

In connection, the tangential and normal cam path angles for each cam type are:

$$\rho_i(\theta) = \left|\tan^{-1} m_c(\theta)\right| - \theta \tag{157}$$

$$\rho_r(\theta) = \left|\tan^{-1} m_c(\theta)\right| \tag{158}$$

$$\Omega(\theta) = \frac{\pi}{2} - \rho(\theta) \tag{159}$$

Therefore, the pressure angles for each cam are:

$$\phi_i(\theta) = \left|\Omega(\theta) - \zeta(\theta)\right| \tag{160}$$

$$\phi_r(\theta) = \left|\Omega(\theta) - \tan^{-1}\frac{x_6(\theta) - x_1}{y_6(\theta) - y_1}\right| \tag{161}$$

Lastly, the moment arms pertaining to the loop closure and force transmissibility regarding the normal cam contour forces are:

$$L_{m_i}(\theta) = \vec{R}_{O_2 D_1}(\theta) \tag{162}$$

$$L_{m_r}(\theta) = \vec{R}_{O_2 D_2}(\theta) \tag{163}$$

$$d_m(\theta) = \frac{L_m(\theta)\cos\phi(\theta)}{\sin\Omega(\theta)} + y_1(\theta)\cot\Omega(\theta) + x_1 \tag{164}$$

3.4.2. Equilibrium Equation Development

Within the static equilibrium equation development for the workpiece as previously shown in **Figure 4**—FBD 1, the positive sense of all external reaction forces is assumed. To note, there are five equilibrium equations for FBD 1 along with a total of six unknown variables.

$$\left[\Sigma F_{x_1}(\theta)=0\right]+\rightarrow; F_C(\theta)\cos\varphi(\theta)-F_B(\theta)\cos\varphi(\theta)+F_{wp_x}=0 \quad (165)$$

$$\left[\Sigma F_{y_1}(\theta)=0\right]+\uparrow; F_A(\theta)-F_B(\theta)\sin\varphi(\theta)-F_C(\theta)\sin\varphi(\theta)+F_{wp_y}=0 \quad (166)$$

$$\left[\Sigma M_{O_1x_1}(\theta)=0\right]+\circlearrowleft; M_{ext_x}-M_{O_1x}=0 \quad (167)$$

$$\left[\Sigma M_{O_1y_1}(\theta)=0\right]+\circlearrowleft; M_{ext_y}-M_{O_1y}=0 \quad (168)$$

$$\left[\Sigma M_{O_1z_1}(\theta)=0\right]+\circlearrowleft; M_{ext_z}-M_{O_1z}=0 \quad (169)$$

Additionally, the three equilibrium equations for FBD 2 pertaining to the rotational gripper on the left side yields three extra unknowns.

$$\left[\Sigma F_{x_2}(\theta)=0\right]+\rightarrow; F_{O_2x}(\theta)+F_B(\theta)\cos\varphi(\theta)+F_{D_{1,2}}(\theta)\cos\Omega(\theta)=0 \quad (170)$$

$$\left[\Sigma F_{y_2}(\theta)=0\right]+\uparrow; F_{O_2y}(\theta)+F_B(\theta)\sin\varphi(\theta)+F_{D_{1,2}}(\theta)\sin\Omega(\theta)=0 \quad (171)$$

$$\left[\Sigma M_{O_{22}}(\theta)=0\right]+\circlearrowleft; L_m(\theta)\left(F_{D_{1,2}}(\theta)\cos\phi(\theta)\right)-L_1\left(F_B(\theta)\sin\psi(\theta)\right)=0 \quad (172)$$

Similarly, the three equilibrium equations for FBD 3 pertaining to the rotational gripper on the right side yields three extra unknowns.

$$\left[\Sigma F_{x_3}(\theta)=0\right]+\rightarrow; F_{O_{3_x}}(\theta)-F_C(\theta)\cos\varphi(\theta)-F_{E_{1,2}}(\theta)\cos\Omega(\theta)=0 \quad (173)$$

$$\left[\Sigma F_{y_3}(\theta)=0\right]+\uparrow; F_{O_{3_y}}(\theta)+F_C(\theta)\sin\varphi(\theta)+F_{E_{1,2}}(\theta)\sin\Omega(\theta)=0 \quad (174)$$

$$\left[\Sigma M_{O_3}(\theta)=0\right]+\circlearrowleft; L_1\left(F_C(\theta)\sin\psi(\theta)\right)-L_m(\theta)\left(F_{E_{1,2}}(\theta)\cos\phi(\theta)\right)=0 \quad (175)$$

Finally, the three equilibrium equations for FBD 4 regarding the translational gripper yields two extra unknowns.

$$\begin{aligned}&\left[\Sigma F_{x_4}(\theta)=0\right]+\rightarrow; F_{E_{1,2}}(\theta)\cos\Omega(\theta)-F_{D_{1,2}}(\theta)\cos\Omega(\theta)\\&+F_{N_1}(\theta)+F_{N_2}(\theta)=0\end{aligned} \quad (176)$$

$$\begin{aligned}&\left[\Sigma F_{y_4}(\theta)=0\right]+\uparrow; F_a-F_A(\theta)-F_{D_{1,2}}(\theta)\sin\Omega(\theta)-F_{E_{1,2}}(\theta)\sin\Omega(\theta)\\&-\mu_s F_{N_1}(\theta)-\mu_s F_{N_2}(\theta)=0\end{aligned} \quad (177)$$

$$\begin{aligned}&\left[\Sigma M_{O_{14}}(\theta)=0\right]+\circlearrowleft; F_{N_1}(\theta)y_{m_1}+F_{N_1}(\theta)\mu_s x_{m_1}+F_{N_2}(\theta)y_{m_2}\\&+F_{N_2}(\theta)\mu_s x_{m_2}+F_{E_{1,2}}(\theta)\sin\Omega(\theta)d_m(\theta)\\&-F_{D_{1,2}}(\theta)\sin\Omega(\theta)d_m(\theta)=0\end{aligned} \quad (178)$$

Therefore, a total of 14 equations and 14 unknowns have been accounted for with the assumption that the reactions at the workpiece are given and/or calculated through other methods as previously described.

3.4.3. Static Force Equations in Terms of Kinematics and Given Force Parameters

Through a systematic resolution of the unknown variables, the contact force that the translational gripper exerts on the workpiece is:

$$\begin{aligned} F_A(\theta) = {} & \frac{1}{L_m(\theta)\cos\phi(\theta)\sin\varphi(\theta) + L_1\sin\psi(\theta)\sin\Omega(\theta)} \\ & \times\Big(F_a L_m(\theta)\cos\phi(\theta)\sin\varphi(\theta) \\ & - L_1\sin\psi(\theta)\Big(F_{wp_y}\sin\Omega(\theta) + F_{wp_x}\mu_s\cos\Omega(\theta)\tan\varphi(\theta)\Big)\Big) \end{aligned} \tag{179}$$

In conjunction, the contact force on the workpiece due to the rotational gripper on the right side is:

$$\begin{aligned} F_B(\theta) = {} & \frac{1}{2\big(L_m(\theta)\cos\phi(\theta)\sin\varphi(\theta) + L_1\sin\psi(\theta)\sin\Omega(\theta)\big)} \\ & \times\Big(L_m(\theta)\cos\phi(\theta)\Big(F_a + F_{wp_y} + F_{wp_x}\tan\varphi(\theta)\Big) \\ & + F_{wp_x}L_1\sec\varphi(\theta)\sin\psi(\theta)\big(\sin\Omega(\theta) - \mu_s\cos\Omega(\theta)\big)\Big) \end{aligned} \tag{180}$$

Similarly, the contact force on the workpiece due to the rotational gripper on the left side is:

$$\begin{aligned} F_C(\theta) = {} & \frac{1}{2\big(L_m(\theta)\cos\phi(\theta)\sin\varphi(\theta) + L_1\sin\psi(\theta)\sin\Omega(\theta)\big)} \\ & \times\Big(L_m(\theta)\cos\phi(\theta)\Big(F_{wp_y} + F_a - F_{wp_x}\tan\varphi(\theta)\Big) \\ & - F_{wp_x}L_1\sec\varphi(\theta)\sin\psi(\theta)\big(\mu_s\cos\Omega(\theta) + \sin\Omega(\theta)\big)\Big) \end{aligned} \tag{181}$$

Additionally, the reaction moments on the workpiece located at the mechanism x - y plane are $M_{O1x1} = M_{extx}$, $M_{O1y1} = M_{exty}$, and $M_{O1z1} = M_{extz}$.

Moving further, the normal force reactions regarding the cam roller follower on the right side of the translational gripper are:

$$\begin{aligned} F_{D_{1,2}}(\theta) = {} & \frac{1}{2L_m(\theta)\big(L_m(\theta)\sin\varphi(\theta) + L_1\sec\phi(\theta)\sin\psi(\theta)\sin\Omega(\theta)\big)} \\ & \times\Big(F_{wp_x}L_m(\theta)\tan\varphi(\theta) + \Big(F_a + F_{wp_y}\Big)L_m(\theta) \\ & + F_{wp_x}L_1\sec\phi(\theta)\sec\varphi(\theta)\sin\psi(\theta)\big(\sin\Omega(\theta) \\ & - \mu_s\cos\Omega(\theta)\big)\Big)L_1\sec\phi(\theta)\sin\psi(\theta) \end{aligned} \tag{182}$$

Similarly, the normal force reactions regarding the cam roller follower on the left side of the translational gripper are:

$$\begin{aligned} F_{E_{1,2}}(\theta) = {} & \frac{-1}{2L_m(\theta)\big(L_m(\theta)\sin\varphi(\theta) + L_1\sec\phi(\theta)\sin\psi(\theta)\sin\Omega(\theta)\big)} \\ & \times\Big(F_{wp_x}L_m(\theta)\tan\varphi(\theta) - \Big(F_a + F_{wp_y}\Big)L_m(\theta) \\ & + F_{wp_x}L_1\sec\phi(\theta)\sec\varphi(\theta)\sin\psi(\theta)\big(\mu_s\cos\Omega(\theta) \\ & + \sin\Omega(\theta)\big)\Big)L_1\sec\phi(\theta)\sin\psi(\theta) \end{aligned} \tag{183}$$

Also, the normal (friction related) force for the upper end of the translational gripper is:

$$F_{N_1}(\theta) = -\frac{1}{L_m(\theta)\left(y_{m_1} - y_{m_2} + \left(x_{m_1} - x_{m_2}\right)\mu_s\right)}\Big(\Big(\left(y_{m_2} + x_{m_2}\mu_s\right)\cos\Omega(\theta) - d_m(\theta)\sin\Omega(\theta)\Big)F_{wp_x}L_1\sec\phi(\theta)\sec\varphi(\theta)\sin\psi(\theta)\Big) \tag{184}$$

Similarly, the normal (friction related) force for the lower end of the translational gripper (at the actuator) is:

$$F_{N_2}(\theta) = \frac{1}{L_m(\theta)\left(y_{m_1} - y_{m_2} + \left(x_{m_1} - x_{m_2}\right)\mu_s\right)}\Big(\Big(\left(y_{m_1} + x_{m_1}\mu_s\right)\cos\Omega(\theta) - d_m(\theta)\sin\Omega(\theta)\Big)F_{wp_x}L_1\sec\phi(\theta)\sec\varphi(\theta)\sin\psi(\theta)\Big) \tag{185}$$

Finally, the reaction forces at the pivot for the rotational gripper on the right side are:

$$\begin{aligned} F_{O_2x}(\theta) = &-\frac{1}{2L_m(\theta)\left(L_m(\theta)\sin\varphi(\theta) + L_1\sec\phi(\theta)\sin\psi(\theta)\sin\Omega(\theta)\right)} \\ &\times\cos\varphi(\theta)\left(L_m(\theta) + L_1\cos\Omega(\theta)\sec\phi(\theta)\sec\varphi(\theta)\sin\psi(\theta)\right) \\ &\Big(\left(F_a + F_{wp_y}\right)L_m(\theta) + F_{wp_x}L_1\sec\phi(\theta)\sec\varphi(\theta)\sin\psi(\theta) \\ &\left(\sin\Omega(\theta) - \mu_s\cos\Omega(\theta)\right) + F_{wp_x}L_m(\theta)\tan\varphi(\theta)\Big) \end{aligned} \tag{186}$$

$$\begin{aligned} F_{O_2y}(\theta) = &-\frac{1}{2L_m(\theta)}\Big(\left(F_a + F_{wp_y}\right)L_m(\theta) + F_{wp_x}L_m(\theta)\tan\varphi(\theta) \\ &+ F_{wp_x}L_1\sec\phi(\theta)\sec\varphi(\theta)\sin\psi(\theta)\left(\sin\Omega(\theta) - \mu_s\cos\Omega(\theta)\right)\Big) \end{aligned} \tag{187}$$

Similarly, the reaction forces at the pivot for the rotational gripper on the left side are:

$$\begin{aligned} F_{O_3x}(\theta) = &-\frac{1}{2L_m(\theta)\left(L_m(\theta)\sin\varphi(\theta) + L_1\sec\phi(\theta)\sin\psi(\theta)\sin\Omega(\theta)\right)} \\ &\times\cos\varphi(\theta)\left(L_m(\theta) + L_1\cos\Omega(\theta)\sec\phi(\theta)\sec\varphi(\theta)\sin\psi(\theta)\right) \\ &\times\Big(\left(F_a + F_{wp_y}\right)\left(-L_m(\theta)\right) + F_{wp_x}L_1\sec\phi(\theta)\sec\varphi(\theta)\sin\psi(\theta) \\ &\times\left(\sin\Omega(\theta) + \mu_s\cos\Omega(\theta)\right) + F_{wp_x}L_m(\theta)\tan\varphi(\theta)\Big) \end{aligned} \tag{188}$$

$$\begin{aligned} F_{O_3y}(\theta) = &\frac{1}{2L_m(\theta)}\Big(F_{wp_x}L_m(\theta)\tan\varphi(\theta) - \left(F_a + F_{wp_y}\right)L_m(\theta) \\ &+ F_{wp_x}L_1\sec\phi(\theta)\sec\varphi(\theta)\sin\psi(\theta)\left(\sin\Omega(\theta) + \mu_s\cos\Omega(\theta)\right)\Big) \end{aligned} \tag{189}$$

As shown, all force formulations are conveniently expressed only in terms of given externally applied loadings and geometrical parameters rather than in terms of other unknown forces. This is valuable as all forces can be theoretically defined rather than needing to use experimental or other similar approaches for resolving one or more of the unknown forces for determining the remaining unknown forces. Moreover, and from a machine design context, the contact forces may then be used in conjunction with Hertzian cylindrical contact stress or other related machine design formulas and/or FEA for determining contact stresses on the workpiece/grippers and related components as well as the cam paths/roller followers and their related components. Additionally, the reaction forces at the pivot points O_2 and O_3 may be used to calculate stresses on the gripper arms and housing at the pivot holes and related pins/bolts. These stresses in comparison to materials and their properties along with reasonable safety factors for the intended application may be used for properly designing and/or sizing these items.

3.5. Translational Gripper, Rotational Gripper, and Cam Dynamics Equations

3.5.1. Rectilinear Self-Centering Translational Gripper Dynamics

As an extension of the generalized static equilibrium analysis in conjunction with being useful from an engineering design, robotics & controls theory, as well as robust design optimization context, dynamic equations regarding the translational and rotational grippers in addition to the cam will be presented.

From a dynamic perspective, vertical movement of the translational gripper results in rotation of the side-arm grippers. Consequently, rectilinear dynamics arise in connection with angular and curvilinear dynamics of the rotational gripper and associated cam contour as provided by the general description within **Figure 5** below.

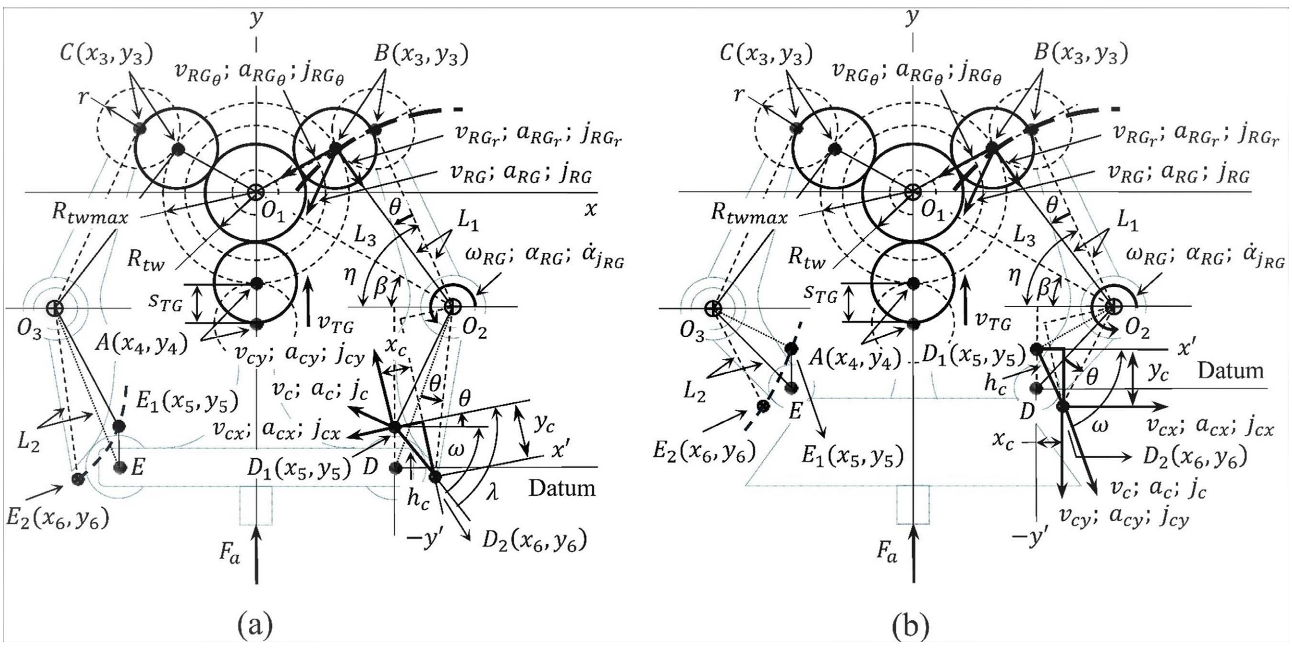

Figure 5. Dynamics diagram of the entire system (a) ınverse wedge cam, (b) regular wedge cam.

Rectilinear dynamics for the translational gripper will be considered through the constant power condition for practical purposes. More specifically, the constant power condition will be used for producing a linear displacement function coupled with a constant rectilinear velocity. As widely known, the constant power condition states that:

$$\text{power} = \frac{\text{force} \times \text{displacement}}{\text{time}}$$

Therefore, and with the force F_a (given), the power P_c (given), and the linear displacement function $s_{TG}(t)$ (travel from the datum in the positive y direction as shown in **Figure 5**), the displacement function can be isolated as a function of time.

$$s_{TG}(t) = \frac{P_c}{F_a} t \tag{190}$$

Additionally, the time derivative of the linear displacement function results in the rectilinear self-centering velocity as shown below.

$$v_{TG}(t) = \frac{P_c}{F_a} \tag{191}$$

Provided that the velocity is constant, as expected for constant power, the acceleration and jerk are zero. To follow, the associated rectilinear dynamics are extended into the development of angular dynamics for the rotational grippers.

3.5.2. Angular Rotational Gripper Dynamics

In consideration of angular dynamics, the angle of cam rotation is required to be a function of time. Therefore, the linear displacement function $s_{TG}(t)$ will be used in conjunction with $y_4(\theta)$ obtained from the basic trigonometric method as follows.

$$y_4(\theta) = (R_{twmax} + r) - s_{TG}(t) \tag{192}$$

To note, the associated value of time that corresponds to the angle of cam rotation is:

$$t(\theta) = \frac{F_a}{P_c}\left(R_{twmax} - R_{tw}(\theta)\right) \tag{193}$$

In connection with URAM theory [46], Equation (192) is converted into the following wave summation form.

$$\begin{aligned} &-2L_1 x_1 \cos(\eta - \theta) - 2L_1 y_1 \sin(\eta - \theta) \\ &= -L_1^2 - L_3^2 + \left(r + R_{twmax} - \frac{P_c}{F_a} t\right)^2 \end{aligned} \tag{194}$$

The cosine and sine amplitudes for Equation (194) are identical to Equations (136) and (137). However, the wave summation number is different than Equation (138) due to the varying time parameter for travel. Consequently, the wave summation number for Equation (194) is:

$$c_D(t) = -L_1^2 - L_3^2 + \left(r + R_{twmax} - \frac{P_c}{F_a} t\right)^2 \tag{195}$$

Due to the cosine and sine amplitudes being the same, the quadrant number of wave summation q, combination-wave fluctuations $\hat{R}$ and $\hat{\varnothing}$, and resultant amplitude parameters R and $\varnothing$ are identical to their respective equations regarding the determination of the maximum angle of cam rotation.

Therefore, the corresponding unified summation wave for Equation (194) is:

$$\left[\hat{R}R\cos\left(\left(\eta-\theta\right)+\hat{\varnothing}\varnothing\right)=c_D\left(t\right)\right]\Rightarrow$$
$$-2L_1L_3\cos\left(\beta-\eta+\theta\right)=-L_1^2-L_3^2+\left(r+R_{twmax}-\frac{P_c}{F_a}t\right)^2 \tag{196}$$

Consequently, and assuming the positive-domain condition along with a bounded limit of $0^\circ\le\theta\le90^\circ$ (requiring that $m=0$), the temporal-domain cam rotation equation is:

$$\theta\left(t\right)=\eta-\left(\cos^{-1}\frac{c_D\left(t\right)}{\hat{R}R}-\hat{\varnothing}\varnothing-m\pi\right)$$
$$=\eta-\beta-\cos^{-1}\frac{L_1^2+L_3^2-\left(r+R_{twmax}-\frac{P_c}{F_a}t\right)^2}{2L_1L_3} \tag{197}$$

Moving further, with having the temporal-domain cam rotation provided by Equation (197), successive time derivatives of the cam rotation are performed for obtaining the angular dynamics of the rotational gripper. Note that the derivatives are presented in condensed form utilizing Equation (143) for R, Equation (195) for $c_D\left(t\right)$, Equation (191) for $v_{TG}\left(t\right)$, and Equation (14) or (63) for $y_4\left(\theta\right)$. Also, note that Equation (197) is used for substitution into $y_4\left(\theta\right)$ for conversion of the cam rotation into temporal-domain form.

$$\omega_{RG}\left(t\right)=\dot{\theta}\left(t\right)\Rightarrow\frac{2v_{TG}\left(t\right)y_4\left(\theta\left(t\right)\right)}{\sqrt{R^2-c_D\left(t\right)^2}} \tag{198}$$

$$\alpha_{RG}\left(t\right)=\ddot{\theta}\left(t\right)=\dot{\omega}_{RG}\left(t\right)\Rightarrow-\frac{2v_{TG}\left(t\right)^2}{\sqrt{R^2-c_D\left(t\right)^2}}-\frac{4c_D\left(t\right)v_{TG}\left(t\right)^2y_4\left(\theta\left(t\right)\right)^2}{\left(R^2-c_D\left(t\right)^2\right)^{3/2}} \tag{199}$$

$$\dot{\alpha}_{j_{RG}}\left(t\right)=\dddot{\theta}\left(t\right)=\ddot{\omega}_{RG}\left(t\right)=\dot{\alpha}_{RG}\left(t\right)\Rightarrow$$
$$\frac{12c_D\left(t\right)v_{TG}\left(t\right)^3y_4\left(\theta\left(t\right)\right)}{\left(R^2-c_D\left(t\right)^2\right)^{3/2}}+\frac{24c_D\left(t\right)^2v_{TG}\left(t\right)^3y_4\left(\theta\left(t\right)\right)^3}{\left(R^2-c_D\left(t\right)^2\right)^{5/2}} \tag{200}$$
$$+\frac{8v_{TG}\left(t\right)^3y_4\left(\theta\left(t\right)\right)^3}{\left(R^2-c_D\left(t\right)^2\right)^{3/2}}$$

To follow, curvilinear dynamics of the rotational gripper with a consideration of generalized universal cylindrical motion equations will be presented.

3.5.3. Curvilinear Rotational Gripper Dynamics

In connection with curvilinear rotational dynamics, the position of the rotational gripper is determined by the arc length formula.

$$s_{RG}\left(t\right)=\theta\left(t\right)L_1 \tag{201}$$

Furthermore, the total velocity, acceleration, and jerk vectors having radial and transverse components are obtained from cylindrical motion equations as shown below.

$$v_{RG}(t)=\left[\dot{L}_1\boldsymbol{u}_r+L_1\omega_{RG}(t)\boldsymbol{u}_\theta\right]\Rightarrow\left[0\boldsymbol{u}_r+L_1\omega_{RG}(t)\boldsymbol{u}_\theta\right]\Rightarrow L_1\omega_{RG}(t) \tag{202}$$

$$\begin{gathered}a_{RG}(t)=\left[\left(\ddot{L}_1-L_1\omega_{RG}^2(t)\right)\boldsymbol{u}_r+\left(L_1\alpha_{RG}(t)+2\dot{L}_1\omega_{RG}(t)\right)\boldsymbol{u}_\theta\right]\Rightarrow\\ \left[-L_1\omega_{RG}^2(t)\boldsymbol{u}_r+L_1\alpha_{RG}(t)\boldsymbol{u}_\theta\right]\Rightarrow L_1\sqrt{\omega_{RG}^4(t)+\alpha_{RG}^2(t)}\end{gathered} \tag{203}$$

$$\begin{gathered}j_{RG}(t)=\left[\left(\dddot{L}_1-3L_1\omega_{RG}(t)\alpha_{RG}(t)-3\dot{L}_1\omega_{RG}^2(t)\right)\boldsymbol{u}_r\right.\\ \left.+\left(L_1\dot{\alpha}_{j_{RG}}(t)+3\dot{L}_1\omega_{RG}(t)+3\ddot{L}_1\omega_{RG}(t)-\dot{L}_1\omega_{RG}^3(t)\right)\boldsymbol{u}_\theta\right]\Rightarrow\\ \left[-3L_1\omega_{RG}(t)\alpha_{RG}(t)\boldsymbol{u}_r+L_1\dot{\alpha}_{j_{RG}}(t)\boldsymbol{u}_\theta\right]\Rightarrow L_1\sqrt{9\omega_{RG}^2(t)\alpha_{RG}^2(t)+\dot{\alpha}_{j_{RG}}^2(t)}\end{gathered} \tag{204}$$

The translational and rotational gripper dynamics provided may be useful regarding impact forces within an engineering design and design optimization/robust design optimization context. Additionally, the angular dynamics associated with the above curvilinear dynamics will be used to formulate the following cam dynamic equations.

3.5.4. Curvilinear Wedge Cam Contour Dynamics

For deriving cam dynamic equations, spatial derivatives and angular dynamics are used regarding the application of the chain rule for time differentiation of the parametric cam contour equation in terms of the cam rotation [38]. Spatial derivatives of the cam contour equation are given by Equations (91) through (102) for both cam types. In conjunction, the angular dynamics are given by Equations (198) through (200). To provide a holistic cam dynamic analysis, horizontal, vertical, and resultant components of motion regarding velocity, acceleration, and jerk are provided below.

The horizontal components of motion are:

$$v_{c_x}(t)=\frac{\mathrm{d}x_c(\theta(t))}{\mathrm{d}\theta(t)}\omega_{RG}(t) \tag{205}$$

$$a_{c_x}(t)=\frac{\mathrm{d}^2x_c(\theta(t))}{\mathrm{d}\theta(t)^2}\omega_{RG}^2(t)+\frac{\mathrm{d}x_c(\theta(t))}{\mathrm{d}\theta(t)}\alpha_{RG}(t) \tag{206}$$

$$\begin{gathered}j_{c_x}(t)=\frac{\mathrm{d}^3x_c(\theta(t))}{\mathrm{d}\theta(t)^3}\omega_{RG}^3(t)+3\frac{\mathrm{d}^2x_c(\theta(t))}{\mathrm{d}\theta(t)^2}\omega_{RG}(t)\alpha_{RG}(t)\\ +\frac{\mathrm{d}x_c(\theta(t))}{\mathrm{d}\theta(t)}\dot{\alpha}_{j_{RG}}(t)\end{gathered} \tag{207}$$

Furthermore, the vertical components of motion are:

$$v_{c_y}(t)=\frac{\mathrm{d}y_c(\theta(t))}{\mathrm{d}\theta(t)}\omega_{RG}(t) \tag{208}$$

$$a_{c_y}(t)=\frac{\mathrm{d}^2y_c(\theta(t))}{\mathrm{d}\theta(t)^2}\omega_{RG}^2(t)+\frac{\mathrm{d}y_c(\theta(t))}{\mathrm{d}\theta(t)}\alpha_{RG}(t) \tag{209}$$

$$j_{c_y}\left(t\right)=\frac{\mathrm{d}^3 y_c\left(\theta\left(t\right)\right)}{\mathrm{d}\theta\left(t\right)^3}\omega_{RG}^3\left(t\right)+3\frac{\mathrm{d}^2 y_c\left(\theta\left(t\right)\right)}{\mathrm{d}\theta\left(t\right)^2}\omega_{RG}\left(t\right)\alpha_{RG}\left(t\right)+\frac{\mathrm{d}y_c\left(\theta\left(t\right)\right)}{\mathrm{d}\theta\left(t\right)}\dot{\alpha}_{j_{RG}}\left(t\right) \tag{210}$$

Finally, the resultant of both horizontal and vertical components of motion regarding the cam path are:

$$v_c\left(t\right)=\sqrt{v_{c_x}^2\left(t\right)+v_{c_y}^2\left(t\right)} \tag{211}$$

$$a_c\left(t\right)=\sqrt{a_{c_x}^2\left(t\right)+a_{c_y}^2\left(t\right)} \tag{212}$$

$$j_c\left(t\right)=\sqrt{j_{c_x}^2\left(t\right)+j_{c_y}^2\left(t\right)} \tag{213}$$

In connection, and in terms of cylindrical motion equations, the resultant components of motion represent the total velocity, acceleration, and jerk (or magnitude of the specific radial and transverse components of self-centering motion).

In closing, Equations (205) through (213) for the curvilinear cam dynamic procedures provide a systematic method for determining the motions of the cam contour utilizing spatial and angular (constant power-based) dynamics. In relation to such, a consideration of the dynamic characteristics for these wedge cams may be useful in engineering design as well as design optimization/robust design optimization of the self-centering arrangement for minimizing certain motion aspects which may involve the cam contour shape in addition to clamping characteristics in terms of impact and vibration.

4. Results with Results Discussion

Regarding authentication of the generalized kinematic theory for achieving accurate self-centering clamping action, the kinematic layout and theoretical arrangement has been applied within the framework of self-centering inverse and regular wedge cam mechanism designs. The overall approach taken to validate the theoretical arrangement and the foundational mathematics involves development of the cam contours as well as the associated gripper paths and related self-centering functions from computer-generated configurations of the mechanism designs as previously shown in **Figure 1(a)** and **Figure 1(b)**. The expected results compared against actual results created from the self-centering function and associated layout validates the actual cam contour solutions and self-centering motion regarding the gripper paths in connection with variable theoretical workpiece diameters constructed from their three points of tangency.

Moving further, clarity in relation to other engineering methods involving the vector formulation and force analyses are self-evidently and respectively verified through loop-closure and equilibrium equations as well as computer-aided engineering (CAE) simulation. Moreover, verification of the dynamic analyses arises from a consideration of CAE motion simulation, average speed calculations, and centered finite-difference methods in addition to graphical considerations regarding calculus aspects in relation to concavity, critical points, abscissa intercepts, inflection points, and curvatures.

4.1. The Self-Centering Inverse and Regular Wedge Cam Mechanism Concept Design Based on Transformation Equations with Cam Path Validation

The validation procedures for the design configurations shown in Figure 1 are constructed from several specified/driving analysis variables including R_{wmax} = 4 in. (0.1016 m), R_{wmin} = 0.5 in. (0.0127 m), r = 2 in. (0.0508 m), C_{lrx} = 0.5 in. (0.0127 m), φ_o = 30˚, x_1 = 12.21 in. (0.3101 m), and y_1 = 11.14 in. (0.2829 m) for both design types along with x_2 = 15.38 in. (0.3907 m) and y_2 = 22.64 in. (0.5751 m) for the inverse wedge cam (and x_2 = 13.21 in. (0.3355 m) and y_2 = 18.29 in. (0.4646 m) for the regular wedge cam), for defining the self-centering geometry. In connection with the design specifications, the finite-domain cam profile and corresponding gripper paths (shown in Figure 6) are determined through transformation equations in conjunction with the angle of cam rotation varying from 0˚ to 18.06˚ (0.315 rad) in accordance with URAM theory. The resulting cam path equations shown in Figure 7 are used for producing the self-centering function(s) regarding the design layouts (at various cam rotation increments) as shown in Figure 8 below. For validation of the cam contour(s) in connection with the self-centering function(s), the design configurations shown provide an illustration for self-centering coordinates (φ, R_{RG}, and R_{TG} at various increments of the cam angle) obtained from transformation equations of the cam paths. Concluding from the parametrically driven computer-generated models, it is observed in Figure 8 below that the radial self-centering coordinate point

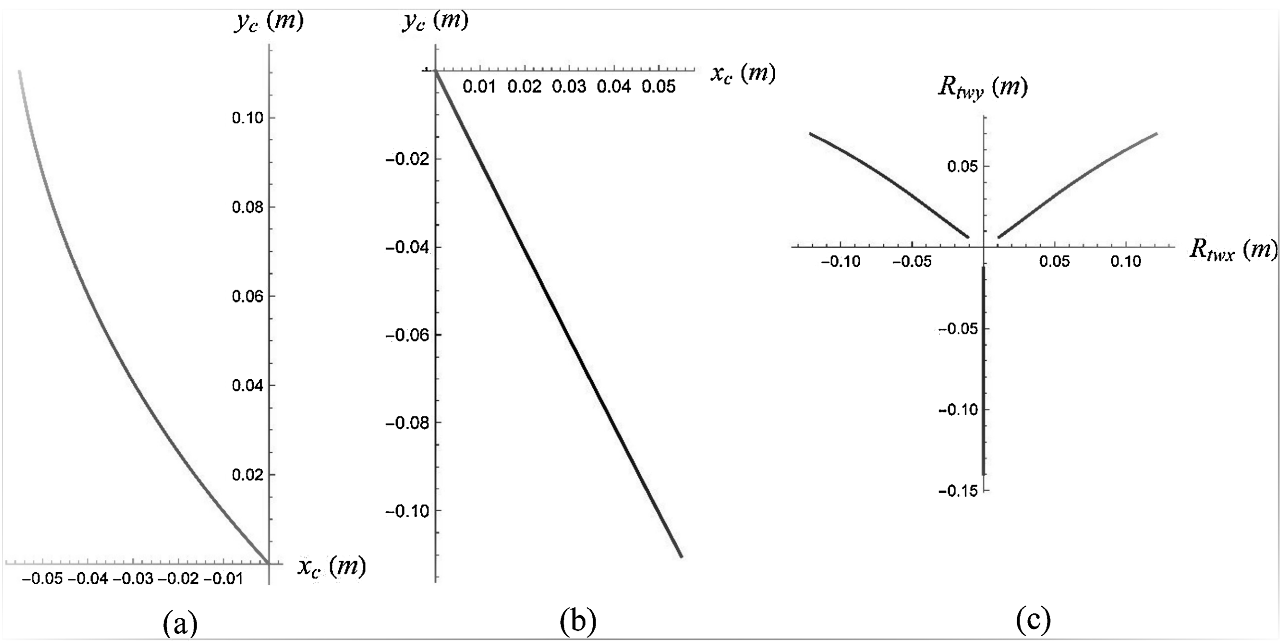

Figure 6. (a) Inverse cam contour, (b) regular cam contour, (c) gripper paths for both types.

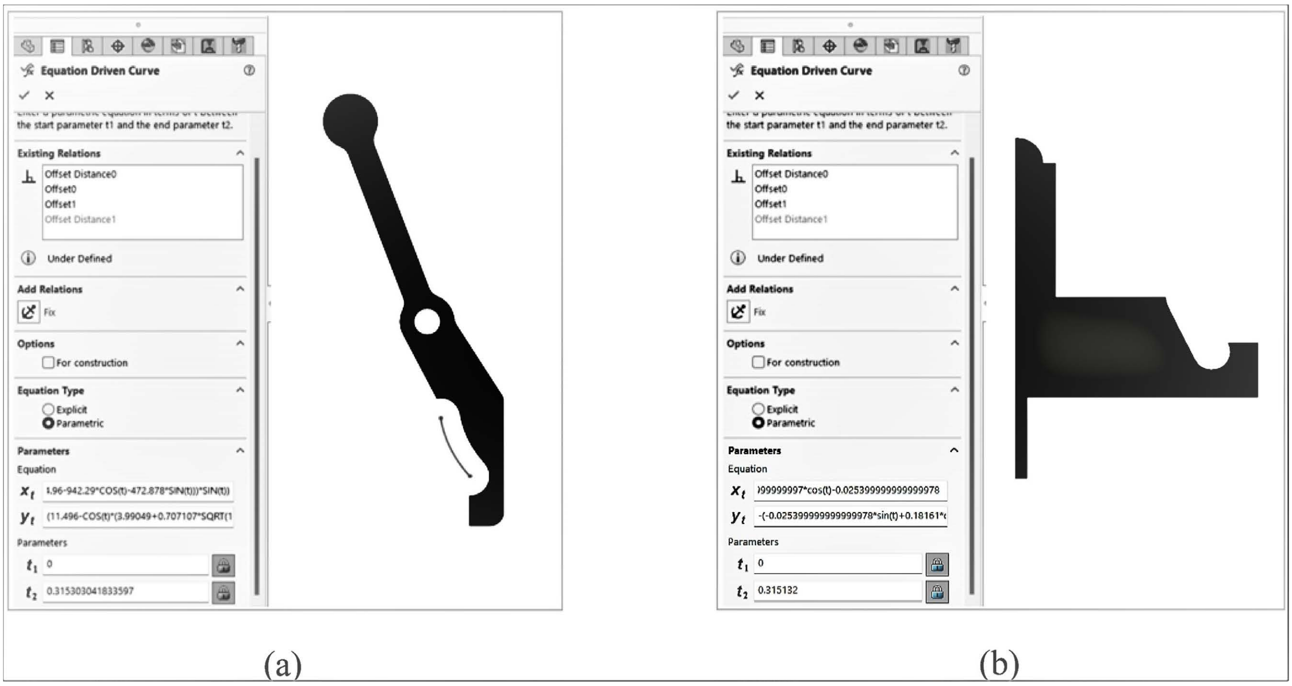

Figure 7. Wedge cam path creation (a) inverse wedge cam, (b) regular wedge cam.

magnitudes for the rotational grippers match the translational gripper magnitudes thereby indicating that the cam contour equations based on transformation equations along with their intended self-centering function are validated.

Additionally, expected values of self-centering coordinates are obtained through basic trigonometry and compared against actual self-centering coordinates obtained through analytical equations in terms of chosen and calculated angles of cam rotation when validating parametric and rectangular form equations of the cam contours in connection with the variable theoretical workpiece diameters regarding their points of tangency. In conjunction, the self-centering radii at the initial and maximum angles of cam rotation match their expected values of $R_{twmax} = 5.506$ in. (0.1398 m) determined from Equation (1) and $R_{wmin} = 0.5$ in. (0.0127 m) as previously given in addition to all expected values in between as can be reasonably extrapolated from Figure 8. For comparison of results, the actual cam profiles in parametric form determined through trigonometric, combined loop-closure with vector projection/resolution, and transformation equations are compared against the cam paths validated within the computer-aided environment indicating 0.0000% percent errors as shown in Table 1 below. For further validation of results, the actual cam profiles in rectangular form are determined through both transformation equations and the ODE solution using the Taylor series approach as well as the trigonometric substitution & transformation method in conjunction with the maximum cam rotation from URAM theory.

As shown in Table 2, the methods using the Taylor series produce maximum errors of 0.0001% for the inverse wedge cam (as well as 0.0000% for the regular wedge cam) regarding self-centering coordinates over the given design range.

While error is expected, it is negligible for the eleventh order series expansion in connection with these associated designs. Moreover, the methods comprising trigonometric substitution & transformation provide errors of 0.0000%. This is

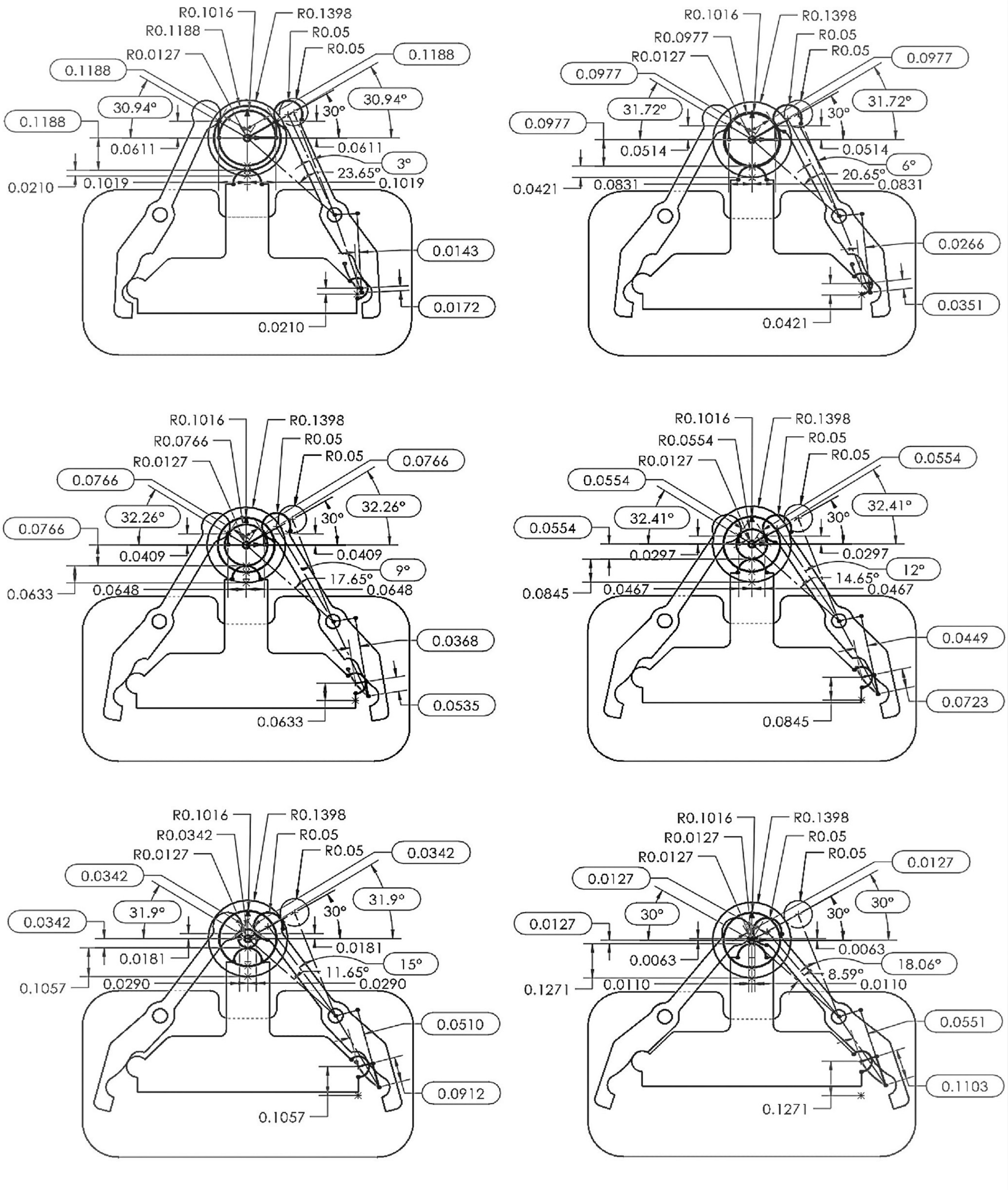

(a)

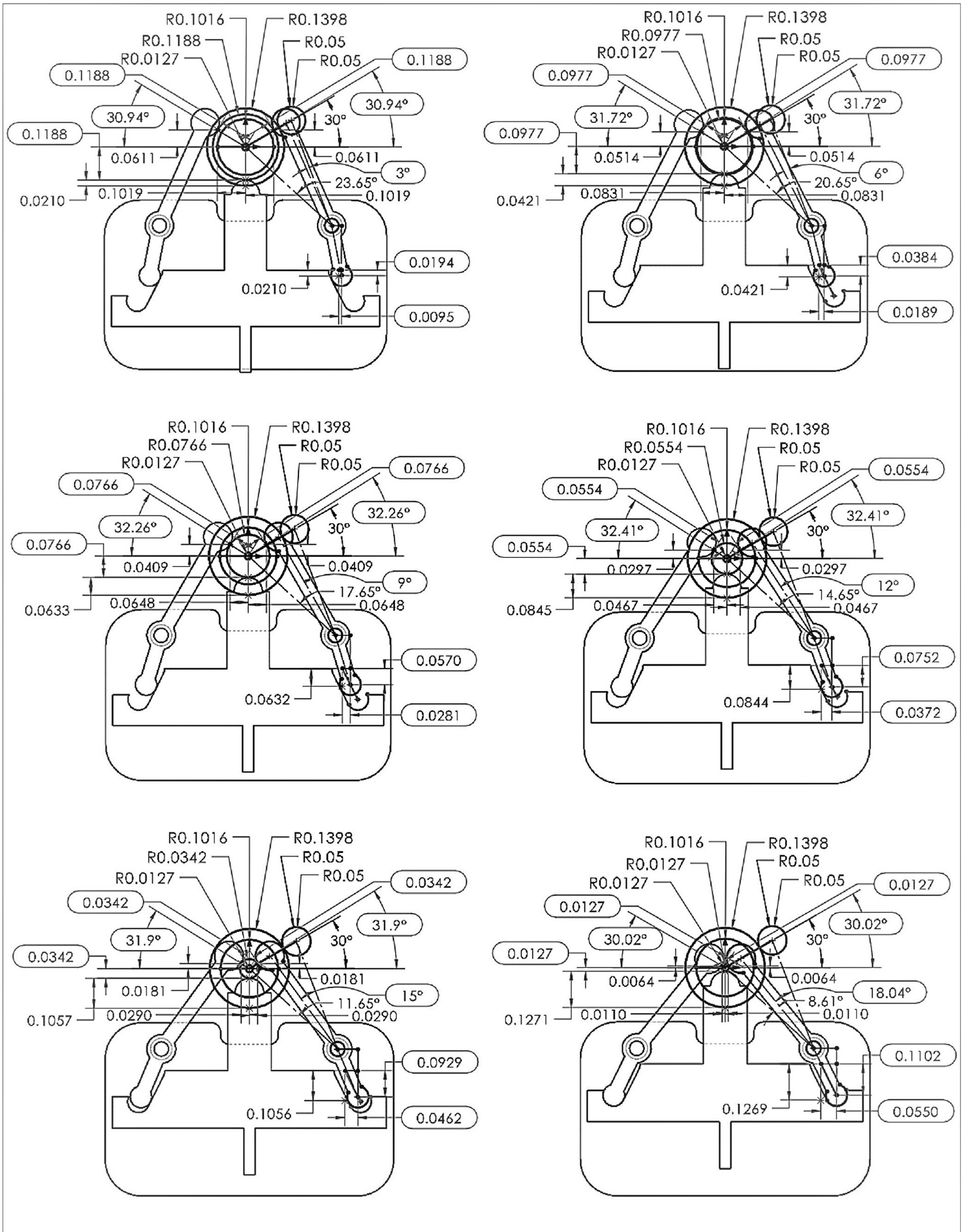

(b)

Figure 8. Computer-generated parametrically driven model of the self-centering wedge cams at various angle increments (a) inverse wedge cam, (b) regular wedge cam.

also expected since the theoretical basis of these methods are founded upon exact mathematical principles rather than using approximation methods. With the percent error being at or near 0.0000% for all approximate and exact methods, the cam contours, all three gripper paths, and therefore the corresponding self-centering functions are validated with a high degree of mathematical accuracy and precision. Furthermore, validation is self-evidently extended to the normalization

Table 1. Parametric cam contour and associated self-centering points validation (a) inverse wedge cam, (b) regular wedge cam.

(a)

Incr. (θ)	Expected Cam Path Points		Expected Self-Centering Points			Actual Cam Path Points with Percent Error				Actual Self-Centering Points with Percent Error					
Parametric Trigonometric Cam Path Equations															
θ (deg)	x_c (m)	y_c (m)	φ (deg)	R_{RG} (m)	R_{TG} (m)	x_c (m)	y_c (m)	E_{xc} (%)	E_{yc} (%)	φ (deg)	R_{RG} (m)	R_{TG} (m)	E_{φ} (%)	E_{RG} (%)	E_{TG} (%)
0	0.000	0.000	30.00	0.134	0.134	0.000	0.000	0.0000	0.0000	30.00	0.134	0.134	0.0000	0.0000	0.0000
3	0.014	0.017	30.94	0.119	0.119	0.014	0.017	0.0000	0.0000	30.94	0.119	0.119	0.0000	0.0000	0.0000
6	0.027	0.035	31.72	0.098	0.098	0.027	0.035	0.0000	0.0000	31.72	0.098	0.098	0.0000	0.0000	0.0000
9	0.037	0.054	32.26	0.077	0.077	0.037	0.054	0.0000	0.0000	32.26	0.077	0.077	0.0000	0.0000	0.0000
12	0.045	0.072	32.42	0.055	0.055	0.045	0.072	0.0000	0.0000	32.42	0.055	0.055	0.0000	0.0000	0.0000
15	0.051	0.091	31.90	0.034	0.034	0.051	0.091	0.0000	0.0000	31.90	0.034	0.034	0.0000	0.0000	0.0000
18.06	0.055	0.110	30.00	0.013	0.013	0.055	0.110	0.0000	0.0000	30.00	0.013	0.013	0.0000	0.0000	0.0000
Parametric Loop-Closure Cam Path Equations															
0	0.000	0.000	30.00	0.134	0.134	0.000	0.000	0.0000	0.0000	30.00	0.134	0.134	0.0000	0.0000	0.0000
3	0.014	0.017	30.94	0.119	0.119	0.014	0.017	0.0000	0.0000	30.94	0.119	0.119	0.0000	0.0000	0.0000
6	0.027	0.035	31.72	0.098	0.098	0.027	0.035	0.0000	0.0000	31.72	0.098	0.098	0.0000	0.0000	0.0000
9	0.037	0.054	32.26	0.077	0.077	0.037	0.054	0.0000	0.0000	32.26	0.077	0.077	0.0000	0.0000	0.0000
12	0.045	0.072	32.42	0.055	0.055	0.045	0.072	0.0000	0.0000	32.42	0.055	0.055	0.0000	0.0000	0.0000
15	0.051	0.091	31.90	0.034	0.034	0.051	0.091	0.0000	0.0000	31.90	0.034	0.034	0.0000	0.0000	0.0000
18.06	0.055	0.110	30.00	0.013	0.013	0.055	0.110	0.0000	0.0000	30.00	0.013	0.013	0.0000	0.0000	0.0000
Parametric Transformation Cam Path Equations															
0	0.000	0.000	30.00	0.134	0.134	0.000	0.000	0.0000	0.0000	30.00	0.134	0.134	0.0000	0.0000	0.0000
3	0.014	0.017	30.94	0.119	0.119	0.014	0.017	0.0000	0.0000	30.94	0.119	0.119	0.0000	0.0000	0.0000
6	0.027	0.035	31.72	0.098	0.098	0.027	0.035	0.0000	0.0000	31.72	0.098	0.098	0.0000	0.0000	0.0000
9	0.037	0.054	32.26	0.077	0.077	0.037	0.054	0.0000	0.0000	32.26	0.077	0.077	0.0000	0.0000	0.0000
12	0.045	0.072	32.42	0.055	0.055	0.045	0.072	0.0000	0.0000	32.42	0.055	0.055	0.0000	0.0000	0.0000
15	0.051	0.091	31.90	0.034	0.034	0.051	0.091	0.0000	0.0000	31.90	0.034	0.034	0.0000	0.0000	0.0000
18.06	0.055	0.110	30.00	0.013	0.013	0.055	0.110	0.0000	0.0000	30.00	0.013	0.013	0.0000	0.0000	0.0000

Continued

(b)

Incr. (θ)	Expected Cam Path Points		Expected Self-Centering Points			Actual Cam Path Points with Percent Error				Actual Self-Centering Points with Percent Error					
Parametric Trigonometric Cam Path Equations															
θ	x_c	y_c	φ	R_{RG}	R_{TG}	x_c	y_c	E_{xc}	E_{yc}	φ	R_{RG}	R_{TG}	E_{φ}	E_{RG}	E_{TG}
(deg)	(m)	(m)	(deg)	(m)	(m)	(m)	(m)	(%)	(%)	(deg)	(m)	(m)	(%)	(%)	(%)
0	0.000	0.000	30.00	0.134	0.134	0.000	0.000	0.0000	0.0000	30.00	0.134	0.134	0.0000	0.0000	0.0000
3	0.010	0.019	30.94	0.119	0.119	0.010	0.019	0.0000	0.0000	30.94	0.119	0.119	0.0000	0.0000	0.0000
6	0.019	0.039	31.72	0.098	0.098	0.019	0.039	0.0000	0.0000	31.72	0.098	0.098	0.0000	0.0000	0.0000
9	0.028	0.057	32.26	0.077	0.077	0.028	0.057	0.0000	0.0000	32.26	0.077	0.077	0.0000	0.0000	0.0000
12	0.037	0.075	32.42	0.055	0.055	0.037	0.075	0.0000	0.0000	32.42	0.055	0.055	0.0000	0.0000	0.0000
15	0.046	0.093	31.90	0.034	0.034	0.046	0.093	0.0000	0.0000	31.90	0.034	0.034	0.0000	0.0000	0.0000
18.06	0.055	0.110	30.00	0.013	0.013	0.055	0.110	0.0000	0.0000	30.00	0.013	0.013	0.0000	0.0000	0.0000
Parametric Loop-Closure Cam Path Equations															
0	0.000	0.000	30.00	0.134	0.134	0.000	0.000	0.0000	0.0000	30.00	0.134	0.134	0.0000	0.0000	0.0000
3	0.010	0.019	30.94	0.119	0.119	0.010	0.019	0.0000	0.0000	30.94	0.119	0.119	0.0000	0.0000	0.0000
6	0.019	0.039	31.72	0.098	0.098	0.019	0.039	0.0000	0.0000	31.72	0.098	0.098	0.0000	0.0000	0.0000
9	0.028	0.057	32.26	0.077	0.077	0.028	0.057	0.0000	0.0000	32.26	0.077	0.077	0.0000	0.0000	0.0000
12	0.037	0.075	32.42	0.055	0.055	0.037	0.075	0.0000	0.0000	32.42	0.055	0.055	0.0000	0.0000	0.0000
15	0.046	0.093	31.90	0.034	0.034	0.046	0.093	0.0000	0.0000	31.90	0.034	0.034	0.0000	0.0000	0.0000
18.06	0.055	0.110	30.00	0.013	0.013	0.055	0.110	0.0000	0.0000	30.00	0.013	0.013	0.0000	0.0000	0.0000
Parametric Transformation Cam Path Equations															
0	0.000	0.000	30.00	0.134	0.134	0.000	0.000	0.0000	0.0000	30.00	0.134	0.134	0.0000	0.0000	0.0000
3	0.010	0.019	30.94	0.119	0.119	0.010	0.019	0.0000	0.0000	30.94	0.119	0.119	0.0000	0.0000	0.0000
6	0.019	0.039	31.72	0.098	0.098	0.019	0.039	0.0000	0.0000	31.72	0.098	0.098	0.0000	0.0000	0.0000
9	0.028	0.057	32.26	0.077	0.077	0.028	0.057	0.0000	0.0000	32.26	0.077	0.077	0.0000	0.0000	0.0000
12	0.037	0.075	32.42	0.055	0.055	0.037	0.075	0.0000	0.0000	32.42	0.055	0.055	0.0000	0.0000	0.0000
15	0.046	0.093	31.90	0.034	0.034	0.046	0.093	0.0000	0.0000	31.90	0.034	0.034	0.0000	0.0000	0.0000
18.06	0.055	0.110	30.00	0.013	0.013	0.055	0.110	0.0000	0.0000	30.00	0.013	0.013	0.0000	0.0000	0.0000

technique due to the concept of changing variables leading to cancellation of the maximum horizontal component.

As confirmed, parametric equations and rectangular form conversion methods using trigonometric substitution & transformation are more accurate than using the Taylor series approach (although rather negligible in error for this design case). Moreover, it is a matter of choice on whether to use parametric, rectangular, or normalized forms of the cam path equations. Of the various forms presented,

Table 2. Rectangular form cam contour and associated self-centering points validation (a) inverse wedge cam, (b) regular wedge cam.

(a)

Incr. (θ)	Expected Cam Path Points		Expected Self-Centering Points			Incr. (x_c)	Actual Cam Path Points with Percent Error				Actual Self-Centering Points with Percent Error					
Taylor Series Approximation																
θ (deg)	x_c (m)	y_c (m)	φ (deg)	R_{RG} (m)	R_{TG} (m)	x_c (m)	θ (deg)	y_c (m)	E_θ (%)	E_{yc} (%)	φ (deg)	R_{RG} (m)	R_{TG} (m)	E_φ (%)	E_{RG} (%)	E_{TG} (%)
0	0.000	0.000	30.00	0.134	0.134	0.000	0.00	0.000	0.0000	0.0000	30.00	0.134	0.134	0.0000	0.0000	0.0000
3	0.014	0.017	30.94	0.119	0.119	0.014	3.00	0.017	0.0000	0.0000	30.94	0.119	0.119	0.0000	0.0000	0.0000
6	0.027	0.035	31.72	0.098	0.098	0.027	6.00	0.035	0.0000	0.0000	31.72	0.098	0.098	0.0000	0.0000	0.0000
9	0.037	0.054	32.26	0.077	0.077	0.037	9.00	0.054	0.0000	0.0000	32.26	0.077	0.077	0.0000	0.0000	0.0000
12	0.045	0.072	32.42	0.055	0.055	0.045	12.00	0.072	0.0000	0.0000	32.42	0.055	0.055	0.0000	0.0000	0.0000
15	0.051	0.091	31.90	0.034	0.034	0.051	15.00	0.091	0.0000	0.0000	31.90	0.034	0.034	0.0000	0.0000	0.0000
18.06	0.055	0.110	30.00	0.013	0.013	0.055	18.06	0.110	0.0000	0.0000	30.00	0.013	0.013	0.0000	0.0001	0.0001
Trigonometric Substitution & Transformation																
0	0.000	0.000	30.00	0.134	0.134	0.000	0.00	0.000	0.0000	0.0000	30.00	0.134	0.134	0.0000	0.0000	0.0000
3	0.014	0.017	30.94	0.119	0.119	0.014	3.00	0.017	0.0000	0.0000	30.94	0.119	0.119	0.0000	0.0000	0.0000
6	0.027	0.035	31.72	0.098	0.098	0.027	6.00	0.035	0.0000	0.0000	31.72	0.098	0.098	0.0000	0.0000	0.0000
9	0.037	0.054	32.26	0.077	0.077	0.037	9.00	0.054	0.0000	0.0000	32.26	0.077	0.077	0.0000	0.0000	0.0000
12	0.045	0.072	32.42	0.055	0.055	0.045	12.00	0.072	0.0000	0.0000	32.42	0.055	0.055	0.0000	0.0000	0.0000
15	0.051	0.091	31.90	0.034	0.034	0.051	15.00	0.091	0.0000	0.0000	31.90	0.034	0.034	0.0000	0.0000	0.0000
18.06	0.055	0.110	30.00	0.013	0.013	0.055	18.06	0.110	0.0000	0.0000	30.00	0.013	0.013	0.0000	0.0000	0.0000
Nonlinear ODE Using the Taylor Series Approximation																
0	0.000	0.000	30.00	0.134	0.134	0.000	0.00	0.000	0.0000	0.0000	30.00	0.134	0.134	0.0000	0.0000	0.0000
3	0.014	0.017	30.94	0.119	0.119	0.014	3.00	0.017	0.0000	0.0000	30.94	0.119	0.119	0.0000	0.0000	0.0000
6	0.027	0.035	31.72	0.098	0.098	0.027	6.00	0.035	0.0000	0.0000	31.72	0.098	0.098	0.0000	0.0000	0.0000
9	0.037	0.054	32.26	0.077	0.077	0.037	9.00	0.054	0.0000	0.0000	32.26	0.077	0.077	0.0000	0.0000	0.0000
12	0.045	0.072	32.42	0.055	0.055	0.045	12.00	0.072	0.0000	0.0000	32.42	0.055	0.055	0.0000	0.0000	0.0000
15	0.051	0.091	31.90	0.034	0.034	0.051	15.00	0.091	0.0000	0.0000	31.90	0.034	0.034	0.0000	0.0000	0.0000
18.06	0.055	0.110	30.00	0.013	0.013	0.055	18.06	0.110	0.0000	0.0000	30.00	0.013	0.013	0.0000	0.0001	0.0001
Nonlinear ODE Using Trigonometric Substitution & Transformation																
0	0.000	0.000	30.00	0.134	0.134	0.000	0.00	0.000	0.0000	0.0000	30.00	0.134	0.134	0.0000	0.0000	0.0000
3	0.014	0.017	30.94	0.119	0.119	0.014	3.00	0.017	0.0000	0.0000	30.94	0.119	0.119	0.0000	0.0000	0.0000
6	0.027	0.035	31.72	0.098	0.098	0.027	6.00	0.035	0.0000	0.0000	31.72	0.098	0.098	0.0000	0.0000	0.0000
9	0.037	0.054	32.26	0.077	0.077	0.037	9.00	0.054	0.0000	0.0000	32.26	0.077	0.077	0.0000	0.0000	0.0000

Continued

12	0.045	0.072	32.42	0.055	0.055	0.045	12.00	0.072	0.0000	0.0000	32.42	0.055	0.055	0.0000	0.0000	0.0000
15	0.051	0.091	31.90	0.034	0.034	0.051	15.00	0.091	0.0000	0.0000	31.90	0.034	0.034	0.0000	0.0000	0.0000
18.06	0.055	0.110	30.00	0.013	0.013	0.055	18.06	0.110	0.0000	0.0000	30.00	0.013	0.013	0.0000	0.0000	0.0000

(b)

Incr. (θ)	Expected Cam Path Points		Expected Self-Centering Points			Incr. (x_c)	Actual Cam Path Points with Percent Error				Actual Self-Centering Points with Percent Error					
							Taylor Series Approximation									
θ (deg)	x_c (m)	y_c (m)	φ (deg)	R_{RG} (m)	R_{TG} (m)	x_c (m)	θ (deg)	y_c (m)	E_θ (%)	E_{yc} (%)	φ (deg)	R_{RG} (m)	R_{TG} (m)	E_φ (%)	E_{RG} (%)	E_{TG} (%)
0	0.000	0.000	30.00	0.134	0.134	0.000	0.00	0.000	0.0000	0.0000	30.00	0.134	0.134	0.0000	0.0000	0.0000
3	0.010	0.019	30.94	0.119	0.119	0.010	3.00	0.019	0.0000	0.0000	30.94	0.119	0.119	0.0000	0.0000	0.0000
6	0.019	0.039	31.72	0.098	0.098	0.019	6.00	0.039	0.0000	0.0000	31.72	0.098	0.098	0.0000	0.0000	0.0000
9	0.028	0.057	32.26	0.077	0.077	0.028	9.00	0.057	0.0000	0.0000	32.26	0.077	0.077	0.0000	0.0000	0.0000
12	0.037	0.075	32.42	0.055	0.055	0.037	12.00	0.075	0.0000	0.0000	32.42	0.055	0.055	0.0000	0.0000	0.0000
15	0.046	0.093	31.90	0.034	0.034	0.046	15.00	0.093	0.0000	0.0000	31.90	0.034	0.034	0.0000	0.0000	0.0000
18.06	0.055	0.110	30.00	0.013	0.013	0.055	18.06	0.110	0.0000	0.0000	30.00	0.013	0.013	0.0000	0.0000	0.0000
							Trigonometric Substitution & Transformation									
0	0.000	0.000	30.00	0.134	0.134	0.000	0.00	0.000	0.0000	0.0000	30.00	0.134	0.134	0.0000	0.0000	0.0000
3	0.010	0.019	30.94	0.119	0.119	0.010	3.00	0.019	0.0000	0.0000	30.94	0.119	0.119	0.0000	0.0000	0.0000
6	0.019	0.039	31.72	0.098	0.098	0.019	6.00	0.039	0.0000	0.0000	31.72	0.098	0.098	0.0000	0.0000	0.0000
9	0.028	0.057	32.26	0.077	0.077	0.028	9.00	0.057	0.0000	0.0000	32.26	0.077	0.077	0.0000	0.0000	0.0000
12	0.037	0.075	32.42	0.055	0.055	0.037	12.00	0.075	0.0000	0.0000	32.42	0.055	0.055	0.0000	0.0000	0.0000
15	0.046	0.093	31.90	0.034	0.034	0.046	15.00	0.093	0.0000	0.0000	31.90	0.034	0.034	0.0000	0.0000	0.0000
18.06	0.055	0.110	30.00	0.013	0.013	0.055	18.06	0.110	0.0000	0.0000	30.00	0.013	0.013	0.0000	0.0000	0.0000
							Nonlinear ODE Using the Taylor Series Approximation									
0	0.000	0.000	30.00	0.134	0.134	0.000	0.00	0.000	0.0000	0.0000	30.00	0.134	0.134	0.0000	0.0000	0.0000
3	0.010	0.019	30.94	0.119	0.119	0.010	3.00	0.019	0.0000	0.0000	30.94	0.119	0.119	0.0000	0.0000	0.0000
6	0.019	0.039	31.72	0.098	0.098	0.019	6.00	0.039	0.0000	0.0000	31.72	0.098	0.098	0.0000	0.0000	0.0000
9	0.028	0.057	32.26	0.077	0.077	0.028	9.00	0.057	0.0000	0.0000	32.26	0.077	0.077	0.0000	0.0000	0.0000
12	0.037	0.075	32.42	0.055	0.055	0.037	12.00	0.075	0.0000	0.0000	32.42	0.055	0.055	0.0000	0.0000	0.0000
15	0.046	0.093	31.90	0.034	0.034	0.046	15.00	0.093	0.0000	0.0000	31.90	0.034	0.034	0.0000	0.0000	0.0000
18.06	0.055	0.110	30.00	0.013	0.013	0.055	18.06	0.110	0.0000	0.0000	30.00	0.013	0.013	0.0000	0.0000	0.0000
							Nonlinear ODE Using Trigonometric Substitution & Transformation									
0	0.000	0.000	30.00	0.134	0.134	0.000	0.00	0.000	0.0000	0.0000	30.00	0.134	0.134	0.0000	0.0000	0.0000
3	0.010	0.019	30.94	0.119	0.119	0.010	3.00	0.019	0.0000	0.0000	30.94	0.119	0.119	0.0000	0.0000	0.0000

Continued

6	0.019	0.039	31.72	0.098	0.098	0.019	6.00	0.039	0.0000	0.0000	31.72	0.098	0.098	0.0000	0.0000	0.0000
9	0.028	0.057	32.26	0.077	0.077	0.028	9.00	0.057	0.0000	0.0000	32.26	0.077	0.077	0.0000	0.0000	0.0000
12	0.037	0.075	32.42	0.055	0.055	0.037	12.00	0.075	0.0000	0.0000	32.42	0.055	0.055	0.0000	0.0000	0.0000
15	0.046	0.093	31.90	0.034	0.034	0.046	15.00	0.093	0.0000	0.0000	31.90	0.034	0.034	0.0000	0.0000	0.0000
18.06	0.055	0.110	30.00	0.013	0.013	0.055	18.06	0.110	0.0000	0.0000	30.00	0.013	0.013	0.0000	0.0000	0.0000

it is also a matter choice on whether to use the trigonometric, combined loop-closure with vector projection/resolution, transformation equation, Taylor series, trigonometric substitution & transformation, or nonlinear ODE solution methods depending on which is more convenient/preferred within the design environment in connection with associated design intent.

Nevertheless, and for additional validation of the combined loop-closure with vector projection/resolution method, Table 3 is provided below to show that all associated summation equations equate to values of zero, as expected. With having confirmation of the kinematic self-centering theory, validation of the static equilibrium equations and associated closed-form force equations will commence.

4.2. Statics Validation

Regarding statics validation, various contact, normal, and reaction forces generated from computer-aided engineering simulation are compared against calculated values derived from solving a system of force equilibrium equations of the entire system with observing that the results are very close to within reason along with all equilibrium equations summing to zero. However, and to note, a self-centering design utilizing the regular wedge cam type is utilized for validation purposes due to technical difficulties occurring in the computer-aided engineering simulation environment arising from the more complex inverse wedge cam. It is important to point out that the statics are virtually the same between both types except for the pressure angle, normal cam path angle, and moment arm distance $\vec{R}_{O2\,D1}$ vs. $\vec{R}_{O2\,D2}$ which is either changing (inverse wedge cam) or fixed (regular wedge cam) over the cam rotation range. Nevertheless, and at any instant in time/cam rotation, a comparison can be appropriately and accurately made with either applied design configuration due to the formulation of the statics equations being identical for either regular or inverse wedge cam design type.

In connection, an activation force of $F_a = 100$ lb. (445 N) is applied along with normal (friction related) force moment arm lengths of $x_{m1} = 3$ in. (0.0762 m), $y_{m1} = 12$ in. (0.3048 m), $x_{m2} = 0.75$ in. (0.0191 m), and $y_{m2} = 27.125$ in. (0.6889 m) relative to the origin of the workpiece.

In the example shown within Figure 9, the static friction coefficient μ_s and external moment components (M_{extx}, M_{exty}, and M_{extz}) are assigned values of zero. Additionally, vertical external loadings applied on the workpiece at two locations (out-of-plane), as shown in Figure 9 for F_{wpy}, provide a value of $F_{wpy} = -23.125$

Table 3. Loop-closure equations (a) inverse wedge cam, (b) regular wedge cam.

(a)

Loop-Closure with Vector Projection Method

Incr.	Vector Magnitudes								Vector Summations		
θ (deg)	R_{BO_2} (m)	R_{O_1B} (m)	R_{AO_1} (m)	R_{D_1A} (m)	$R_{O_2D_1}$ (m)	R_{D_2A} (m)	$R_{O_2D_2}$ (m)	$R_{D_1D_2}$ (m)	ΣR_1 (m)	ΣR_2 (m)	ΣR_3 (m)
0	0.4051	0.1906	0.1906	0.5781	0.3030	0.5481	0.3030	0.0000	0.0000	0.0000	0.0000
3	0.4051	0.1696	0.1696	0.5781	0.2828	0.5704	0.3030	0.0223	0.0000	0.0000	0.0000
6	0.4051	0.1485	0.1485	0.5781	0.2626	0.5920	0.3030	0.0440	0.0000	0.0000	0.0000
9	0.4051	0.1274	0.1274	0.5781	0.2426	0.6130	0.3030	0.0649	0.0000	0.0000	0.0000
12	0.4051	0.1062	0.1062	0.5781	0.2227	0.6331	0.3030	0.0851	0.0000	0.0000	0.0000
15	0.4051	0.0850	0.0850	0.5781	0.2031	0.6525	0.3030	0.1045	0.0000	0.0000	0.0000
18.06	0.4051	0.0635	0.0635	0.5781	0.1836	0.6714	0.3030	0.1233	0.0000	0.0000	0.0000

(b)

Loop-Closure with Vector Resolution Method

Incr.	Vector Magnitudes								Vector Summations		
θ (deg)	R_{BO_2} (m)	R_{O_1B} (m)	R_{AO_1} (m)	R_{D_1A} (m)	$R_{O_2D_1}$ (m)	R_{D_2A} (m)	$R_{O_2D_2}$ (m)	$R_{D_1D_2}$ (m)	ΣR_1 (m)	ΣR_2 (m)	ΣR_3 (m)
0	0.4051	0.1906	0.1906	0.4331	0.1834	0.4331	0.1834	0.0000	0.0000	0.0000	0.0000
3	0.4051	0.1696	0.1696	0.4331	0.1626	0.4529	0.1834	0.0216	0.0000	0.0000	0.0000
6	0.4051	0.1485	0.1485	0.4331	0.1418	0.4724	0.1834	0.0428	0.0000	0.0000	0.0000
9	0.4051	0.1274	0.1274	0.4331	0.1210	0.4917	0.1834	0.0636	0.0000	0.0000	0.0000
12	0.4051	0.1062	0.1062	0.4331	0.1004	0.5107	0.1834	0.0839	0.0000	0.0000	0.0000
15	0.4051	0.0850	0.0850	0.4331	0.0801	0.5294	0.1834	0.1037	0.0000	0.0000	0.0000
18.06	0.4051	0.0635	0.0635	0.4331	0.0601	0.5479	0.1834	0.1233	0.0000	0.0000	0.0000

lb. (−103 N) located at the x - y mechanism plane. Due to there being no horizontal loading F_{wpx}, the resulting forces are symmetrical with respect to each other and about the centerline of the mechanism, as expected. The associated comparison indicates 6.39% of maximum percent error (1.84% average error).

As a more thorough example, the static friction coefficient μ_s has a value of 0.3 along with external moment components (M_{extx} , M_{exty} ,and M_{extz}) defined as zero. Additionally, vertical and horizontal loadings are applied along the workpiece as shown in Figure 10 below (giving totals of $F_{wpx} = -4.6875$ lb. (-20.85 N) and $F_{wpy} = -23.125$ lb. (−103 N) located at the x - y mechanism plane) with observing that the results are also very close to each other and within acceptable reason. However, and regarding the asymmetrical case, due to the presence of horizontal loading on the workpiece, the forces are not symmetrical about

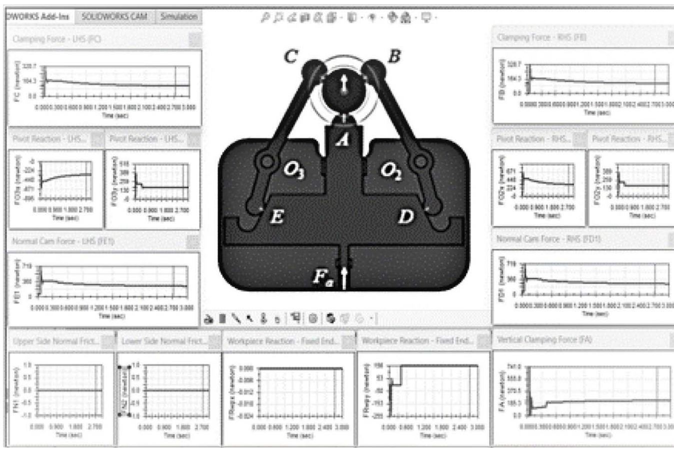

(N)	Given		Max. Error
F_a	445 @ Actuator ($z = 0$ m)		6.39%
F_{wp_x}	0 Along WP ($z = 1.37$ m)		Avg. Error
F_{wp_y}	-178 ($z = 0.914$ m); -89 ($z = 1.37$ m)		1.84%
(N)	Simulated	Theory	Error %
F_A	226.19	221.26	2.23
F_B	110.81	117.78	0.87
F_C	110.81	117.78	0.87
F_{D_2}	247.99	251.24	1.28
F_{E_2}	247.99	251.24	1.28
F_{O_2x}	317.96	319.78	0.57
F_{O_2y}	165.74	170.99	3.07
F_{O_3x}	317.96	319.78	0.57
F_{O_3y}	165.74	170.99	3.07
F_{Rwp_x}	0.00	0.00	0.00
F_{Rwp_y}	153.55	164.05	6.39

Figure 9. Computer-aided symmetrical force simulation ($R_{tw} = 3.5$ in. [0.0889 m]).

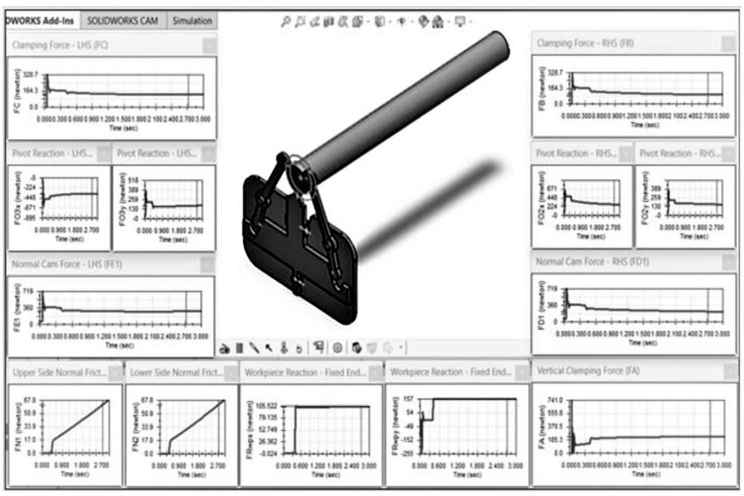

(N)	Given		Max. Error
F_a	445 @ Actuator ($z = 0$ m)		11.46%
F_{wp_x}	−133 Along WP ($z = 1.37$ m)		Avg. Error
F_{wp_y}	−178 ($z = 0.914$ m); −89 ($z = 1.37$ m)		5.58%
(N)	Simulated	Theory	Error %
F_A	227.88	226.41	0.65
F_B	96.86	104.36	10.06
F_C	127.66	128.91	0.96
F_{D_2}	216.27	234.51	7.78
F_{E_2}	279.93	289.76	3.38
F_{O_2x}	267.83	298.52	10.29
F_{O_2y}	156.27	159.60	2.08
F_{O_3x}	367.33	368.85	0.41
F_{O_3y}	175.59	197.19	11.46
F_{Rwp_x}	103.64	112.58	7.95
F_{Rwp_y}	153.60	164.05	6.37

Figure 10. Computer-aided asymmetrical force simulation ($R_{tw} = 3.5$ in. [0.0889 m]).

the mechanism's centerline, as expected. The associated comparison indicates 11.46% of maximum percent error (5.58% average error).

Lastly, the equilibrium equations for both examples sum to zero as shown in Table 4 and Table 5 below thereby validating the generalized theoretical statics formulation of closed-form force equations in terms of kinematic and given force parameters.

Table 4. Equilibrium summations for symmetrical example.

Symmetric Static Equilibrium														
Incr.	Force Magnitudes										Force Summations			
θ (deg)	F_A (N)	F_B (N)	F_C (N)	F_{D_2} (N)	F_{E_2} (N)	F_{N_1} (N)	F_{N_2} (N)	F_{O_2x} (N)	F_{O_2y} (N)	F_{O_3x} (N)	F_{O_3y} (N)	ΣF_x (N)	ΣF_y (N)	ΣM_{O_1z} (N × m)
0	216.9	114.0	114.0	169.0	169.0	0.0000	0.0000	−223.4	−171.0	−223.4	−171.0	0.0000	0.0000	0.0000
3	225.7	119.5	119.5	181.5	181.5	0.0000	0.0000	−247.2	−171.0	−247.2	−171.0	0.0000	0.0000	0.0000
6	235.2	125.9	125.9	199.3	199.3	0.0000	0.0000	276.6	−171.0	276.6	−171.0	0.0000	0.0000	0.0000
9	245.9	134.0	134.0	225.2	225.2	0.0000	0.0000	−315.4	−171.0	−315.4	−171.0	0.0000	0.0000	0.0000
12	258.7	145.4	145.4	264.5	264.5	0.0000	0.0000	−370.3	−171.0	−370.3	−171.0	0.0000	0.0000	0.0000
15	275.4	163.0	163.0	328.4	328.4	0.0000	0.0000	−445.9	−171.0	−445.9	−171.0	0.0000	0.0000	0.0000
18.06	300.3	197.5	197.5	449.6	449.6	0.0000	0.0000	−614.9	−171.0	−614.9	−171.0	0.0000	0.0000	0.0000

Table 5. Equilibrium summations for asymmetrical example.

Asymmetric Static Equilibrium														
Incr.	Force Magnitudes										Force Summations			
θ (deg)	F_A (N)	F_B (N)	F_C (N)	F_{D_2} (N)	F_{E_2} (N)	F_{N_1} (N)	F_{N_2} (N)	F_{O_2x} (N)	F_{O_2y} (N)	F_{O_3x} (N)	F_{O_3y} (N)	ΣF_x (N)	ΣF_y (N)	ΣM_{O_1z} (N × m)
0	219.5	104.6	128.7	155.0	190.7	5.410	−31.75	−205.0	−156.9	252.2	−193.0	0.0000	0.0000	0.0000
3	228.9	110.4	134.7	167.7	204.6	2.770	−32.21	−228.4	−158.0	278.7	−192.8	0.0000	0.0000	0.0000
6	239.1	117.3	141.8	185.7	224.5	−0.270	−32.75	−257.7	−159.3	311.6	−192.6	0.0000	0.0000	0.0000
9	250.6	126.0	150.7	211.8	253.3	−3.840	−33.34	−296.7	−160.8	354.7	−192.3	0.0000	0.0000	0.0000
12	264.4	138.4	163.1	251.7	296.7	−8.140	−33.92	−352.5	−162.8	415.4	−191.8	0.0000	0.0000	0.0000
15	282.6	157.8	182.4	317.5	366.9	−13.36	−34.37	−440.7	−165.3	509.3	−191.0	0.0000	0.0000	0.0000
18.06	309.7	194.9	218.9	443.6	498.4	−19.70	−34.40	−606.6	−168.7	681.5	−189.5	0.0000	0.0000	0.0000

4.3. Translational Gripper, Rotational Gripper, and Cam Dynamics Validation

Regarding the models previously shown within Figure 8 along with prior related discussion, computer-aided designs were used in conjunction with parametric transformation equations of the cam profiles for developing and validating the geometric cam paths and self-centering function(s) theory (strictly derived from the input of parametric equations). In connection, computer-aided engineering motion simulation is utilized along with linear displacement and angular dynamic equations, both independent to the geometric path(s) and to each other, to drive the vertical translational and rotational grippers respectively with a specified activation force of $F_a = 100$ lb. (445 N) and power source of $P_c = 50$ lb. × in./sec (5.649 N × m/sec). Moreover, the maximum angle and associated time are prescribed through utilization of maximum cam rotation (developed from URAM theory) and constant power equations.

Furthermore, as shown within **Figure 11** below, the graphical trace path output(s) are developed from the translational and rotational dynamic equations while noting that their path(s) independently and exactly match the geometrical path(s) formed from the parametric transformation equations. Additionally, and although unable to be shown without a dynamic animation, the mechanism(s) stop at the minimum workpiece diameter regarding the maximum angle and associated time using URAM theory, also being independent to the geometric path(s). In connection, it is observed that self-centering is achieved and that the auto-generated dynamics graphs within **Figure 11** match the graphs produced from theory as shown in **Figure 12** and **Figure 13** below.

Moreover, an extra layer of validation for the translational and angular dynamics in addition to validation regarding the curvilinear rotational gripper and curvilinear cam dynamics provided in **Figures 12-16** is explored through various calculus principles as shown in the following presentment.

In connection, through inspection of the associated graphs in **Figure 12(a)** through **Figure 16(a)** and their first, second, and third derivatives regarding critical and inflection points as well as local and global maxima/minima and related concavity aspects, the resulting dynamics appear reasonable and in alignment with what would be expected. In relation, first derivatives testing is utilized to provide insights toward important features on the original corresponding graphs. For example, through observation of the angular velocity graph in **Figure 13(b)**, it is noted that its sign does not change direction at the local minimum, therefore indicating that this critical point (which is located at approximately 6.4 seconds) is also an inflection point on the angular position graph (that cannot be easily seen due to scaling). Additionally, the sign of the angular acceleration graph is negative to the left of the critical point and positive to the right of the critical point thus implying that this critical point is also a local minimum on the angular velocity curve. Moreover, the angular jerk is always positive therefore indicating that the angular acceleration has an inflection point (that again cannot be easily seen due to scaling).

Moving further, second derivatives are used for determining the concavity of their original graphs. With the angular acceleration in **Figure 13(c)** changing sign in addition to the second derivative being zero at this point, there is an inflection point on the angular position graph at that same abscissa point (which is in agreement

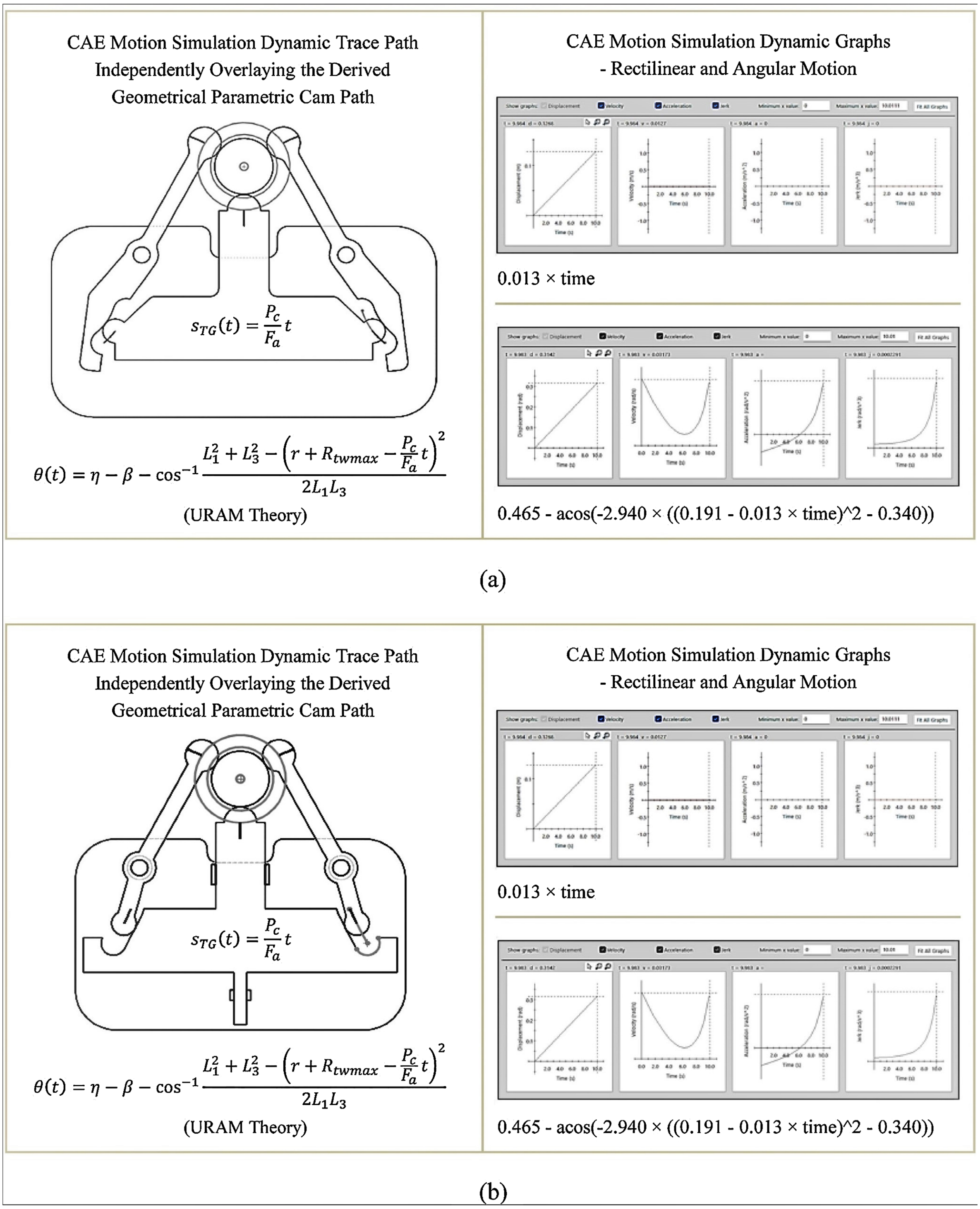

Figure 11. Computer-aided dynamic simulation (a) ınverse wedge cam, (b) regular wedge cam.

with the previous discussion). Furthermore, and with the angular jerk always being positive in terms of concavity, there is a local minimum on the angular velocity graph which is also in agreement with the previous discussion involving first derivatives. Lastly, and in relation to various derivative aspects, graphical validation follows a similar pattern for the curvilinear rotational gripper and cam

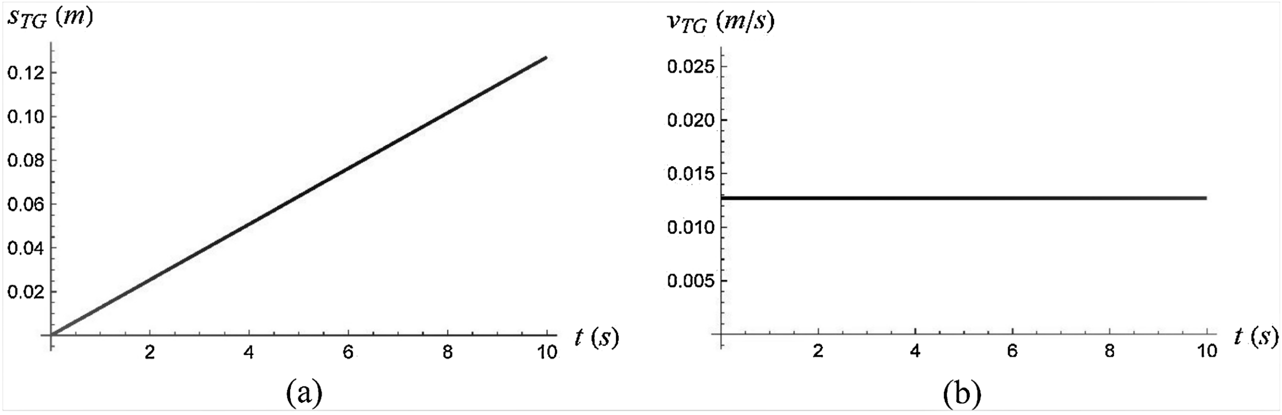

Figure 12. Rectilinear self-centering translational gripper position and velocity for both cam designs.

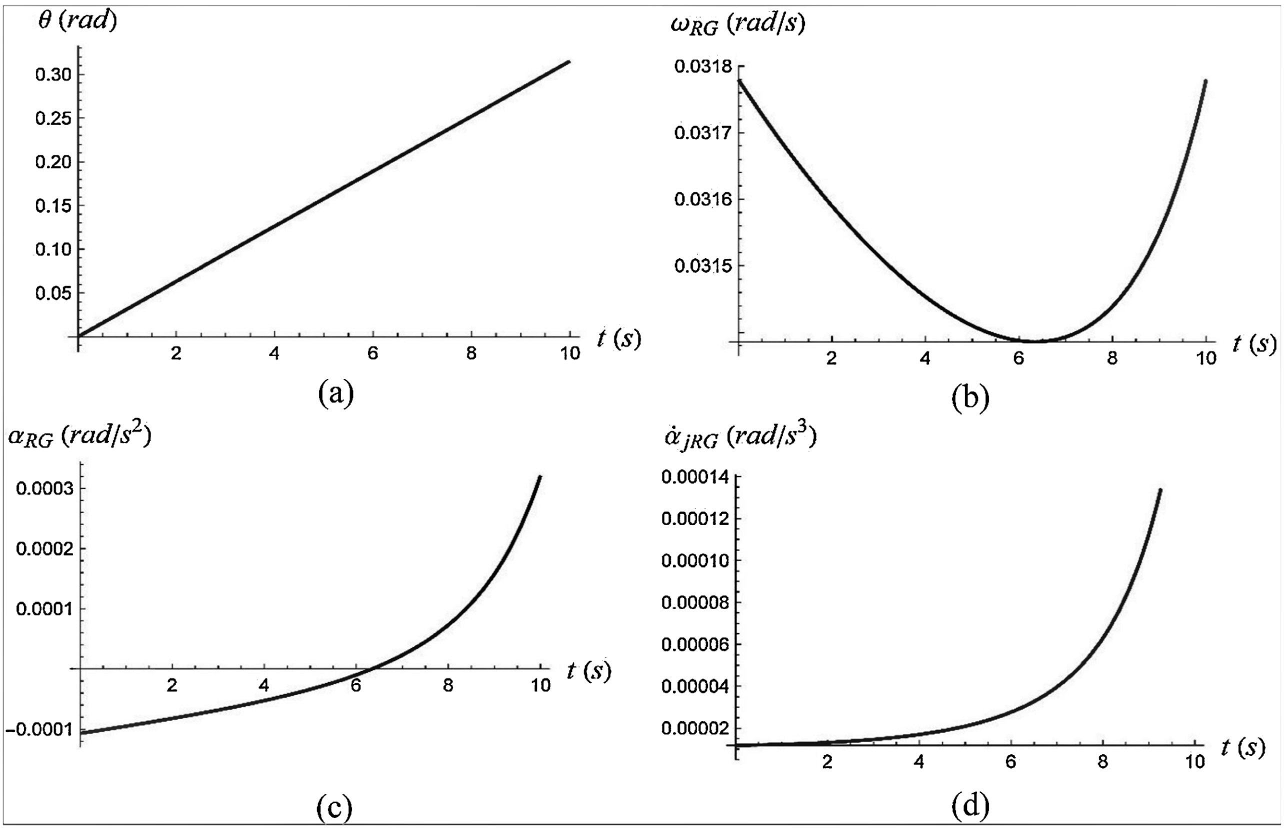

Figure 13. Angular rotational gripper position, velocity, acceleration, and jerk for both cam designs.

dynamics shown in **Figures 14-16** as previously described in the above discussion regarding angular dynamics. Note that the results of **Figure 12** are not mentioned in this discussion due to the graphical understanding being self-evident in nature (*i.e.* the derivative of a linear function produces a horizontal line for constant velocity).

Moreover, basic engineering judgment is utilized with related average speed calculations for gaining a sense of numerical values for the first derivatives of position. Regarding such, and since it is known that the rotational gripper rotates

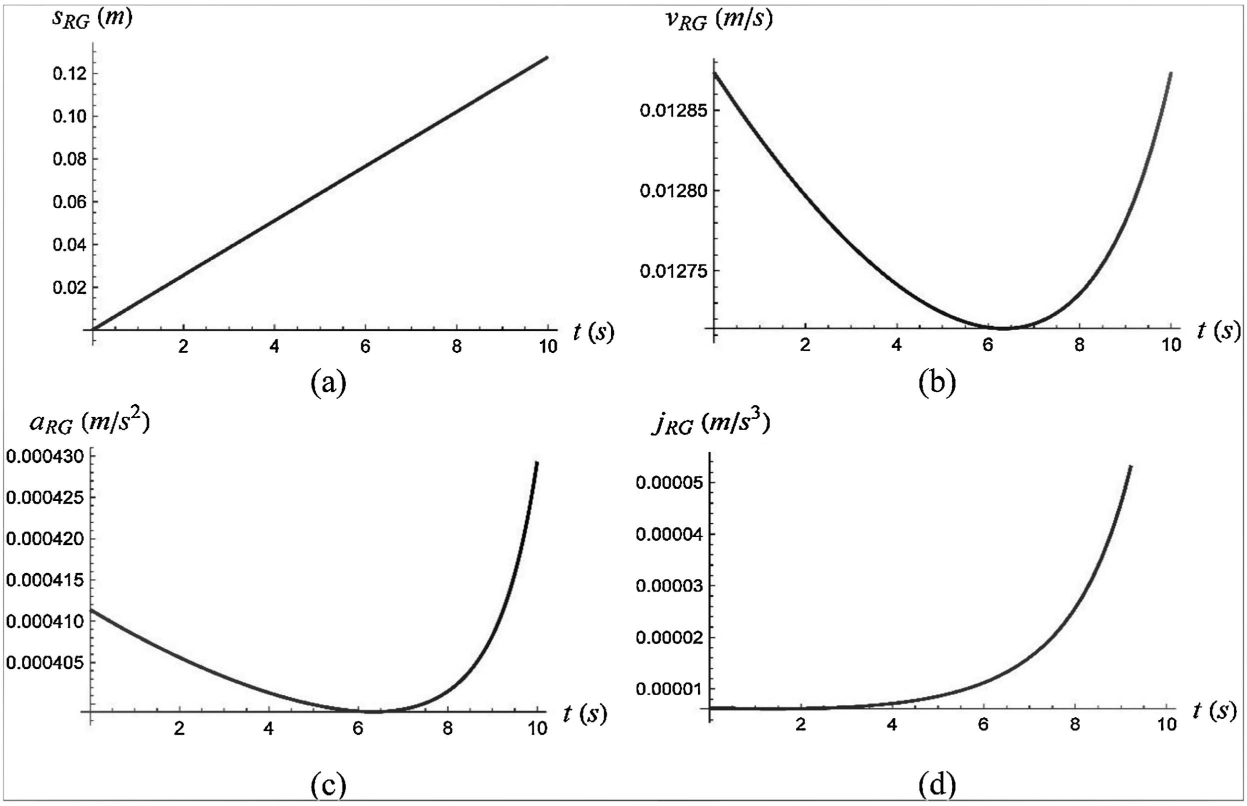

Figure 14. Curvilinear rotational gripper position, velocity, acceleration, and jerk for both cam designs.

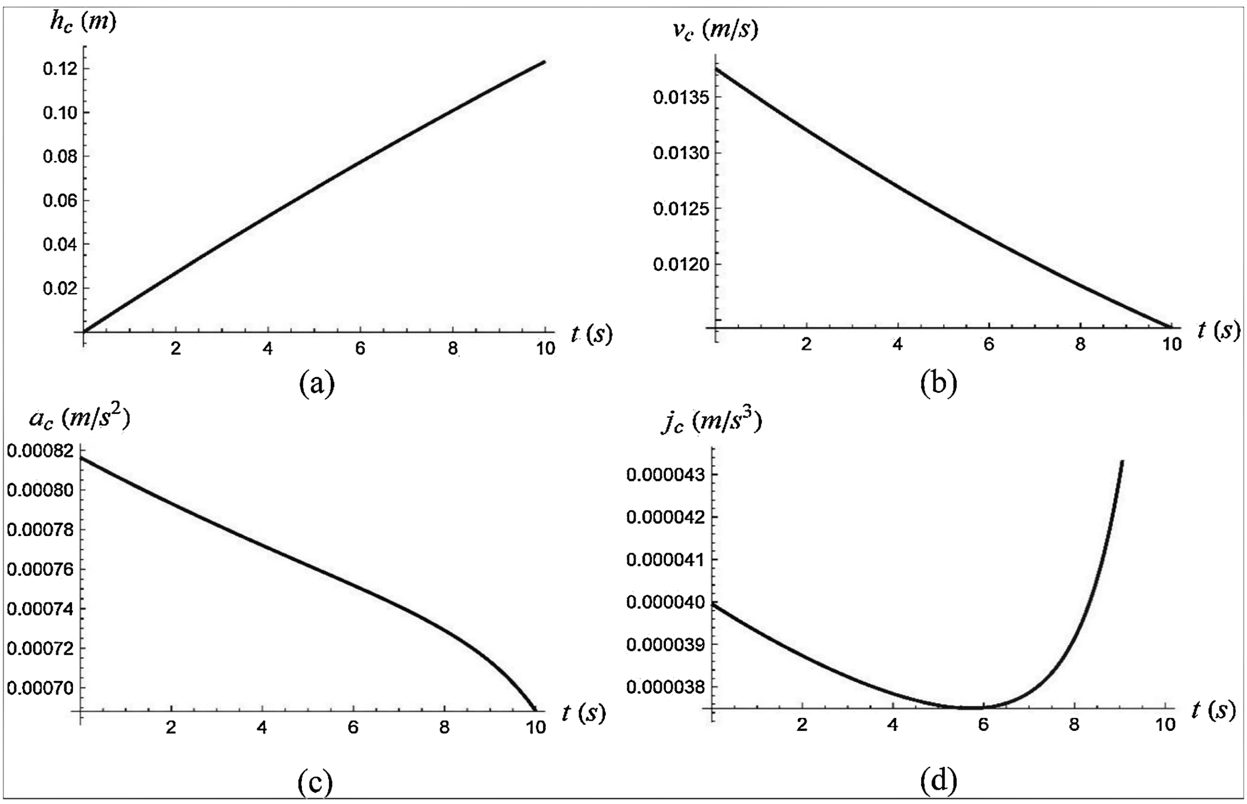

Figure 15. Curvilinear resultant ınverse wedge cam contour position, velocity, acceleration, and jerk.

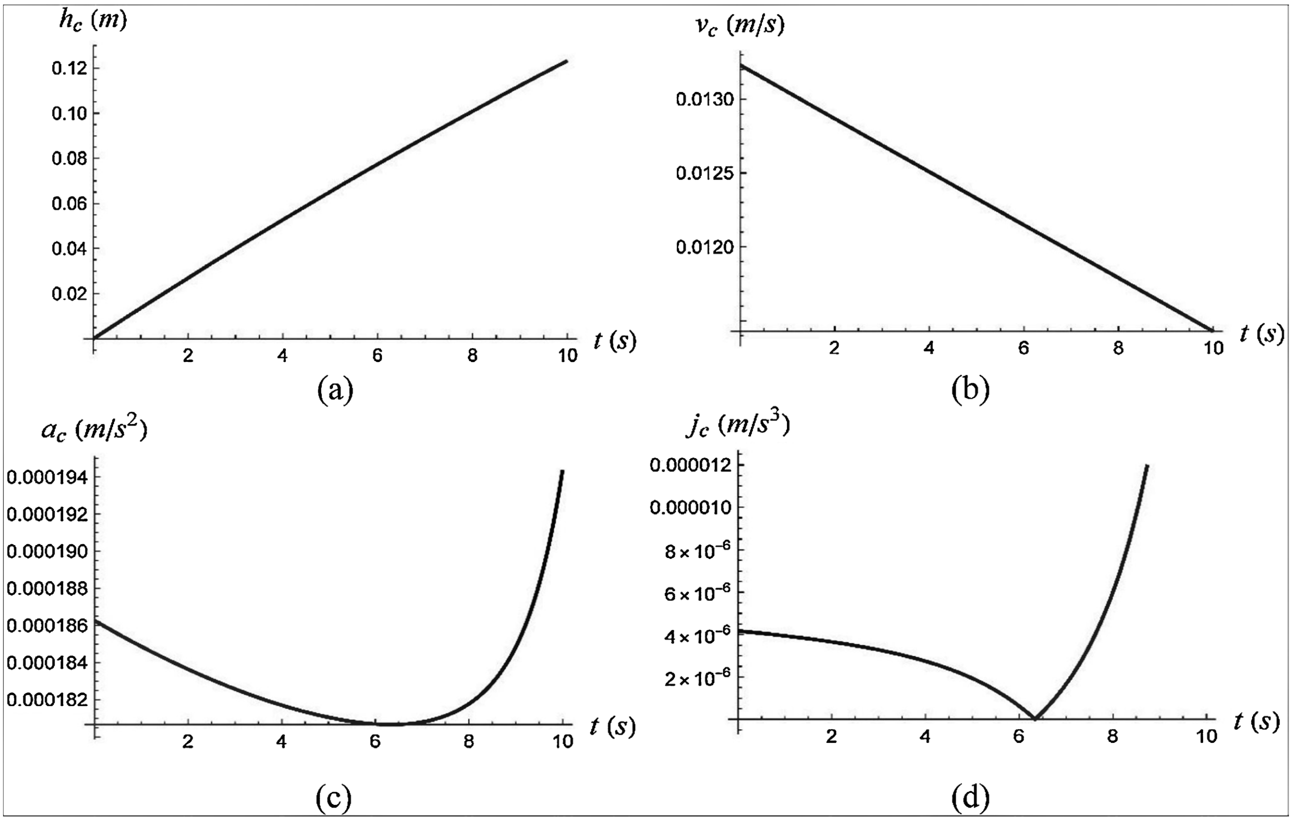

Figure 16. Curvilinear resultant regular wedge cam contour position, velocity, acceleration, and jerk.

approximately 18.06 degrees (0.315 radians) in 10.011 seconds over its full positional range, the angular velocity should be expected to be approximately equal to 0.031 (0.315/10.011) rad/sec. In comparison, this coincides with **Figure 13(b)** which shows the value to be 0.032 rad/sec. Additionally, and using the same procedure, the curvilinear rotational gripper velocity is 0.502 (5.03/10.011) in./sec vs. 0.506 in./sec (or 0.0128 (0.128/10.011) m/sec vs. 0.0129 m/sec) and the curvilinear inverse/regular cam velocity is 0.484 (4.86/10.011) in./sec vs. 0.449 in./sec (or 0.0123 (0.123/10.011) m/sec vs. 0.0114 m/sec). Also, and to note, the angular velocity times the first spatial derivative produces curvilinear velocity. In connection, the basic calculation approach provides 0.482 (15.06×0.032) in./sec (or 0.0122 (0.383×0.032) m/sec) in conjunction with the graphical approach showing 0.449 (14.031×0.032) in./sec (or 0.0114 (0.356×0.032) m/sec). These values are identical to the previous values obtained directly (in addition to being very close to one another). As noted, although rough first-pass approximations for first derivatives are discussed, the basic calculated values closely coincide with their corresponding graphs thereby providing a further level of validation in conjunction with also providing a good base level of engineering intuition regarding dynamics.

Furthermore, and with having each of the previously validated position equations and graphs, numerical techniques utilizing centered finite-difference Equations (214), (215), and (216) with corresponding results are shown within **Table 6** for providing close approximations in comparison with successive derivatives of the original positional graphs expressed in terms of exact equations.

Note that the numerical method and associated equations described (having an order of $O(h^4)$ error) are used instead of forward or backward finite-difference methods having an order of $O(h^2)$ error. Additionally, a step size of $h = 0.01$ is used for the rectilinear translational gripper, angular rotational gripper, and curvilinear cam dynamics. However, a step size of $h = 0.00005$ is used for the curvilinear rotational gripper dynamics due to sensitivity issues regarding the jerk equation.

$$\frac{\mathrm{d}f(x)}{\mathrm{d}x} = \frac{-f(x+2h)+8f(x+h)-8f(x-h)+f(x-2h)}{12h} \tag{214}$$

$$\frac{\mathrm{d}^2 f(x)}{\mathrm{d}x^2} = \frac{-f(x+2h)+16f(x+h)-30f(x)+16f(x-h)-f(x-2h)}{12h^2} \tag{215}$$

$$\begin{aligned}\frac{\mathrm{d}^3 f(x)}{\mathrm{d}x^3} = \frac{1}{8h^3}\big(&-f(x+3h)+8f(x+2h)-13f(x+h)\\ &+13f(x-h)-8f(x-2h)+f(x-3h)\big)\end{aligned} \tag{216}$$

Through observation of the error values within **Table 6**, indicating the maximum error between the exact dynamic equations vs. numerical methods is approximately 0.0079% for English units (0.0016% for metric units) for the inverse wedge cam and 0.0051% for English units (0.0016% for metric units) for the regular wedge cam, the centered finite-difference method for dynamic calculations validates the exact dynamic equations provided within the methodology. In relation to such, and in closing, computer-aided engineering dynamics simulation may follow as part of future exploratory efforts with a more thorough discussion pertaining to practical matters of cam design and associated optimization characteristics.

Table 6. Exact vs. approximate mechanism dynamics.

(a)

Incr.	Exact				Approximate			Percent Error		
Rectilinear Translational Gripper Dynamics										
t (s)	s_{TG} (m)	v_{TG} (m/s)	a_{TG} (m/s²)	j_{TG} (m/s³)	v_{TG} (m/s)	a_{TG} (m/s²)	j_{TG} (m/s³)	E_v (%)	E_a (%)	E_j (%)
0.0000	0.0000	0.0127	0.0000	0.0000	0.0127	0.0000	0.0000	0.0000	0.0000	0.0000
1.6520	0.0210	0.0127	0.0000	0.0000	0.0127	0.0000	0.0000	0.0000	0.0000	0.0000
3.3120	0.0421	0.0127	0.0000	0.0000	0.0127	0.0000	0.0000	0.0000	0.0000	0.0000
4.9770	0.0633	0.0127	0.0000	0.0000	0.0127	0.0000	0.0000	0.0000	0.0000	0.0000
6.6450	0.0845	0.0127	0.0000	0.0000	0.0127	0.0000	0.0000	0.0000	0.0000	0.0000
8.3120	0.1057	0.0127	0.0000	0.0000	0.0127	0.0000	0.0000	0.0000	0.0000	0.0000
10.0111	0.1271	0.0127	0.0000	0.0000	0.0127	0.0000	0.0000	0.0000	0.0000	0.0000

Continued

Angular Rotational Gripper Dynamics										
t (s)	θ (rad)	ω_{RG} (rad/s)	α_{RG} (rad/s²)	$\dot{\alpha}_{jRg}$ (rad/s³)	ω_{RG} (rad/s)	α_{RG} (rad/s²)	$\dot{\alpha}\, j_{RG}$ (rad/s³)	E_{ω} (%)	E_{α} (%)	$E_{\dot{\alpha}}$ (%)
0.0000	0.0000	0.0318	0.0000	0.0000	0.0318	0.0000	0.0000	0.0000	0.0000	0.0010
1.6520	0.0524	0.0316	0.0000	0.0000	0.0316	0.0000	0.0000	0.0000	0.0000	0.0000
3.3120	0,1047	0.0315	0.0000	0.0000	0.0315	0.0000	0.0000	0.0000	0.0000	0.0000
4.9770	0.1571	0.0314	0.0000	0.0000	0.0314	0.0000	0.0000	0.0000	0.0000	0.0000
6.6450	0.2094	0.0314	0.0000	0.0000	0.0314	0.0000	0.0000	0.0000	0.0000	0.0007
8.3120	0.2618	0.0315	0.0000	0.0000	0.0315	0.0000	0.0000	0.0000	0.0000	0.0000
10.0111	0.3151	0.0318	0.0003	0.0002	0.0318	0.0003	0.0002	0.0000	0.0000	0.0011
Curvilinear Rotational Gripper Dynamics										
t (s)	s_{RG} (m)	v_{RG} (m/s)	a_{RG} (m/s²)	j_{RG} (m/s³)	v_{RG} (m/s)	a_{RG} (m/s²)	j_{RG} (m/s³)	E_v (%)	E_a (%)	E_j (%)
0.0000	0.0000	0.0129	0.0004	0.0000	0.0129	0.0004	0.0114	0.0000	0.0000	0.0000
1.6520	0.0212	0.0128	0.0004	0.0000	0.0128	0.0004	0.0000	0.0000	0.0086	0.0000
3.3120	0.0424	0.0128	0.0004	0.0000	0.0128	0.0004	0.0146	0.0000	0.0000	0.0000
4.9770	0.0636	0.0127	0.0004	0.0000	0.0127	0.0004	0.0127	0.0000	0.0016	0.0000
6.6450	0.0848	0.0127	0.0004	0.0000	0.0127	0.0004	0.0000	0.0000	0.0000	0.0000
8.3120	0.1061	0.0127	0.0004	0.0000	0.0127	0.0004	0.0085	0.0000	0.0000	0.0000
10.0111	0.1277	0.0129	0.0004	0.0000	0.0129	0.0004	0.0063	0.0000	0.0010	0.0000
Curvilinear Inverse Wedge Cam Dynamics										
t (s)	h_c (m)	v_c (m/s)	a_c (m/s²)	j_c (m/s³)	v_c (m/s)	a_c (m/s²)	j_c (m/s³)	E_v (%)	E_a (%)	E_j (%)
0.0000	0.0000	0.0138	0.0008	0.0000	0.0138	0.0008	0.0000	0.0000	0.0000	0.0010
1.6520	0.0223	0.0133	0.0008	0.0000	0.0133	0.0008	0.0000	0.0000	0.0000	0.0000
3.3120	0.0440	0.0129	0.0008	0.0000	0.0129	0.0008	0.0000	0.0000	0.0000	0.0000
4.9770	0.0649	0.0125	0.0008	0.0000	0.0125	0.0008	0.0000	0.0000	0.0000	0.0000
6.6450	0.0851	0.0121	0.0007	0.0000	0.0121	0.0007	0.0000	0.0000	0.0000	0.0000
8.3120	0.1045	0.0177	0.0007	0.0000	0.0177	0.0007	0.0000	0.0000	0.0000	0.0000
10.0111	0.1233	0.0114	0.0007	0.0000	0.0114	0.0007	0.0000	0.0000	0.0000	0.0001

(b)

Incr.	Exact				Approximate			Percent Error		
Rectilinear Translational Gripper Dynamics										
t (s)	s_{TG} (m)	v_{TG} (m/s)	a_{TG} (m/s²)	j_{TG} (m/s³)	v_{TG} (m/s)	a_{TG} (m/s²)	j_{TG} (m/s³)	E_v (%)	E_a (%)	E_j (%)
0.0000	0.0000	0.0127	0.0000	0.0000	0.0127	0.0000	0.0000	0.0000	0.0000	0.0000

Continued

1.6520	0.0210	0.0127	0.0000	0.0000	0.0127	0.0000	0.0000	0.0000	0.0000	0.0000
3.3120	0.0421	0.0127	0.0000	0.0000	0.0127	0.0000	0.0000	0.0000	0.0000	0.0000
4.9770	0.0633	0.0127	0.0000	0.0000	0.0127	0.0000	0.0000	0.0000	0.0000	0.0000
6.6450	0.0845	0.0127	0.0000	0.0000	0.0127	0.0000	0.0000	0.0000	0.0000	0.0000
8.3120	0.1057	0.0127	0.0000	0.0000	0.0127	0.0000	0.0000	0.0000	0.0000	0.0000
10.0111	0.1271	0.0127	0.0000	0.0000	0.0127	0.0000	0.0000	0.0000	0.0000	0.0000
Angular Rotational Gripper Dynamics										
t (s)	θ (rad)	ω_{RG} (rad/s)	α_{RG} (rad/s²)	$\dot{\alpha}_{jRg}$ (rad/s³)	ω_{RG} (rad/s)	α_{RG} (rad/s²)	$\dot{\alpha}\, j_{RG}$ (rad/s³)	E_{ω} (%)	E_{α} (%)	$E_{\dot{\alpha}}$ (%)
0.0000	0.0000	0.0318	0.0000	0.0000	0.0318	0.0000	0.0000	0.0000	0.0000	0.0010
1.6520	0.0524	0.0316	0.0000	0.0000	0.0316	0.0000	0.0000	0.0000	0.0000	0.0000
3.3120	0,1047	0.0315	0.0000	0.0000	0.0315	0.0000	0.0000	0.0000	0.0000	0.0000
4.9770	0.1571	0.0314	0.0000	0.0000	0.0314	0.0000	0.0000	0.0000	0.0000	0.0000
6.6450	0.2094	0.0314	0.0000	0.0000	0.0314	0.0000	0.0000	0.0000	0.0000	0.0007
8.3120	0.2618	0.0315	0.0000	0.0000	0.0315	0.0000	0.0000	0.0000	0.0000	0.0000
10.0111	0.3151	0.0318	0.0003	0.0002	0.0318	0.0003	0.0002	0.0000	0.0000	0.0011
Curvilinear Rotational Gripper Dynamics										
t (s)	s_{RG} (m)	v_{RG} (m/s)	a_{RG} (m/s²)	j_{RG} (m/s³)	v_{RG} (m/s)	a_{RG} (m/s²)	j_{RG} (m/s³)	E_v (%)	E_a (%)	E_j (%)
0.0000	0.0000	0.0129	0.0004	0.0000	0.0129	0.0004	0.0114	0.0000	0.0000	0.0000
1.6520	0.0212	0.0128	0.0004	0.0000	0.0128	0.0004	0.0000	0.0000	0.0086	0.0000
3.3120	0.0424	0.0128	0.0004	0.0000	0.0128	0.0004	0.0146	0.0000	0.0000	0.0000
4.9770	0.0636	0.0127	0.0004	0.0000	0.0127	0.0004	0.0127	0.0000	0.0016	0.0000
6.6450	0.0848	0.0127	0.0004	0.0000	0.0127	0.0004	0.0000	0.0000	0.0000	0.0000
8.3120	0.1061	0.0127	0.0004	0.0000	0.0127	0.0004	0.0085	0.0000	0.0000	0.0000
10.0111	0.1277	0.0129	0.0004	0.0000	0.0129	0.0004	0.0063	0.0000	0.0010	0.0000
Curvilinear Regular Wedge Cam Dynamics										
t (s)	h_c (m)	v_c (m/s)	a_c (m/s²)	j_c (m/s³)	v_c (m/s)	a_c (m/s²)	j_c (m/s³)	E_v (%)	E_a (%)	E_j (%)
0.0000	0.0000	0.0132	0.0002	0.0000	0.0132	0.0002	0.0000	0.0000	0.0000	0.0000
1.6520	0.0216	0.0129	0.0002	0.0000	0.0129	0.0002	0.0000	0.0000	0.0000	0.0000
3.3120	0.0428	0.0126	0.0002	0.0000	0.0126	0.0002	0.0000	0.0000	0.0000	0.0013
4.9770	0.0636	0.0123	0.0002	0.0000	0.0123	0.0002	0.0000	0.0000	0.0000	0.0000
6.6450	0.0839	0.0120	0.0002	0.0000	0.0120	0.0002	0.0000	0.0000	0.0000	0.0000
8.3120	0.1037	0.0117	0.0002	0.0000	0.0117	0.0002	0.0000	0.0000	0.0000	0.0000
10.0111	0.1233	0.0114	0.0002	0.0000	0.0114	0.0002	0.0000	0.0000	0.0000	0.0000

5. Conclusions with Limitations

In conclusion, the theoretical self-centering wedge cam procedures and associated quantitative model(s) are adequately derived from first principles and validated through application within the context of a design concept(s). Various approaches involved within the derivation of the model(s) were presented which included both approximation and exact methods in conjunction with fundamental mathematics applied within the context of kinematics theory and the laws of mechanics. However, it is important to note that when using approximation methods, unexplained variation in self-centering as well as approximation errors due to numerical differentiation will be induced into the design framework.

Nevertheless, establishing the foundational theory sets the premise through which product designs with this needed functionality of self-centering around cylindrical workpieces can be better engineered or improved upon with proven quality design concepts such as robust design at their heart for increasing accuracy and precision in final output product designs. Moreover, the quantitative model presented is highly useful and important for design optimization in connection with computer-based robust design optimization techniques as once a reliable model is obtained, optimization results can often be quickly realized. Therefore, having this analytical model(s) is very beneficial for the practicing design engineer or inventor with sufficient mechanical engineering background and knowledge tasked with developing a product design of this self-centering inverse/regular wedge cam type under limited time constraints or lacking the specialized knowledge which may require the use of this self-centering theory as part of research & development activities.

To further mention, the entailed research is mathematically extensive and intensive in nature which may provide insights beyond the specific self-centering theory depicted and into the development of other novel theories and research areas. However, care must always be taken to thoroughly validate mathematical-based engineering models. While real-world product development activities were outside of the scope and focus of this current research manuscript, physical prototypes with experimental testing are crucial for confirming the computer-aided simulations presented herein thereby demonstrating the effectiveness of a proposed design in a real-world setting including operating conditions, manufacturing tolerances, material properties, and external disturbances.

Moreover, and worth considering, engineering designs represent a compromise among conflicting objectives and sometimes qualitative aspects will drive a design in significant ways. In connection, it is just as important to select the best concept for achieving the desired goal as optimization algorithms do not choose a design concept and only help optimize a particular concept. Consequently, the utilization of this theory in conjunction with a systems-based concurrent engineering approach should be considered for ensuring a design approaches the best design in relation to achieving true 'robustness' as it incorporates a holistic approach to solving engineering problems.

6. Future Research

Having the associated mathematical model as presented within paves way for future application toward a design concept in preparation for quantitative design synthesis regarding computer-based design optimization. This can be accomplished through robust design optimization techniques thereby providing a natural framework for creating robust product designs as it is an optimization problem at heart. Therefore, "*robust design should be done in concert with optimization, since part of the robust design philosophy is to integrate variation and performance considerations together, which can be accomplished in a straightforward way using optimization methods*" [47].

Consequently, future research will involve preparing a design concept involving the self-centering cam theory that will be couched in terms of robust design and robust design optimization techniques along with performing sensitivity robust design optimization for minimizing a critical characteristic's variation. This will take the form of first looking into robust design methods while considering operating conditions and external factors along with using good engineering judgment through means of establishing insights based on the theoretical kinematic cam procedures. This is an important preliminary aspect of design optimization as the theoretical procedures aid in providing design insights for reducing overall model complexity from a systems engineering view imperative to accurately performing computer-based optimization which typically requires a reasonably close starting point to the final global/local optimum solution. Extending upon such, design tolerances linked to manufacturing process capability in conjunction with statistical tolerancing connected to feasibility robust design optimization will be incorporated in future research for further balancing and vibration minimization as well as true physical clamping is concerned. Following, various computer-aided engineering optimization techniques will be employed in context of the self-centering quantitative model for reducing the critical characteristic's variation and assessing manufacturing tolerances along with comparison to the theoretical model(s).

Furthermore, physical prototypes of baseline concepts vs. optimized concepts along with experimental testing coupled with studies into the nonlinear dynamic response of these cams subjected to rapid load changes, particularly relevant in robotics applications, in addition to reviewing how dynamic loads affect wear and longevity in relation to clamping accuracy will commence. In conjunction, this may be contained within the Design for Six Sigma (DFSS/DMADV) framework for taking a holistic systems engineering approach to robust design as it is almost always the case that a system vs. component view will produce the best design [48].

Authors' Contributions

Shawn P. Guillory: Conceptualization, formal analysis, methodology, validation, visualization, Writing-original draft, Writing-review & editing, **Alan A. Barhorst:** Supervision, Writing-review, **Jim Lee:** Writing-review, **Jonathan R. Raush:** Writing-review, **Raju Gottumukkala:** Writing-review, **Terrence L. Chambers:** Supervision, Writing-review & editing.

Acknowledgments

The author would like to provide a special note of appreciation toward Mr. Jason and Jacob Neu, both with Neu Company, LLC, a Civil/Structural Engineering firm specializing in the overhead crane, heavy industrial, oil & gas and maritime industries, for their industry support toward my professional career growth and family life during my doctoral studies which comprise this manuscript's research.

Conflicts of Interest

The authors declare no conflicts of interest regarding the publication of this paper.

References

[1] Bruno, D. (1970) Clamping Device. U.S. Patent No.3535963.27.

[2] Dietmar, H. and Herbert, I. (1984) Steady for Holding Rod-Like Circular Cross-Section Components. U.S. Patent No.4463635.07.

[3] Guy, W. (1989) Self-Centering Steady Rest. U.S. Patent No.4823657.25.

[4] Karl, H. (1988) Self-Centering Steady Rest for Lathe. U.S. Patent No.4754673.05.

[5] Paul, O. (1985) Multi-Purpose Steady Rest. U.S. Patent No.4546681.15.

[6] Peter, F. (2002) Self-Centering Steady Rest Clamping Device. U.S. Patent No.6458022.01.

[7] Peter, H. and Eckhard, M. (2011) Self-Centering Steady Rest. U.S. Patent No.20110209591.01.

[8] Peter, H. and Eckhard, M. (2014) Self-Centering Steady Rest. U.S. Patent No.8726772B2.20.

[9] Richard, L. (2008) Steady Rest for Rotating Shaft. U.S. Patent No.20080139092.12.

[10] Stefano, R. (1985) Selfcentering Work-Rest. U.S. Patent No.4519279.28.

[11] ARMS Automation (2024) https://www.armsautomation.com

[12] Arobotech Systems Inc (2024) https://arobotech.com/

[13] Atling Steady Rest (2024) https://www.atling.com/

[14] Fenwick and Ravi (2024) https://www.fenwickandravi.co.in/

[15] Kitagawa (2024) https://kitagawa.global/

[16] RÖHM (2024) http://www.roehm.biz/

[17] SAJRAJ Technologies (2024) https://www.steadyrestmanufacturer.com/

[18] SCHUNK SE & Co. KG (2024) https://www.schunk.com/

[19] SMW-AUTOBLOK (2024) https://www.smwautoblok.com/

[20] David, S., Jeff, H., Lawrence, H. and Bernd, R. (2009) Positioning and Spinning Device. U.S Patent No.7509722-B2.

[21] Afandiyev, E.M. and Nuriyev, M.N. (2021) Analysis of the Condition of a Pipe Fixed in a Clamping Device. *EUREKA: Physics and Engineering*, No. 1, 78-85.

[22] Wang, L., Guo, S., Gong, H. and Shang, X. (2016) Research and Development of a Self-Centering Clamping Device for Deep-Water Multifunctional Pipeline Repair

Machinery. *Natural Gas Industry B*, **3**, 82-89.
https://doi.org/10.1016/j.ngib.2015.12.012

[23] Bavadekar, P.S., Survase, P.P., Hogade, R.S., Patil, S.R., Dhokale, O.S. and Mhamane, D.A. (2020) Design and Analysis of Self Centering Steady Rest for CNC Turning Machine. *International Research Journal of Engineering and Technology*, **6**, 13-21.

[24] Rajendra, B.L. and Satish, B.G. (2016) Design and Analysis of Self Centering Steady Rest for Supercut-6 CNC Turning Machine Using CAD & FEA. *Ram Meghe Institute of Technology & Research*, **4**, 14-19.

[25] Dinesh, J.G. and Pooja, J.S. (2015) Design and Analysis of Self Centering Automatic Gripper (Steady Rest) for Supercut-6 CNC Turning Machine Using CAD and FEA. *International Engineering Research Journal*, No. 3, 65-68.

[26] Chen, T.L. and Xie, Z.Q. (2019) Design and Machining of Translation Cam for Self-Centering Center Rest. *Mechanical Research & Application*, 32, 152-154, 159.

[27] He, R.K. (1999) Cam Curve Design and Processing of Hydraulic Center Frame. *Mechanical Design and Manufacturing*, No. 4, 46.

[28] Li, J.L. (1991) Calculation of Working Wedge Curve of Self-Centering Steady Rest. *Machinery Manufacturing Engineer*, No. 11, 27-28.

[29] Liu, B.F. and Xu, X.D. (2000) Solving the Translational Convex Contour of the Open Self-Centering Center Frame Using the Instantaneous Center Method. *Journal of Jiangnan University*, **15**, 34-37.

[30] Lu, X.Y. and Xie, N.F. (2008) Research on the Derivation of Cam Curve of Hydraulic Self-Centering Steady Rest. *Mechanical Design and Manufacturing*, No. 4, 24-25.

[31] Wang, Y.L. and Ying, Q.F. (2019) Design and Machining of Cam Curve of the Self-Centering Steady Rest. *Manufacturing Technology & Machine Tool*, No. 3, 64-66.

[32] Xiao, K. (2013) Calculation of Internal Process Cam Curve of Self-Centering Steady Rest. *Equipment Manufacturing Technology*, No. 3, 149-150.

[33] Xu, N.N. and Tang, W.C. (2015) Design Calculation for Wedge Cam of Small Roller Centering Three-Jaw Jig. *Key Engineering Materials*, **656-657**, 641-645.
https://doi.org/10.4028/www.scientific.net/KEM.656-657.641

[34] Xie, Z.Q. (2021) Design and Machining of Self-Centering Center Rest Cam Mechanism Based on Linear Approximation. *Mechanical Research & Application*, **34**, 77-82.

[35] Xie, Z.Q., Ni. Y. and Miu, Q.L. (2021) Research on Linear Approximation of Errors Such as Convex Contour Line of Self-Centering Steady Frame. *Mechanical Engineering and Automation*, No. 2, 34-36, 39.

[36] Rothbart, H.A. (2004) Cam Design Handbook. McGraw Hill.
https://doi.org/10.1115/1.1723466

[37] Chironis, N.P. and Sclater, N. (2007) Mechanisms and Mechanical Devices Sourcebook. 4th Edition, McGraw Hill.

[38] Uicker, J., Pennock, G. and Shigley, J. (1995) Theory of Machines and Mechanisms. 2nd Edition, McGraw Hill.

[39] Tsay, D.M. and Wei, H.M. (1996) A General Approach to the Determination of Planar and Spatial Cam Profiles. *Journal of Mechanical Design*, **118**, 259-265.
https://doi.org/10.1115/1.2826878

[40] Zhang, J., Sun, S.L. and Wu, Y.F. (2019) Design and Analysis of Cylindrical Indexing Cam Mechanism of Tool Magazine in Machining Center. *Machine Tool & Hydraulics*, **81**, 175-188.

[41] Ade, M., Kucheriya, N., Laware, S., Patil, T., Jain, A. and Dakhole, M.Y. (2020) Cam Design Using Polydyne Approach. *International Research Journal of Engineering and Technology*, **7**, 1388-1392.

[42] Meena, S., Laxmi, S. and Vijay, K. (2016) Design of Cam and Follower System Using Basic and Synthetic Curves: A Review. *International Journal of Innovative Science, Engineering & Technology*, **3**, 362-372.

[43] Zhou, C., Hu, B., Chen, S. and Ma, L. (2016) Design and Analysis of High-Speed Cam Mechanism Using Fourier Series. *Mechanism and Machine Theory*, **104**, 118-129. https://doi.org/10.1016/j.mechmachtheory.2016.05.009

[44] Szydlowski, W.M. (2000) Self-Aligning Mechanisms, Forgotten Part of ME Curriculum. University of Nebraska-Lincoln, Session 3425, 5.540.1-5.540.14.

[45] Brooks, S.H., Magleby, S.P. and Howell, L.L. (2005) Grasping Mechanisms with Self-Centering and Force-Balancing Characteristics. *ASME* 2005 *International Design Engineering Technical Conferences and Computers and Information in Engineering Conference*, Long Beach, 24-28 September 2005, 405-414. https://doi.org/10.1115/DETC2005-85478

[46] Guillory, S.P. (2025) A Simulated Unified Resultant Amplitude Method for Multi-Dimensional/Multi-Variable Opposite Wave Summation. *Journal of Applied Mathematics and Physics*, **13**, 281-301. https://doi.org/10.4236/jamp.2025.131013

[47] Parkinson, A. (1995) Robust Mechanical Design Using Engineering Models. *Journal of Mechanical Design*, **117**, 48-54. https://doi.org/10.1115/1.2836470

[48] Parkinson, A.R., Hedengren, J.D. and Balling, R.J. (2013) Optimization Methods for Engineering Design. Brigham University Press.

[49] Hibbler, R.C. (1974) Engineering Mechanics Dynamics. 7th Edition, Prentice Hall.

[50] Helgason, S. (n.d.) Sophus Lie, the Mathematician. Courtesy of Scandinavian University Press, 3-21.

Appendix A: The Nonlinear Second Order Nonhomogeneous Instantaneous Constant Radius of Curvature Ordinary Differential Equation (ODE)

In connection with an ordinary differential equation arising from the radius of curvature Equation (A1), a radius of this kind can be correlated with the polar coordinate determined from the Pythagorean theorem as widely known by Equation (A2) [49]. While in general, the polar coordinate and the radius of curvature are not identical, there is one condition that results in equivalence. This condition occurs when all centers of curvature are coincident with the same origin of the Cartesian plane.

$$r_{rc}(x) = \frac{\left(1 + y'(x)^2\right)^{3/2}}{\left|y''(x)\right|} \tag{A1}$$

$$r_{pc}(x) = \sqrt{x^2 + y(x)^2} \tag{A2}$$

Nevertheless, and as shown, Equation (A1) represents a differential equation in atypical form. To determine the characteristics of this differential equation, it is converted into a form that is typically presented in the context of differential equation analysis as defined by Equations (A3) and (A4).

$$r_{rc}^2(x)\, y''(x)^2 = \left(1 + y'(x)^2\right)^3 \tag{A3}$$

$$r_{rc}^2(x)\, y''(x)^2 = 1 + 3y'(x)^2 + 3y'(x)^4 + y'(x)^6 \tag{A4}$$

Regarding Equation (A4), the differential equation is described as nonlinear and nonhomogeneous. In relation to the solution of the differential equation, the function $y(x)$ is considered to be an unknown function. In connection, when the radius of curvature is given in terms of x, there is a definite solution to the differential equation. The derivation of the solution consistent with the uniqueness and existence theorem is presented below.

$$y(x) = \mp\sqrt{r_{rc}^2(x) - x^2 \pm 2r_{rc}(x)c_1(x)x - r_{rc}^2(x)c_1^2(x)} + c_2(x) \tag{A5}$$

However, and to note, the functions $c_1(x)$ and $c_2(x)$ are currently unknown (will be determined further below). Additionally, the plus/minus signs indicate multiple solutions which can be chosen in reference to **Table A1** below.

Table A1. Plus/minus sign patterns.

Solution Num	Radical Term	Term $2r_{rc}(x)c_1(x)x$
1	−	+
2	+	+
3	−	−
4	+	−

For eliminating the use of **Table A1**, the plus/minus sign patterns will be mathematically modeled through equations that depend on an integer-based solution number s_{num} that ranges from 1 to 4. This will be accomplished by utilizing Euler's equation in specific reference to URAM theory [46]. The resulting calculations that produce the plus/minus sign patterns are given in **Table A2** and accompanying Equations (A6) and (A7) below.

Table A2. Calculations for the Plus/Minus Sign Patterns.

s_{num}	Values for $\hat{s}_1$	Values for $\hat{s}_2$
1	$e^{i(1\pi)} = -1$	$-\left(e^{i(\pi)}\right) = +1$
2	$e^{i(2\pi)} = +1$	$-\left(e^{i(\pi)}e^{i(2\pi)}\right) = +1$
3	$e^{i(3\pi)} = -1$	$-\left(e^{i(\pi)}e^{i(2\pi)}e^{i(3\pi)}\right) = -1$
4	$e^{i(4\pi)} = +1$	$-\left(e^{i(\pi)}e^{i(2\pi)}e^{i(3\pi)}e^{i(4\pi)}\right) = -1$

$$\hat{s}_1 = e^{i(s_{num}\pi)} \Rightarrow \cos(s_{num}\pi) + i\sin(s_{num}\pi) \quad s_{num} = 1,2,3,4 \tag{A6}$$

$$\hat{s}_2 = -\prod_{m=1}^{s_{num}} e^{i(m\pi)} \Rightarrow (-1)^{\text{Floor}\left(\frac{s_{num}-1}{2}\right)} \quad s_{num} = 1,2,3,4 \tag{A7}$$

With the above equations containing the plus/minus sign patterns, the ODE solution becomes:

$$y(x) = \hat{s}_1\sqrt{r_{rc}^2(x) - x^2 + 2\hat{s}_2 r_{rc}(x) c_1(x) x - r_{rc}^2(x) c_1^2(x)} + c_2(x) \tag{A8}$$

The radius of curvature $r_{rc}(x)$ is treated as a constant along with utilizing the parameters $c_1(x)$ and $c_2(x)$ (which would normally be constants in typical differential equation theory). However, the true variable nature of the functions $r_{rc}(x)$, $c_1(x)$, and $c_2(x)$ can be viewed as instantaneous constants that change from point to point for this specific ODE theory. This is consistent with the definition for the radius of curvature which states that it creates a circle that best approximates the curve and changes on a pointwise basis.

In view of the instantaneous constant nature involved with this differential equation, the square of the radius of curvature is congruent to an instantaneous constant Lie symmetry invariant corresponding to well-known transformation equations for rotation in the x - y plane. To mention, around 1870, Marius Sophus Lie realized that many of the methods for solving differential equations could be unified using group theory. Lie symmetry methods are central to the modern approach for studying nonlinear ODEs. They use the notion of symmetry to generate solutions in a systematic manner. Moreover, the works of Sophus Lie have an interesting connection with a powerful technique used in the theory of nonlinear ordinary differential equations which is in alignment with the instantaneous constant nature of the nonlinear radius of curvature ODE [50].

With having the ODE solution given by Equation (A8), the following condition can be extrapolated to determine whether the solution is real or complex.

$$r_{rc}^2(x) - x^2 + 2\hat{s}_2 r_{rc}(x) c_1(x) x - r_{rc}^2(x) c_1^2(x) > 0 \tag{A9}$$

Moving further, the associated spatial derivatives of the ODE solution are determined on an instantaneous constant basis in the following manner.

$$y'(x) = \frac{\hat{s}_1\left(-2x + 2\hat{s}_2 r_{rc}(x) c_1(x)\right)}{2\sqrt{r_{rc}^2(x) - x^2 + 2\hat{s}_2 r_{rc}(x) c_1(x) x - r_{rc}^2(x) c_1^2(x)}} \tag{A10}$$

$$y''(x) = -\hat{s}_1\left(\frac{\left(-2x + 2\hat{s}_2 r_{rc}(x) c_1(x)\right)^2}{4\left(r_{rc}^2(x) - x^2 + 2\hat{s}_2 r_{rc}(x) c_1(x) x - r_{rc}^2(x) c_1^2(x)\right)^{3/2}} + \frac{1}{\sqrt{r_{rc}^2(x) - x^2 + 2\hat{s}_2 r_{rc}(x) c_1(x) x - r_{rc}^2(x) c_1^2(x)}}\right) \tag{A11}$$

More importantly, having the ODE solution and its first spatial derivative enables a determination of the functions $c_1(x)$ and $c_2(x)$ through the use of known variable initial conditions $k_1(x)$ and $k_2(x)$.

$$k_1(x) = y(x) \tag{A12}$$

$$k_2(x) = y'(x) \tag{A13}$$

Solving for the parameters $c_1(x)$ and $c_2(x)$, we have:

$$c_1(x) = \frac{\hat{s}_2 x}{r_{rc}(x)} \pm \frac{k_2^2(x) r_{rc}^2(x)}{\sqrt{k_2^2(x)\left(1 + k_2^2(x)\right) r_{rc}^4(x)}} \tag{A14}$$

$$c_2(x) = k_1(x) - \hat{s}_1\sqrt{r_{rc}^2(x) - x^2 + 2\hat{s}_2 r_{rc}(x) c_1(x) x - r_{rc}^2(x) c_1^2(x)} \tag{A15}$$

In summary, the nonlinear radius of curvature ODE solution has been fully generalized with the functions $c_1(x)$ and $c_2(x)$ being determined from Equations (A14) and (A15). We conclude that the radius of curvature and associated initial condition functions adequately define the path $y(x)$ in rectangular form. However, the path can also be determined through a parametric equation $y(\theta)$ with the radius of curvature and initial conditions being formulated in terms of the angle θ. Another aspect worth noting is that the path in parametric form can be converted into rectangular form by substituting $\theta(x)$ into the associated equations for the radius of curvature and initial conditions. Nevertheless, it is important to reiterate that the solution does not define the path equation in full and only does so in relation to an instantaneous constant fashion. Future research may explore this nonlinear ODE regarding the development of the full path equation.